NUMERICAL INVESTIGATION OF BUBBLE ENTRAPMENT WITH TIP VORTEX VIA AN EULERIAN-LAGRANGIAN APPROACH

TZU-YAO HUANG

Department of Maritime and Transport Technology
Faculty of Mechanical, Maritime and Materials Engineering
Delft University of Technology (TU Delft)

August 2022

Tzu-Yao Huang: *Numerical investigation of bubble entrapment with tip vortex via an Eulerian-Lagrangian approach* © August 2022

SUPERVISORS:
Prof.dr.ir. T. J. C. van Terwisga & Dr. A. K. Lidtke &
Ir. M. Stigter & Ir. M. X. van Rijsbergen

LOCATION:
Delft, South Holland, the Netherlands

TIME FRAME:
November 2021 – August 2022

The thesis is typeset in LaTeX 2ε with hypertext to prepare the references, abbreviations, figures and tables.

An electronic version of the thesis is available at TU Delft Repository.

NUMERICAL INVESTIGATION OF BUBBLE ENTRAPMENT WITH TIP VORTEX VIA AN EULERIAN-LAGRANGIAN APPROACH

TZU-YAO HUANG

in partial fulfillment of the requirements for the degree of

Master of Science
in Marine Technology

with the specialization
of Ship Hydromechanics

at the Delft University of Technology;

to be defended publicly on
Wednesday August 31st, 2022 at 2:00 p.m. (CEST).

Student number:	5306744	
Report number:	MT.21/22.047.M	
Thesis Committee:	Prof.dr.ir. T. J. C. van Terwisga,	TU Delft, chair
	Dr. A. K. Lidtke,	MARIN, supervisor
	Ir. M. Stigter,	TU Delft, supervisor
	Ir. M. X. van Rijsbergen,	MARIN, supervisor
	Dr.ir. M. J. B. M. Pourquie,	TU Delft, member

This page intentionally left blank

ABSTRACT

Tip vortex cavitation around the marine propeller is the primary source of the underwater noises emitted by ships. Investigating the tip vortex inception is important to understand the aforementioned side effect. The water quality, highly related to the bubbles population, surrounding the tip vortex is crucial to the tip vortex cavitation inception. This research explores how bubble moves around the tip vortex and investigates its background mechanisms. A one-way coupled Lagrangian bubble tracking model is applied to the Lamb-Oseen vortex and the hydrofoil tip vortex flow field, where the tip vortex is simulated with an open-usage Computational Fluid Dynamics (CFD) software, ReFRESCO. A series of capture time models have been developed by exploiting the bubble force (acceleration) balance in the Lamb-Oseen vortex to identify the crucial parameters. The other aspect of the acceleration analysis reflects the role of the lift force as the system's stabilizer, which has long been ignored. In the CFD tip vortex flow simulation, the bubble population evolution is investigated from upstream to downstream. Several kinds of bubble behaviors around the tip vortex flow have been identified via the numerical simulation, and simplified models based on the bubble force analysis have been proposed in order to explain them. Mainly due to the stagnation bubble events, clustering of large bubbles has been discovered a short distance downstream of the foil tip, implying that this may be a possible hotspot for tip vortex cavitation inception. The stagnation bubble phenomenon still needs to be further investigated, particularly in terms of quantifying its dependence on various flow parameters. The results also need to be rigorously validated which has not been possible as of yet due to insufficient measurement data. Still, this research manages to explore the bubble motion around the tip vortex and their fundamental mechanism.

Keywords: tip vortex, cavitation inception, water quality, bubble entrapment, ReFRESCO, Eulerian-Lagrangian Method

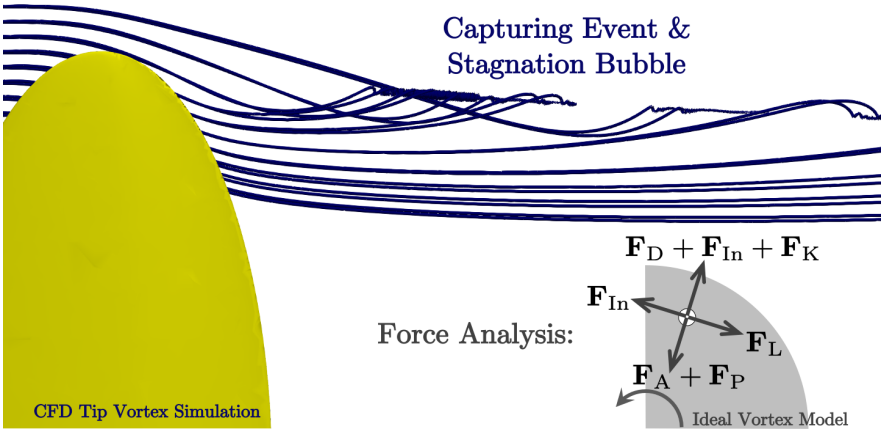

Graphical abstract.

ACKNOWLEDGMENTS

First of all, I would like to thank my supervisor, Prof. Tom van Terwisga, for his coordination of my thesis and his precious support. He provided me ample support and also introduced many professionals to consult. The thesis would not even start without him.

Next, I am deeply indebted to Dr. Artur K. Lidtke, one of my daily supervisors, from MARIN. He is so kind that he keeps encouraging me on the path with his endless patience. He sacrificed his precious time even on holiday only to guide me to the right path. I will never forget the time we spent in the Teams solving the numerical errors and craving the model concepts. Also, he kindly provided me a bunch of well-structured source codes and clever automation tools. Those codes have brought me to a higher level of programming skills and saved me a tremendous amount of unnecessary time. Furthermore, he provided me insight into how to build a scientific researcher mindset, the most precious present along the journey.

I'm also extremely grateful to Ir. Rens Stigter, the other daily supervisor, from TU Delft. He also encouraged me a lot with his precious kindness whenever I thought I did not meet the expectations. Also, every time we met always brought me different viewpoints as an experimentalist, which is especially priceless for me, who spends most of the time in the numerical area. The insightful recommendations always led the research in the correct way. Besides, his continuous review of my thesis made it less awkward and more logical. He is the one who saw the growth of the research.

Thanks should also go to Ir. Martijn van Rijsbergen from MARIN. His recommendations, regardless of the visualizations or the numerical results, made this research more reader-friendly and comprehensive.

I would like to extend my sincere thanks to Mr. Yu-Cheng Hsu back in Taiwan. Ever since my bachelor's study, he has always guided me with his valuable aesthetic insight into every academic aspect. He is so generous that he is willing to correct this research despite his busy work schedule.

Lastly, words cannot express my gratitude to my parents and sister for their constant support in my academic career. Their endless love gives me the courage to pursue my dream without concerns. Their unconditional love also forms a concrete harbor whenever I am tired. I am sincerely indebted for not accompanying them during these two years.

Tzu-Yao Huang,
Delft, August 2022

CONTENTS

LIST OF FIGURES

This page intentionally left blank

LIST OF TABLES

This page intentionally left blank

ACRONYMS

AOA	Angle of Attack
CFD	Computational Fluid Dynamics
DBM	Discrete Bubble Model
DDES	Delayed Detached-eddy Simulation
DES	Detached-eddy Simulation
DNS	Direct-numerical Simulation
EARSM	Explicit Algebraic Reynolds Stress Model
IDDES	Improved Delayed Detached-eddy Simulation
ILES	Implicit Large-eddy Simulation
LCTM	Local Correlation-based Transition Model
LES	Large-eddy Simulation
LPT	Lagrangian Particle Tracking
ODE	Ordinary Differential Equation
PANS	Partially-averaged Navier-Stokes
RANS	Reynolds-averaged Navier-Stokes
RSM	Reynolds Stress Model
SST	Shear-stress Transport
URN	Underwater Radiated Noise
VOF	Volume of Fluid

This page intentionally left blank

NOMENCLATURE

Latin symbols

a	quasi-drag coefficient	$[1/s]$
a_{ij}	the ij^{th} component of Reynolds stress anisotropy tensor	$[1/s]$
b	the half-span of a elliptical foil	$[m]$
C_{AM}	added mass coefficient	$[-]$
C_D	drag coefficient	$[-]$
C_i, C_i^*	coefficients of SSG model	$[-]$
C_L	bubble lift coefficient	$[-]$
C_L	hydrofoil lift coefficient	$[-]$
C_P	pressure coefficient	$[-]$
$C_{P_{\text{crit}}}$	critical pressure coefficient	$[-]$
$C_{P_{\text{min}}}$	minimum pressure coefficient	$[-]$
$C_{P_{\text{v}}}$	vapor pressure coefficient	$[-]$
C_μ	equilibrium parameter	$[-]$
c	the sound speed of the carrier phase	$[m/s]$
c_0	the root chord length of a elliptical foil	$[m]$
c_{ai}, c_{di}	coefficients in γ production and destruction term	$[-]$
$c_{\theta t}$	coefficients in $\tilde{\text{Re}}_{\theta t}$ production term	$[-]$
D	Reynolds stress diffusion coefficient	$[-]$
D_{ij}	the ij^{th} component of specific diffusion tensor	$[m^2/s^3]$
D_{ij}^{p}	the ij^{th} component of specific pressure diffusion tensor	$[m^2/s^3]$
D_{ij}^{v}	the ij^{th} component of specific viscous diffusion tensor	$[m^2/s^3]$

E_γ	specific destruction rate of the intermittency	$[m^2/s^3]$
$\hat{\mathbf{e}}_r$	radial unit vector	[-]
$\hat{\mathbf{e}}_\theta$	azimuthal unit vector	[-]
$\mathbf{F}_A$	added mass force	[N]
$\mathbf{F}_D$	drag force	[N]
$\mathbf{F}_H$	history force	[N]
$\mathbf{F}_K$	Kelvin impulse force	[N]
$\mathbf{F}_L$	lift force	[N]
$\mathbf{F}_P$	pressure gradient force	[N]
$\mathbf{F}_S$	hydrostatic force	[N]
F_{length}	correlation which controls the length of the transition region in γ production term	[-]
F_{onset}	switcher which controls the γ production term	[-]
F_{turb}	switcher for the turbulence in γ destruction term	[-]
$F_{\theta t}$	switcher which controls the $\tilde{Re}_{\theta t}$ production term	[-]
f	elliptic relaxation function (in $\bar{v^2}$-f turbulence model)	[1/s]
$\mathbf{g}$	gravitational acceleration vector	$[m/s^2]$
g	gravitational acceleration magnitude	$[m/s^2]$
$\mathbf{I}$	Kelvin impulse	[kg m/s]
k	turbulent kinetic energy	$[m^2/s^2]$
L	turbulent length scale	[m]
M_{ij}	the ij^{th} component of specific tensor of fluctuating mass flux contribution tensor	$[m^2/s^3]$
m	lifting line distribution factor	[-]
m_B	bubble mass	[kg]
N	number of the bubble in a certain section	[-]
N_0	number of the initial bubble population	[-]
$N_{x,y,z}$	the number of grid in the corresponding direction	[-]

n	polytropic constant	[-]
P	flow pressure	[Pa]
P_{crit}	minimum pressure	[Pa]
P_{g}	non-condensable gas pressure in bubble	[Pa]
P_{ij}	the ij^{th} component of specific production rate tensor	$[\mathrm{m}^2/\mathrm{s}^3]$
$\tilde{P}_{ij}$	the ij^{th} component of the modified specific production rate tensor by intermittency	$[\mathrm{m}^2/\mathrm{s}^3]$
P_{min}	minimum pressure	[Pa]
P_{v}	vapor pressure	[Pa]
P_{vc}	pressure at the viscous core edge	[Pa]
P_{γ}	specific production rate of the intermittency	$[\mathrm{m}^2/\mathrm{s}^3]$
$P_{\theta t}$	specific production rate of the intermittency local transition momentum thickness Reynolds number	$[\mathrm{m}^2/\mathrm{s}^3]$
P_{∞}	reference pressure	[Pa]
p	fluctuation flow pressure	[Pa]
q	dynamics pressure at the reference point	[Pa]
R	bubble radius	[m]
R^*	normalized bubble radius	[-]
$\dot{R}$	bubble wall velocity	$[\mathrm{m}/\mathrm{s}]$
$\ddot{R}$	bubble wall acceleration	$[\mathrm{m}/\mathrm{s}^2]$
R_0	initial bubble radius	[m]
R_{ij}	the ij^{th} component of specific Reynolds stress tensor	$[\mathrm{m}^2/\mathrm{s}^2]$
Re	Reynolds number	[-]
Re_{B}	bubble Reynolds number	[-]
Re_{c}	base chord Reynolds number	[-]
Re_{v}	vortex Reynolds number	[-]
Re_{θ}	momentum thickness based Reynolds number	[-]
$\mathrm{Re}_{\theta t}^{\mathrm{eq}}$	equivalent momentum thickness based Reynolds number in $\tilde{\mathrm{R}}\mathrm{e}_{\theta t}$ production term	[-]

$\tilde{\mathrm{Re}}_{\theta t}$	local transition onset momentum thickness Reynolds number	[-]
r	radial coordinate to the vortex center	[m]
r^*	normalized radial coordinate	[m]
$\dot{r}$	bubble radial velocity	[m/s]
$\ddot{r}$	bubble radial acceleration	[m/s^2]
r_0	initial bubble radial coordinate	[m]
r_0^*	normalized initial bubble radial coordinate	[-]
r_B	Rankine body radius	[m]
r_c	cavity core radius	[m]
r_cap	capture radius	[m]
r_s	settling radius	[m]
r_v	vortex core radius	[m]
S_{ij}	strain rate tensor	[1/s]
$\bar{S}$	averaged strain rate tensor	[1/s]
s_{ij}	fluctuation strain rate tensor	[1/s]
T	tension	[Pa]
$\mathcal{T}$	the averaging time window in Reynolds-averaging procedure	[s]
$\mathfrak{T}$	time scale in $\tilde{\mathrm{Re}}_{\theta t}$ production term	[s]
T_{ij}	the ij^{th} component of deviatoric stress tensor	[Pa]
$\mathcal{T}_{ij}$	the ij^{th} component of specific turbulent transport tensor	[m^2/s^3]
t	time	[s]
t_c	capture time	[s]
t_c^*	normalized capture time	[-]
$\mathbf{U}$	flow velocity vector	[m/s]
$\mathbf{U}_\mathrm{B}$	bubble velocity vector	[m/s]
U_i	the i^{th} component of flow velocity	[m/s]
U_ref	reference velocity magnitude	[m/s]
U_v	azimuthal velocity at viscous core edge	[m/s]

U_x	x component of flow velocity	$[m/s]$
U_x^*	x component of normalized flow velocity	[-]
U_y^*	y component of normalized flow velocity	[-]
U_{yz}	In-plane (x-plane) flow velocity	$[m/s]$
U_θ	azimuthal flow velocity	$[m/s]$
U_∞	unperturbed uniform inflow speed	$[m/s]$
u_i	the i^{th} component of fluctuation flow velocity	$[m/s]$
V_B	bubble volume	$[m^3]$
$\bar{v^2}$	fluctuation velocity scale (in $\bar{v^2}$-f turbulence model)	$[m^2/s^2]$
We	Weber number	[-]
W_{ij}	the ij^{th} component of spin tensor	$[1/s]$
x	x coordinate	$[m]$
$\dot{x}$	bubble axial velocity	$[m/s]$
x^*	normalized x coordinate	[-]
x_i	i^{th} components of the Cartesian coordinate	$[m]$
y	y coordinate	$[m]$
y^*	normalized y coordinate	[-]
z	z coordinate	$[m]$

Greek symbols

α	normalized shear rate	[-]
α_{foil}	angle of attack	[rad]
α_ω	coefficient of ω-production	[-]
β	cavitation coefficient of the Lamb-Oseen vortex	[-]
β_ω	coefficient of ω-destruction	[-]
Γ	circulation strength	$[m^2/s]$
Γ_0	maximum circulation strength	$[m^2/s]$
Γ_∞	circulation evaluated at infinity	$[m^2/s]$
γ	intermittency factor (in γ-$\tilde{Re}_{\theta t}$ transition model)	[-]
γ	dipole strength density	$[m/s]$

δ_{ij}	Kronecker delta	[-]
ε	isotropic turbulence dissipation rate	$[m^2/s^3]$
ε_{ij}	the ij^{th} component of dissipation rate tensor	$[m^2/s^3]$
$\tilde{\varepsilon}_{ij}$	the ij^{th} component of the modified dissipation rate tensor by intermittency	$[m^2/s^3]$
ε_m	loading coefficient in Moore's vortex	$[m^2/s^3]$
ε_ϕ	relative error of interpolated variable	[-]
ζ	coefficient in Moore's trailing vortex model	$[m^{1.5}/s]$
η	surface tension	[N/m]
Θ	the characteristic time scale of mean flow	[s]
θ	azimuthal coordinate	[rad]
$\dot{\theta}$	bubble angular velocity	[rad/s]
$\ddot{\theta}$	bubble angular acceleration	$[rad/s^2]$
$\dot{\theta}_{\text{flow}}$	flow angular velocity	[rad/s]
θ_{rel}	relative angular coordinate difference	[rad]
θ_{s}	settling azimuthal coordinate	[rad]
λ	deduction coefficient in azimuthal velocity	[-]
μ	carrier-fluid dynamic viscosity	[Pa s]
μ_{t}	eddy dynamic viscosity	[Pa s]
ν	total kinematic viscosity	$[m^2/s]$
ν_{l}	liquid-phase kinematic viscosity	$[m^2/s]$
ν_{t}	eddy kinematic viscosity	$[m^2/s]$
$\bar{\bar{\xi}}$	the centroid of the vorticity	[m]
ξ	spanwise coordinate	[m]
Π_i	Buckingham Π variable	[-]
Π_{ij}	the ij^{th} component of specific pressure-strain correlation tensor	$[m^2/s^3]$
$\tilde{\Pi}_{ij}$	the ij^{th} component of the modified specific pressure-strain correlation tensor by intermittency	$[m^2/s^3]$
ρ	carrier fluid density	$[kg/m^3]$

ρ_B	bubble density	$[kg/m^3]$
ρ_v	vapor-phase density	$[kg/m^3]$
σ	cavitation number	[-]
σ_d	coefficient of cross-diffusion	[-]
σ_f	coefficient of γ-diffusion	[-]
$\sigma_{\theta t}$	coefficient of $\tilde{\mathrm{Re}}_{\theta t}$-diffusion	[-]
σ_ω	coefficient of ω-diffusion	[-]
ς	viscous radius coefficient in Lamb-Oseen vortex	[-]
τ	the characteristic time scale of turbulence	[s]
τ_{ij}	fluctuation deviatoric stress tensor	[Pa]
τ_K	turbulence Kolmogorov time scale	[s]
τ_p	particle response time	[s]
Φ_p	volume fraction of disperse phase	[-]
$\bar{\Omega}$	vorticity magnitude	[1/s]
$\boldsymbol{\omega}$	vorticity vector	[1/s]
ω	specific turbulence dissipation rate	[1/s]
ω	vorticity magnitude	[1/s]
ω_{max}	maximum vorticity magnitude	[1/s]

This page intentionally left blank

MAIN BODY

1

INTRODUCTION

1.1 BACKGROUND

Underwater Radiated Noise (URN) has gained increased attention in recent years due to its harmful impact on the marine creatures (Bureau Veritas, 2019). The shipping industry, as a significant role in the sea, contributes to a notable portion. Understanding the cavitation provides insight into the unwanted impacts.

Cavitation is a phase change phenomenon. One could boil a bottle of water through raising the temperature. By contrast, cavitation converts liquid to vapor mainly with the pressure decrease, as Figure 1.1 shows. Consequently, it typically happens near the suction sides of blades or the vortex cores, where the lowest pressures occur. Figure 1.2 illustrates different cavitation types from sheet to tip vortex cavitation.

Cavitation is usually harmful to the marine propeller. Most propellers suffer from cavitation when reaching high loading or low ambient pressure scenarios. The phenomenon brings two main harmful aspects: cavitation erosion and sound emission. Among them, the sound emission initiates this research to understand more about the bubble behaviors.

Cavitation, in essence, is composed of the bubble growth, coalesce, and collapse. When bubble radius changes, which occurs in all stages, sounds will be emitted and usually become the dominant part of

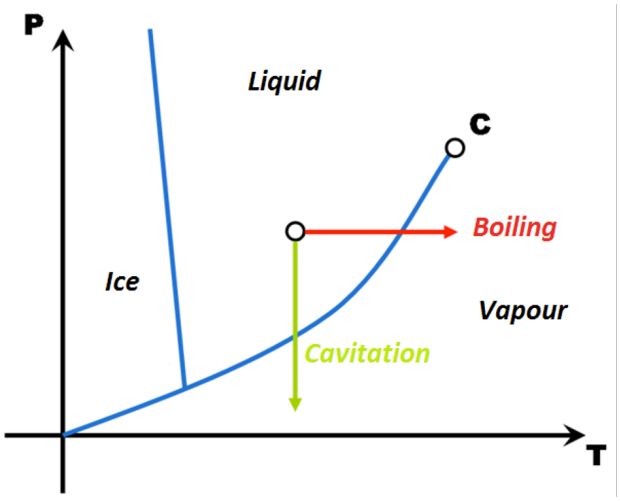

Figure 1.1: Phase change of water, retrieved from Asnaghi (2015).

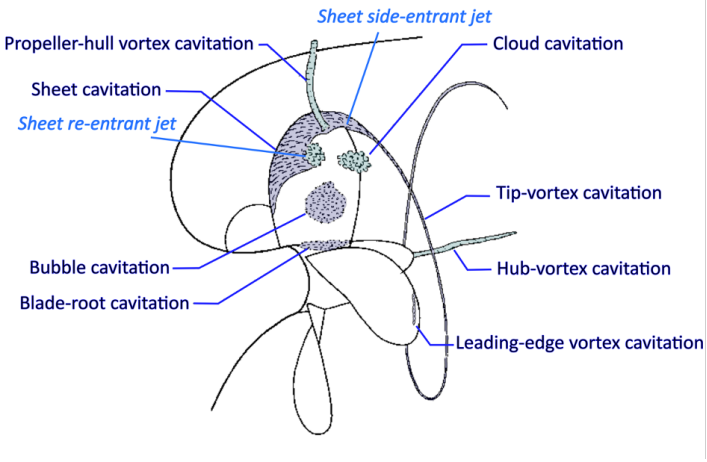

Figure 1.2: Types of cavitation around a propeller, originated from Propulsion Committee of 23rd ITTC (2002), and modified by Bosschers (2018).

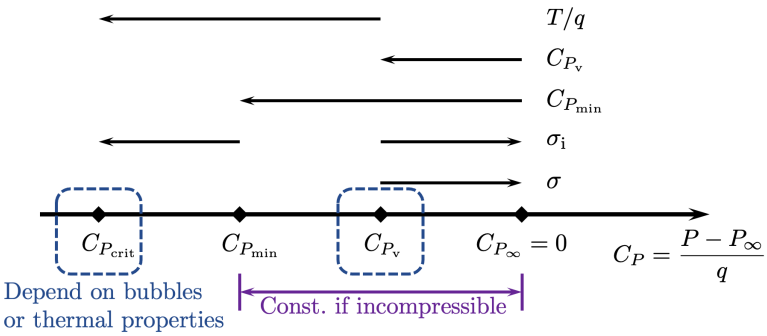

Figure 1.3: Relationships between pressure coefficients. The arrow describes the sign. The purple line is constant

the overall acoustic signature of the ship. The tip vortex cavity also yields noise, but this is due to the interface dynamics and interaction with the ambient turbulence. Still, it is a major contributor to the broadband noise (Bosschers, 2018; Pennings, 2016; van Wijngaarden *et al.*, 2005). As a result, an insightful understanding of tip vortex cavitation is essential, where the cavitation inception is one of the major topics.

Cavitation inception is influenced by many parameters such as ambient pressure, surface tension, bubble population, and viscosity effect.

A few pressure-related quantities are defined for further analyses. Figure 1.3 gives readers an overview. The minimum pressure coefficient is

$$C_{P_{min}} = \frac{P_{min} - P_\infty}{\frac{1}{2}\rho U_{ref}^2}, \tag{1.1}$$

where P_∞, ρ, and U_{ref} are the reference pressure, the liquid phase density and the reference velocity, separately. The minimum pressure usually occurs at the vortex centers during the tip vortex cavitation.

Cavitation, as a phase change phenomenon, should also take vapor pressure into account:

$$\sigma = -C_{P_v} = \frac{P_\infty - P_v}{\frac{1}{2}\rho U_{ref}^2}, \tag{1.2}$$

where P_v is the vapor (or sometimes called saturation) pressure. σ is named as the cavitation number since, empirically, the researchers find it is a critical quantity to characterize the cavitation phenomenon (Arakeri, 1979). P_{crit} is the critical pressure, which is the actual inception point. The inception point deviates from the vapor pressure because the actual bubble expansion dominates the inception phenomenon. Bubbles do not necessarily expand severely toward cavitating when the surrounding pressure drops to the vapor pressure since there are still other retarding parameters such as the surface tension.

The next quantity describes the relationship between vapor pressure and critical pressure, which is called tension or tensile strength[1]:

$$\begin{aligned} T &= P_v - P_{crit} \\ &= -q\, C_{P_{crit}} - P_\infty + P_v \\ &= -q\,(C_{P_{crit}} + \sigma)\,, \end{aligned} \tag{1.3}$$

where q is dynamic pressure at reference point, $\frac{1}{2}\rho U_{ref}^2$. The deviation, $P_v - P_{crit}$, increases if the amount of bubbles is limited or the bubble sizes are small since the surface tension is more dominant in the case. Also, fluid is traditionally called "strong" water if the tensile strength is high, while "weak" water is the other way around.

σ_i is the so-called cavitation inception number, to which the cavitation number has to drop such that the cavitation happens:

$$\sigma_i = \frac{P_\infty - P_v - (P_{min} - P_{crit})}{\frac{1}{2}\rho U_{ref}^2} \tag{1.4}$$

Supposed that the cavitation number is controlled by the reference pressure, i.e., the inflow velocity and the vapor pressure remain

1 Not to be confused by the terms, the tension and the surface tension are two totally different quantities.

constant. In that case, the cavitation inception number is the cavitation number when the minimum pressure coincides with the critical pressure. Note that for a normal cavitation tunnel flow field, which is usually considered incompressible, $P_\infty - P_{\min}$ is a constant if the flow kinematic does not alter so that the minimum pressure will move simultaneously and equally with the reference pressure. If the inception pressure equals the vapor pressure, the inception number is just the negative minimum pressure coefficient.

As briefly mentioned, the critical inception pressure is not necessarily the vapor pressure. The vapor pressure is an approximated criterion when only a little information is known. There are other factors that restrict or promote bubbles' growth, such as tensile strength, residence time effect, contaminant gas, or turbulence (Brennen, 2013).

The role of bubble-surrounding pressure is pronounced. If pressure drops below the critical pressure, cavitation is likely to happen because bubbles will grow rapidly, so one can observe them. Khoo *et al.* (2021) confirm that the pressure indeed plays a significant role in tip vortex cavitation inception by measuring the flow field around the tip vortex generated by a hydrofoil. The bubble at the near downstream is more likely to cavitate and is less sensitive to external conditions because the pressure at the vortex center reaches its minimum at around 0.0-0.2c_0 downstream, where c_0 represents the root chord length. The minimum pressure value is sufficiently low, so the change of the ambient pressure and cavitation number and the turbulence pressure fluctuation still cannot elevate the surrounding pressure over the critical pressure.

As suggested by Maines and Arndt (1993), tip vortex cavitation inception consists of four stages:

1. Spherical nucleus entrainment,
2. Spheroidal bubble growth,
3. Transitional phase,
4. Cylindrical bubble growth.

From the stages, it could be observed that the ambient bubble population is a critical factor affecting cavitation inception. Asnaghi *et al.* (2018) even apply it directly as an inception prediction method. The bubble population affects cavitation inception mostly at the first stage, i.e. the entrainment of nuclei into the. Bubble capture could be described by the entrapment time, which is a function of initial bubble radius, bubble distance to vortex center, vortex size, and vortex core strength (Ligneul & Latorre, 1993; Oweis *et al.*, 2005). Khoo *et al.* (2021) investigates bubble population effect on the capturing event and the activation rates (when the cylindrical bubble growth is observed) via the polydisperse population under $\mathcal{O}(10)$ μm and the monodisperse population at $\mathcal{O}(100)$ μm[2]. They show that the activation rate of large bubbles is higher than that of smaller bubbles by about one order. Chen *et al.* (2019) demonstrates that capture and rapid growth mainly happens at $\mathcal{O}(30)$ μm. Nevertheless, they assume that the larger bubbles are less abundant than the smaller ones, so the initial radial distances of large bubbles are greater than those of the smaller ones, which is a doubtful coupling hypothesis. As a result, it is anticipated that the result might be biased and not as representative as the others. On the other hand, Gindroz and Billet (1998) directly points out that 59% of the cavitation index reduction is found with increasing the liquid tensile strength (lower the gas content).

All in all, developing an understanding of bubble entrapment within the tip vortex is a key to understanding cavitation inception and the social impacts, such as the noise mentioned before.

In an experiment, all physics are, in principle, included. However, it suffers from some unavoidable drawbacks, such as the scaling effect and inability of measuring the detailed bubble population and paths. Although the numerical simulation is incomplete due to uncertainties and modeling errors, it can provide helpful insight if the result is verified and validated correctly. Therefore, this research investigates the bubble behavior around the tip vortex via a numerical approach.

2 Polydisperse distribution means bubble sizes do not concentrate near a value but a broad spectrum, while monodisperse distribution does have a narrow peak in its size spectrum.

1.2 RESEARCH OBJECTIVES

> How will bubbles (nuclei) behave when they interact with a tip vortex?

1. What are the roles and effects of different force terms on bubble behavior?

   Expanding the understanding of the force's role could assist to build more robust models to explain the interesting phenomena.

   Abdel-Maksoud *et al.* (2010) and Peters and el Moctar (2020) investigate bubble behavior under different formulations, such as one with pressure gradient force being neglected. Inspired by them, it is curious what the other forces' roles in the bubble motions are with a far more rigorous investigation.

2. What is the effect of initial bubble properties on entrapment time?

   The entrapment time is one of the essential physical quantities related to the bubble capture, as mentioned in Chen *et al.* (2019) and Khoo *et al.* (2021). The bubbles of different sizes are released in different locations relative to the vortex core, as Oweis *et al.* (2005) have done before. Still, this research would like to focus on not only the numerical part but also the analytical part. The development of the analytical part could be assisted by the knowledge acquired by the previous sub-question. This research question could potentially help estimate the "influence zone," where bubbles are captured throughout traveling times.

3. What is the bubble population of each section?

   Many researchers such as Khoo *et al.* (2021) have pointed out that the bubble population is important to understand tip vortex inception and its scale effect. Hsiao *et al.* (2006) and Ku *et al.* (2020) investigate the bubble-induced noises via tracking

bubbles from the upstream to downstream, through which they either explicitly or implicitly discover the bubble population at some streamwise sections. However, a further study on this topic is in favor: what happens around the location of the tip vortex core and what the effects of upstream ambient bubbles are. This question relates to the previous one since the migration velocities toward the core of different sizes influence bubble populations as they go downstream. The question can also shed some light on the cavitation inception hotspots.

4. To what extent can the numerical simulation resemble the experimental measurement in the context of the bubble motion around the tip vortex?

   Only few researchers, such as Oweis *et al.* (2005), perform decent comparisons between the simulates and experimental results. Furthermore, when it comes to the bubble population comparison, the number of related studies become even less. Therefore, this study also carries out a preliminary comparison research with the a statistical approach proposed by Ir. Nanda.

1.3 CASE PLAN

This research plans to carry out several cases to answer the research questions and objectives.

A CFD case simulating the tip vortex could increase the understanding of the bubble population evolution and the experimental comparison. However, it is necessary to isolate the tip vortex from the propeller rotation motion to prevent excessive computational effort. Two experimental setups are proposed to avoid the motion: half-span lifting elliptical wing and converging-diverging nozzle (Arndt *et al.*, 1991; de Montgolfier, 2011; van den Boogaard, 2019). Among, the elliptical wing gained more attention, and several related experiments have been done (Arndt *et al.*, 1991; Khoo *et al.*, 2021; Ku *et al.*, 2020;

Peng *et al.*, 2017; Pennings, 2016). As a result, the elliptical wing case is chosen, especially the "Arndt" wing[3].

"Arndt" wing configuration in the old TU Delft cavitation tunnel is applied to perform the numerical simulation. Researchers such as Nanda *et al.* (2022) and Pennings (2016) have performed detailed measurements on tip vortex cavitation or bubble trajectories near the vortex center or cavity. Numerically, the tip vortex cavitation of the wing has also been under intensive investigation these days, such as Asnaghi *et al.* (2020), Klapwijk (2021), and Liebrand *et al.* (2020), on which the Eulerian simulation could conveniently be based.

However, a more controlled flow field should also be implemented to examine the influences of different parameters and to perform the force analysis. As a result, aside from the CFD tip vortex simulation, bubble motion in the Lamb-Oseen vortex will also be carried out.

1.4 THESIS STRUCTURE

The master thesis is divided into several chapters. First, Chapter 2 carries out an extensive literature review of why specific approaches are chosen and then elaborates on them. Successively, Chapter 3 tries to verify and validate both the methodologies and implementations of the Eulerian and Lagrangian parts. Chapters 4 and 5 together approaches the research targets by applying both the theoretical and simulated vortex flow fields. Next, Chapter 6 organizes all the results from the previous chapters and answers the proposed research questions from a more aerial perspective. Finally, Chapter 7 sums up the research and addresses some critical research questions to be answered in the future.

3 "Arndt" wing is named after Prof. Roger E. A. Arndt, who firstly carried out a series of extensive cavitation studies with the given hydrofoil: NACA66_2-415 (Arndt *et al.*, 1991).

This page intentionally left blank

2

METHODOLOGY

This chapter describes why the specific approaches and settings are chosen to tackle the problems at hand.

The reason for choosing the one-way coupling Eulerian-Lagrangian method is first argued. Successively, the two composite parts are addressed: the Eulerian flow simulation and Lagrangian Particle Tracking (LPT). The Eulerian part takes care of the background flow field simulation, while bubbles are traced via the latter approach.

2.1 BUBBLE-FLOW COUPLING

Modeling the bubble motion in the flow field has long been challenging, especially in the cavitation inception research. Performing accurate simulations while maintaining a reasonable computational effort stimulates the growth of different approximations toward the scenario.

Three categories of numerical multiphase approaches are developed: Eulerian mixture, Euler-Euler, and Eulerian-Lagrangian. Note that there are few alternative nomenclatures for every single category. They are sometimes even inter-used, such as Eulerian mixture and Euler-Euler approaches. Those terms in the following will be distinguished to the best.

2.1.1 *Eulerian mixture approach*

Eulerian mixture regards all fluids in flow as a single mixture fluid with properties mixed from the composing fluids. An indicator function controls the mixture state. There is still one set of flow dynamics governing equations but with an additional transport equation describing the advection of the indicator functions, which is defined differently among models.

One of the most used models is Volume of Fluid (VOF) developed by Hirt and Nichols (1981). It features a low memory requirement and the suitability on a fixed grid. However, regarding the bubble-flow scenario, it is not advisable. In seas and the cavitation tunnels, bubble sizes range from microns to millimeters, implying that the computational grids should be on the micrometer scale. Modeling bubbles in millimeters is still feasible for the current computer. However, the resolution around micrometers has already approached that of Direct-numerical Simulation (DNS), which is undesirable to many current computational powers (Cifani, 2017; Fedkiw *et al.*, 1999; Osher & Fedkiw, 2001).

2.1.2 *Euler-Euler approach*

Euler-Euler method, sometimes also called the Eulerian-Eulerian method, considers each fluid flow separately instead. Each fluid has its own set of governing equations. They are judiciously coupled with the slip velocity between different fluids, same pressure field shared by each fluid, and approximated momentum exchange such as drag, virtual mass, and lift forces (Afolabi & Lee, 2014; Sokolichin *et al.*, 1997). The method is primarily adopted and developed by chemical engineering and nuclear reactor simulation (Sokolichin *et al.*, 1997).

However, these additional advantages do not extend its usability out of the large cavities or statistical bubble cloud motions. To capture the individual bubble motion, the grids are again required to approach the targeted bubble size, which is unreasonable. Also,

initially designed for the bubble clouds, the momentum exchange modeling will turn into a hindrance without careful treatment down to the bubble scale. The comparison of the Eulerian mixture and Euler-Euler methods could be found in Bertolotti *et al.* (2021).

Note that terminologies of "Euler-Euler" and "Eulerian mixture" are sometimes misused together, such as Peters (2019) and Yakubov *et al.* (2011). The ambiguous usage of these two terms might stem from Černe *et al.* (2001) idea to couple VOF and two-fluid Euler-Euler together, which is further modified by Wardle and Weller (2013) and Weller (2008), and is merged in a widely-spread open-source toolbox, Open∇FOAM®.

2.1.3 *Eulerian-Lagrangian approach*

Borrowing the concept from the particle-flow interaction, the Eulerian-Lagrangian method simulates background carrier flow via standard continuum fluid methods, i.e., the Eulerian approach, while bubbles, the dispersed phase, are tracked by Lagrangian equations. In consequence, it is sometimes called Discrete Bubble Model (DBM) (Ghahramani & Bensow, 2016) if it is the bubble being tracked. Since an normal grid size is enough, the Eulerian-Lagrangian approach is the most prominent one to track individual bubbles.

Johnson Jr. and Hsieh (1966) is one of the first who applies the approach in the cavitation inception simulation. Hsiao and Pauley (1999) and Latorre (1982) have also investigated tip vortex cavitation via the scheme.

It assumes that bubbles and flow are only weakly-nonlinearly coupled so that the bubble motions could be separated from the flow field with only some source corrections (Xu *et al.*, 2002), local density difference (Finn *et al.*, 2011; Ma *et al.*, 2015) or even without any correction added into flow momentum equations. Depending on the interactions and corrections added between the phases, there are one-way (carrier flow toward bubbles), two-way (carrier flow to bubble and the other way around), and four-way couplings (two-way

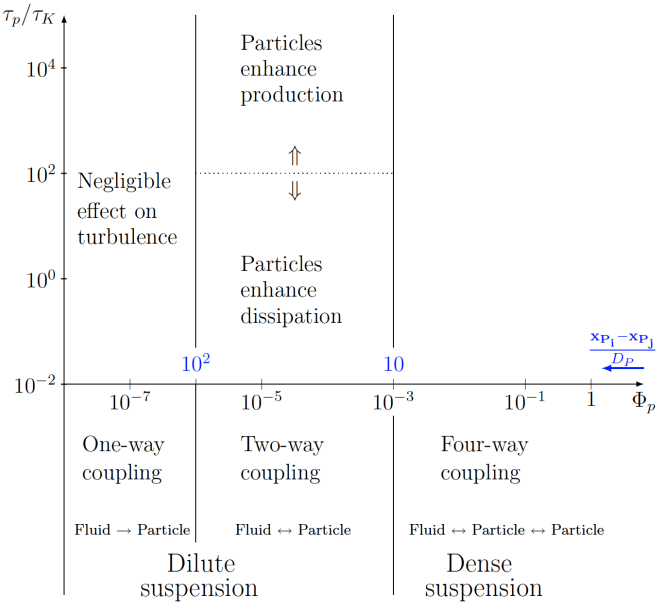

Figure 2.1: Map of flow regimes in particle-laden flows, originally proposed by Elghobashi (1994) and further adapted by Vallier (2010). Φ_p is the volume fraction of the dispersed phase in the interested region. τ_p/τ_K is the ratio of particle response time (in Stokes limit) to turbulence Kolmogorov time scale.

along with the bubble-bubble inter-couplings). The complexity and computational requirement grow from one- to four-way coupling schemes.

Elghobashi (1994) divides method regimes based on the volume fraction, as shown in Figure 2.1. Although initially proposed for the particle-laden flow, it is reasonable to extrapolate the scheme to the bubble flow. The bubble does not grow explosively in the capturing stage, so the initial volume fraction is nominal enough. As calculated from Hsiao *et al.* (2006) and Khoo *et al.* (2021), the volume fractions of disperse phase all fall below 10^{-6}; therefore, the one-way coupling is enough.

Recently, researchers have developed a family of methods that can exchange bubble simulation between Eulerian and Lagrangian meth-

ods, which is the so-called hybrid or multi-scale Eulerian-Lagrangian (Hsiao *et al.*, 2017; Lidtke, 2017; Vallier, 2013). If a bubble grows to a size large enough to cover several cells, the Eulerian mixture takes over, while a bubble will return to the Lagrangian control if it shrinks too much. The method can also specify the slip velocity, which is essential for the accuracy (Hsiao *et al.*, 2017). The aforementioned researchers reported promising noise or flow characteristics results compared to the experimental counterparts. However, some issues, such as the sudden pressure waves during transition times from Eulerian to Lagrangian frameworks, still need to be addressed (Ghahramani & Bensow, 2016). Furthermore, the switch between Eulerian and Lagrangian reference frames should also be investigated more since the transition based purely on grid size is not physical.

This research will apply the pure one-way coupling Eulerian-Lagrangian method since tracking bubbles individually are of the most interest considering the research questions. Also, it could save the computation loading quite a bit.

2.2 EULERIAN FLOW SIMULATION

This section addresses the flow governing equations and the important closure strategies – turbulence models. It is noted that the tip vortex cavitation inception does not involve any large cavity at the beginning stage, so the fully-wetted flow is chosen instead of a cavitating tip vortex flow.

2.2.1 *Flow field governing equations*

The fluid flow is governed by the mass and momentum conservation, i.e., Navier-Stokes equations. Mass conservation equation, also known as the continuity equation, reads

$$\frac{\partial \rho}{\partial t} + \frac{\partial \rho U_i}{\partial x_i} = 0, \tag{2.1}$$

where t denotes time, ρ the fluid density, U_i the i^{th} component of the flow velocity, and x_i the i^{th} component of the Cartesian coordinates.

The momentum conservation is governed by the Navier-Stokes equations of Newtonian fluid:

$$\frac{\partial \rho U_i}{\partial t} + \frac{\partial \rho U_i U_j}{\partial x_j} = -\frac{\partial P}{\partial x_i} + \frac{\partial T_{ij}}{\partial x_j}, \tag{2.2}$$

where P denotes the static pressure, and T_{ij} the deviatoric stress tensor reads

$$T_{ij} = \mu \left(2S_{ij} - \frac{2}{3} \frac{\partial U_m}{\partial x_m} \delta_{ij} \right), \tag{2.3}$$

of which μ is the liquid-phase dynamics viscosity, $2/3$ is an assumed constant by Stokes, and the strain rate tensor is defined as

$$S_{ij} = \frac{1}{2} \left(\frac{\partial U_i}{\partial x_j} + \frac{\partial U_j}{\partial x_i} \right). \tag{2.4}$$

The present Navier-Stokes equations are of the compressible form but it could also successfully describe the incompressible flow in the current case.

2.2.2 *Turbulence models*

CFD encounters a critical challenge when the Reynolds number (Re) increases. The nonlinear nature of the convective term gives rise to turbulence and energy cascade, hence introducing the scale separation (Nieuwstadt *et al.*, 2016). CFD has to increase its grid resolution to resolve the viscous dissipation range (Kolmogorov scale), the most miniature scale of the energy cascade. Also, the time step is confined by the dissipation time scale and Courant number[4]. In a typical cavitation tunnel scale, the Reynolds number is approximately 10^5-10^6, requiring computational effort only affordable for a supercomputer.

As a result, proper transition and turbulence modelings are important in CFD field, not to mention simulating the present case.

Turbulence models divide, either in spatial or temporal domains, flow field variables (Φ) into time- or spatial-averaged/filtered ($\langle\Phi\rangle$) and fluctuation/residual (ϕ) parts. They aim to model the nonlinear fluctuation interaction part from the filtered/averaged, i.e., resolved part.

Reynolds-averaged Navier-Stokes (RANS) method family averages flow variables either within a period of time or with several ensembles, so the resolved part is usually called time/ensemble-averaged quantity, and the unresolved one is the fluctuation. On the other hand, Large-eddy Simulation (LES) or other related approaches filter flow fields spatially with a convolution kernel. Therefore, the resolved and unresolved quantities are called filtered and residual parts. However, in mathematics, they have the same form of $\Phi = \langle\Phi\rangle + \phi$, so the symbols remain the same intentionally. Also, unified names of the "resolved" and "unresolved" to the symbols will be applied for simplicity.

In order of reducing the minimum resolved scale, categories of turbulence models may be listed as: potential flow (no turbulence modeling), RANS equations, hybrid models, bridging models, LES, and DNS. Typical tip vortex cavitation simulations limit themselves from RANS to LES (Asnaghi *et al.*, 2017b; Salvatore *et al.*, 2009). In the following, the pros and cons of each turbulence model applied in the tip vortex cavitation simulation will be addressed. Also, since the Eulerian-Lagrangian approach is applied, the multiphase correction in turbulence models will not be reviewed.

RANS modeling is the most developed since the early day (Boussinesq, 1877; Reynolds, 1895). The Reynolds-averaging procedure is applied to the governing equations, and thus the flow variables (Φ)

4 Indeed, implicit time integration schemes do not require Courant–Friedrichs–Lewy (CFL) condition to maintain stability. However, accuracy is still achieved by small time step sizes.

are separated into two components, the mean ($\langle\Phi\rangle$) and fluctuation (ϕ) parts:

$$\langle\Phi(t)\rangle = \frac{1}{\mathcal{T}}\int_{t-\mathcal{T}}^{t}\Phi(s)\,\mathrm{d}s\,, \quad \text{with} \quad \tau \ll \mathcal{T}, \tag{2.5}$$

$$\phi(t) = \Phi(t) - \langle\Phi(t)\rangle\,, \tag{2.6}$$

where τ is the characteristic time scale of the fluctuation, $\mathcal{T}$ is the averaging window such that it is long enough to rule out the fluctuation but short enough to preserve the unsteady flow properties: $\tau \ll \mathcal{T} \ll \Theta$, where Θ is the characteristic timescale of the mean flow. According to the process, flow variables are expressed in the following fashion:

$$\begin{aligned} U_i &= \langle U_i\rangle + u_i, \\ P &= \langle P\rangle + p, \\ T_{ij} &= \langle T_{ij}\rangle + \tau_{ij}, \\ S_{ij} &= \langle S_{ij}\rangle + s_{ij}. \end{aligned}$$

The capitalized and lower cases represent the resolved and unresolved parts of the physical quantities, respectively.

The mean flow continuity and RANS equations read

$$\frac{\partial\rho}{\partial t} + \frac{\partial\rho\langle U_k\rangle}{\partial x_k} = 0, \tag{2.7}$$

$$\frac{\partial\rho\langle U_i\rangle}{\partial t} + \frac{\partial\rho\langle U_j\rangle\langle U_i\rangle}{\partial x_j} = -\frac{\partial\langle P\rangle}{\partial x_i} + \frac{\partial\langle T_{ij}\rangle - \rho R_{ij}}{\partial x_j}, \tag{2.8}$$

where the Reynolds stress is expressed as

$$\rho R_{ij} = \langle\rho u_i u_j\rangle\,. \tag{2.9}$$

Another constitutive relationship is necessary to estimate the Reynolds stress. Boussinesq (1877) proposes a hypothetical relationship between the Reynolds stress and the mean flow strain rate, and it is named the "linear" eddy viscosity model family since he assumes that the deviatoric Reynolds stress is directly proportional to

and aligned with the mean deviatoric flow strain rate with an eddy viscosity, ν_t (Gatski & Rumsey, 2002):

$$-R_{ij} + \frac{1}{3}R_{ii}\delta_{ij} = \nu_t \left(2\left\langle S_{ij} \right\rangle - \frac{2}{3}\frac{\partial \left\langle U_m \right\rangle}{\partial x_m}\delta_{ij} \right). \tag{2.10}$$

The rest for models to fill up is how to estimate the eddy viscosity. There are generally algebraic, one- and two-equation models in this family.

The algebraic and one-equation models are proven to be insufficient to resolve the tip vortex flow. Mohamed *et al.* (2009) states that Spalart-Allmaras, a famous one-equation turbulence model, will result in an excessive viscous dissipation because the existing flow vortex maintains a strong positive production term of the turbulent viscosity coefficient. Therefore, the tip vortex further downstream will disappear.

Two-equation models offer several options but also suffer from different extents of over turbulent diffusion. One underlying reason is that the high gradient regions such as the tip vortex core do not necessarily contribute to the turbulence generation (Nieuwstadt *et al.*, 2016).

The standard k-ε model cannot even give a convergent result and also predict the excessive turbulent kinetic energy near blade surfaces (Kim *et al.*, 2017; Ku *et al.*, 2020). The realizable k-ε model can capture the vortex structure but again is haunted by the drawback (Ku *et al.*, 2020).

k-ω family, another one of the most applied eddy-viscosity models (Terziev *et al.*, 2020), also gives rise to the same problem. The original k-ω is very sensitive to the freestream turbulence value (Menter, 1992), so it is not considered in the discussion. Instead, the blending one, k-ω Shear-stress Transport (SST) model, is mainly applied in the literature. However, k-ω SST severely underpredicts the azimuthal velocity around the tip vortex and again suffers from the high level of the turbulence viscosity.

k-$\sqrt{k}L$ model, which is also developed by Dr. Menter (Egorov *et al.*, 2010; Menter & Egorov, 2010; Menter *et al.*, 2006), aims to include the scale-resolving property by von Karman length scale and to improve the convergence behavior (Klapwijk, 2021) It is expected to perform better than k-ω SST model. Still, Liebrand *et al.* (2020) points out the general behaviors resemble k-ω SST model.

"[For the linear eddy-viscosity models, two] of the most notable deficiencies are the isotropy of the eddy viscosity and the material-frame indifference of the models. The isotropic eddy viscosity is a consequence of the Boussinesq approximation, which assumes a direct proportionality between the turbulent Reynolds stress and the mean strain rate field. The material frame-indifference is a consequence of the sole dependence on the (frame-indifferent) strain rate tensor. These deficiencies preclude, for example, the prediction of turbulent secondary motions in ducts (isotropic eddy viscosity) and the insensitivity of the turbulence to noninertial effects such as imposed rotations (material frame-indifference). Remedies for these deficiencies can be made on a case-by-case or ad hoc basis; however, within the framework of a linear eddy viscosity formulation such defects cannot be fixed in a rigorous manner" (Gatski & Rumsey, 2002). Liebrand *et al.* (2020) also indicates that linear viscosity models cannot satisfy the accuracy of the detailed velocity field near the tip vortex cavitation but can only predict integral quantities such as the lift coefficient.

Contrary to the linear eddy viscosity model, the nonlinear one tries to exploit as much as possible the other characteristics of the strain rate tensor, such as the ten invariant tensor bases, to avoid the false alignment assumption between the stress and strain rate tensors. One of them is Explicit Algebraic Reynolds Stress Model (EARSM). This model obtains each Reynolds stress individually and introduces the skew-symmetric part of the mean stress tensor into the relationship. Certainly, EARSM demonstrates anisotropy of Reynolds stresses. However, the lift coefficient is underpredicted by about 10%, so the azimuthal and axial velocities are doubtful (Liebrand *et al.*, 2020). Still, the same author points out that EARSM is more optimistic than the linear model due to its anisotropy nature.

Another category of RANS models circumvents the necessity of the direct relationship between the resolved and unresolved tensors. Instead, they directly resort to the analytical Reynolds stress equations. Reynolds Stress Model (RSM) solves transport equations for each Reynolds stress component. Inherently, the model also captures the anisotropy nature and should be more accurate than EARSM. Some scholars state RSM seems to perform better in wetted tip vortex flow (still not sufficiently validated), but cavitation behavior is still similar to the linear model (Ku *et al.*, 2020; Liebrand *et al.*, 2020). However, the others report that RSM indeed succeeds in the validation (Park *et al.*, 2021).

Until now, RANS models assume the turbulent boundary layer covers the whole chordwise. However, the transition between laminar and turbulent flow is inevitable, especially in such a model scale for the cavitation tunnel. Therefore, Lopes (2021) argues that a transition model is necessary to consider the transition, separation, and reattachment. γ-$\tilde{\mathrm{Re}}_{\theta t}$ model is proven to be the most robust and succeed in improving results compared to one without a transition model. The model falls in the category of Local Correlation-based Transition Model (LCTM) since it considers the transition phenomenon individually for each location, which is also the advantage of the model. However, it is still not mature yet. The performance of the transition model is highly influenced by the inflow turbulence, convection discretization scheme and so on (Lopes, 2021). Also, it is hard to converge because transition points keep jumping between two streamwise adjoined cells due to the switchers in the related equations (Liebrand, 2019).

Aside from RANS, LES is also widely applied in the field. Compared to the RANS simulation, LES can predict the cavity interface dynamics, 3D rotation motion and even the meandering vortex (Paskin *et al.*, 2019; Xie *et al.*, 2021). Moreover, the result is appropriately validated against the experimental result (Asnaghi *et al.*, 2020; Paskin *et al.*, 2019; Xie *et al.*, 2021). However, the computational time is considerably larger compared to RANS.

Hybrid models balance LES's accuracy and RANS's computational efficiency. RANS is applied to predict the near-wall region, while

LES for the outer part. To name just a few, Detached-eddy Simulation (DES), Delayed Detached-eddy Simulation (DDES), and Improved Delayed Detached-eddy Simulation (IDDES) all fall in this category. Several scholars report quite optimistic results with each method named above, especially for the DDES and IDDES (Liebrand *et al.*, 2020; Paskin *et al.*, 2019). However, the commutation error is not well assessed, so the result might still be falsely correct (Liebrand *et al.*, 2020).

The bridging model is also a category able to balance the computational efficiency. Partially-averaged Navier-Stokes (PANS) equations are one of the bridging models. To the author's knowledge, the method is applied to the tip vortex cavitation only by Klapwijk *et al.* (2021), and is temporally summarized in Klapwijk (2021). Its advantage over the hybrid model is that there is no commutation error if the modeled-to-total ratio remains constant. Besides, it is easier to estimate the discretization error because of an explicit modeled-to-total ratio set. In contrast, LES sometimes even directly couples discretization error into computation such as Implicit Large-eddy Simulation (ILES). However, PANS shows an advantage only for the wetted flow, while the velocity profiles are similar to IDDES one in the cavitating flow. Also, an extra inflow turbulence generator is vital to trigger cavity dynamics in both PANS and IDDES (Klapwijk, 2021).

This study plans to use RSM because it is accurate enough and capable of capturing the anisotropic nature of the tip vortex in the steady state without increasing too much computational requirement. Also, the γ-$\tilde{\mathrm{Re}}_{\theta t}$ are applied to account for the transition effect.

2.2.3 *Reynolds-stress Model*

If not explicitly stated, the theory is highly based on Rumsey (2017, 2022). The Reynolds stress has a set of exact transport equations by subtracting the averaged equations from the original Navier-Stokes equations and then multiplying the resulting equation by the

fluctuation velocity components. The transport equation is generally formulated as (Cécora *et al.*, 2012; Wilcox, 2006)

$$\frac{\partial \rho R_{ij}}{\partial t} + \frac{\partial \rho \langle U_k \rangle R_{ij}}{\partial x_k} = \rho P_{ij} + \rho \Pi_{ij} - \rho \varepsilon_{ij} + \rho D_{ij} + \rho M_{ij}. \tag{2.11}$$

BRIEF INTRODUCTION TO THE TERMS ρP_{ij} denotes the production term,

$$\rho P_{ij} = -\rho R_{ik} \frac{\partial \langle U_j \rangle}{\partial x_k} - \rho R_{jk} \frac{\partial \langle U_i \rangle}{\partial x_k}, \tag{2.12}$$

and it is exact since mean velocities gradients are resolved. The turbulent pressure-strain term reads

$$\rho \Pi_{ij} = \left\langle p \left(\frac{\partial u_i}{\partial x_j} + \frac{\partial u_j}{\partial x_i} \right) \right\rangle, \tag{2.13}$$

which represents a redistribution of turbulence kinetic energy to different directions, and the closure requires the most attention. Also, an additional dilatation term should be included if it is a compressible flow. The dissipation term of molecular viscosity and turbulence fluctuations is defined as

$$\rho \varepsilon_{ij} = \left\langle \tau_{ik} \frac{\partial u_j}{\partial x_k} \right\rangle + \left\langle \tau_{jk} \frac{\partial u_i}{\partial x_k} \right\rangle. \tag{2.14}$$

The diffusion term

$$\begin{aligned} \rho D_{ij} = &-\frac{\partial}{\partial x_k} \left(\langle \rho u_i u_j u_k \rangle \right) && \dots \rho \mathcal{T}_{ij} \\ &+\frac{\partial}{\partial x_k} \left(\langle \tau_{ik} u_j \rangle + \langle \tau_{jk} u_i \rangle \right) && \dots \rho D_{ij}^{\mathrm{v}} \\ &-\frac{\partial}{\partial x_k} \left(\langle p u_i \rangle \delta_{jk} + \langle p u_j \rangle \delta_{ik} \right) && \dots \rho D_{ij}^{\mathrm{p}}, \end{aligned} \tag{2.15}$$

is composed of the turbulent transport, $\rho \mathcal{T}_{ij}$, the viscous diffusion ρD_{ij}^{v}, and the pressure diffusion, ρD_{ij}^{p}, while the pressure diffusion term is usually neglected (Wilcox, 2006). The final term

$$\rho M_{ij} = \langle u_i \rangle \left(-\frac{\partial \langle P \rangle}{\partial x_j} + \frac{\partial \langle T_{jk} \rangle}{\partial x_k} \right) + \langle u_j \rangle \left(-\frac{\partial \langle P \rangle}{\partial x_i} + \frac{\partial \langle T_{ik} \rangle}{\partial x_k} \right) \tag{2.16}$$

stands for the compressibility and is again neglected here.

MODELING OF THE TERMS The production term has enough information from the mean flow, so no modeling is required. The dissipation is modeled via

$$\rho\varepsilon_{ij} = \frac{2}{3}\rho\varepsilon\delta_{ij}, \tag{2.17}$$

where the isotropic turbulent dissipation rate reads $\varepsilon = C_\mu k\omega$, and the turbulent kinetic energy is defined as $k = R_{ii}/2$. The pressure-strain correlation term is expressed in a very complicated fashion (Launder *et al.*, 1975; Speziale *et al.*, 1991):

$$\begin{aligned}\rho\Pi_{ij} = &-\left(C_1\rho\varepsilon + \frac{1}{2}C_1^*\rho P_{kk}\right)a_{ij} \\ &+ C_2\rho\varepsilon\left(a_{ik}a_{kj} - \frac{1}{3}a_{kl}a_{kl}\delta_{ij}\right) \\ &+ \left(C_3 - C_3^*\sqrt{a_{kl}a_{kl}}\right)\rho k\left\langle T_{ij}\right\rangle \\ &+ C_4\rho k\left(a_{ik}\left\langle S_{jk}\right\rangle + a_{jk}\left\langle S_{ik}\right\rangle - \frac{2}{3}a_{kl}\left\langle S_{kl}\right\rangle\delta_{ij}\right) \\ &+ C_5\rho k\left(a_{ik}\left\langle W_{jk}\right\rangle + a_{jk}\left\langle W_{ik}\right\rangle\right),\end{aligned} \tag{2.18}$$

where they introduce the normalized Reynolds stress anisotropy tensor a_{ij} and the spin tensor W_{ij}[5]:

$$a_{ij} = \frac{R_{ij}}{k} - \frac{2}{3}\delta_{ij}, \tag{2.19}$$

$$W_{ij} = \frac{1}{2}\left(\frac{\partial U_i}{\partial x_j} - \frac{\partial U_j}{\partial x_i}\right). \tag{2.20}$$

C_i and C_i^* are the model coefficients which will be given in Appendix A. Meanwhile, the isotropic turbulent dissipation rate ε is modeled via an extra transport equation for the length scale, which will be elaborated soon. The diffusion term is modeled through a generalized gradient diffusion model (Daly & Harlow, 1970) without the pressure diffusion term:

$$\begin{aligned}\rho D_{ij} &= \frac{\partial}{\partial x_k}\left[\left(\mu\delta_{kl} + D\frac{\rho k R_{kl}}{\varepsilon}\right)\frac{\partial R_{ij}}{\partial x_l}\right] \\ &= \frac{\partial}{\partial x_k}\left[\left(\mu\delta_{kl} + D\frac{\rho R_{kl}}{C_\mu\omega}\right)\frac{\partial R_{ij}}{\partial x_l}\right].\end{aligned} \tag{2.21}$$

MODELING OF THE LENGTH SCALE The length scale is described by the dimensionless dissipation rate, which is similar to the original proposition of Wilcox (2006):

$$\frac{\partial \rho\omega}{\partial t} + \frac{\partial \rho \langle U_k \rangle \omega}{\partial x_k} = \frac{\alpha_\omega \omega}{k}\frac{\rho P_{kk}}{2} - \beta_\omega \rho \omega^2 + \frac{\partial}{\partial x_k}\left[\left(\mu + \sigma_\omega \frac{\rho k}{\omega}\right)\frac{\partial \omega}{\partial x_k}\right] + \sigma_d \frac{\rho}{\omega}\max\left(\frac{\partial k}{\partial x_j}\frac{\partial \omega}{\partial x_j}, 0\right). \quad (2.22)$$

All further details of the coefficients will again be given in Appendix A.

2.2.4 γ-$\tilde{\mathrm{Re}}_{\theta t}$ *LCTM model*

The description is highly based on Liebrand (2019), Lopes (2021), and Nie *et al.* (2018) if is not mentioned explicitly, while the detailed modelling constants are given in Appendix A. The model tries to control turbulence kinetic energy budgets by multiplying the sources and sinks in the Reynolds stress equations (see Equation 2.11) with an intermittency factor (γ) that indicates the level of the developed/developing turbulence:

$$\tilde{P}_{ij} = \gamma_{\text{eff}} P_{ij}, \quad (2.23)$$

$$\tilde{\varepsilon}_{ij} = \min(\max(\gamma_{\text{eff}}, 0.1), 1.0)\varepsilon_{ij}, \quad (2.24)$$

where γ_{eff} improves the simulated γ with several limiters, which will be detailed in the appendix. The pressure-strain correlation term is a redistribution term between the Reynolds stresses, which is also believed to alter in the laminar boundary layer, so

$$\tilde{\Pi}_{ij} = \gamma_{\text{eff}} \Pi_{ij}. \quad (2.25)$$

5 By the two aforementioned tensors, a velocity gradient is composed: $\frac{\partial U_i}{\partial x_j} = S_{ij} + W_{ij}$. That is, S_{ij} is the symmetric part of the full velocity gradient tensor while W_{ij} is the anti-symmetric part. Furthermore, the invariant bases of tensor are based on the S_{ij} and W_{ij} (Gatski & Rumsey, 2002; Pope, 1975).

INTERMITTENCY EQUATION The following transport equation describes the intermittency:

$$\frac{\partial \rho\gamma}{\partial t} + \frac{\partial \rho \left\langle U_j \right\rangle \gamma}{\partial x_j} = \rho P_\gamma - \rho E_\gamma + \frac{\partial}{\partial x_j}\left(\left(\mu + \frac{\mu_\mathrm{t}}{\sigma_f}\right)\frac{\partial \gamma}{\partial x_j}\right). \quad (2.26)$$

The source term is

$$P_\gamma = F_{\mathrm{length}} c_{a1} \bar{S} \left(\gamma F_{\mathrm{onset}}\right)^{0.5} \left(1 - c_{e1}\gamma\right), \quad (2.27)$$

where c_{e1} controls the upper bound of the intermittency. $\bar{S} = \sqrt{2\left\langle S_{ij}\right\rangle \left\langle S_{ij}\right\rangle}$ represents the strain rate magnitude. F_{length} and F_{onset} together determine the transition speed of the location. The destruction term in the equation aims to reduce the intermittency in the laminar boundary layer

$$E_\gamma = c_{a2}\bar{\Omega}\gamma F_{\mathrm{turb}}(c_{e2}\gamma - 1), \quad (2.28)$$

where the c_{a2} and c_{e2} are some constants, and the latter one control the minimum of E_γ to be $1/c_{e2}$. $\bar{\Omega} = \sqrt{2\left\langle W_{ij}\right\rangle \left\langle W_{ij}\right\rangle}$[6] represents the vorticity magnitude. F_{turb} maintains the turbulence in the turbulent boundary layer.

Other than that, the model also simulates the local transition Reynolds number to determine the onset criteria in the γ equation:

$$\frac{\partial \rho \tilde{\mathrm{Re}}_{\theta t}}{\partial t} + \frac{\partial \rho \left\langle U_j \right\rangle \tilde{\mathrm{Re}}_{\theta t}}{\partial x_j} = \rho P_{\theta t} + \frac{\partial}{\partial x_j}\left(\sigma_{\theta t}(\mu + \mu_\mathrm{t})\frac{\partial \tilde{\mathrm{Re}}_{\theta t}}{\partial x_j}\right). \quad (2.29)$$

The production term reads

$$P_{\theta t} = c_{\theta t}\frac{1}{\mathfrak{T}}\left(\mathrm{Re}_{\theta t}^{\mathrm{eq}} - \tilde{\mathrm{Re}}_{\theta t}\right)\left(1.0 - F_{\theta t}\right), \quad (2.30)$$

where $c_{\theta t}$ is a constant, $\mathfrak{T}$ introduces a time scale, while $\mathrm{Re}_{\theta t}^{\mathrm{eq}}$ and $F_{\theta t}$ shut down the production term in the free-stream.

6 $\bar{\Omega}$ instead of $\langle\Omega\rangle$ is applied here to represent the mean vorticity magnitude because the norm operation ($\sqrt{2\left\langle W_{ij}\right\rangle \left\langle W_{ij}\right\rangle}$) is by no mean linear, and thus $\langle\Omega\rangle$ makes no sense.

2.3 LAGRANGIAN PARTICLE TRACKING

Solving micro bubbles far under the grid scale is inefficient by brutally refining the grid. Instead, bubble equations are applied to track them directly, as mentioned in Section 2.1. Also, confined by the computational capacity and considering the cavitation inception scenario, only the one-way coupling is applied, which is essentially a post-processing procedure after the CFD simulation.

2.3.1 *Bubble motion equation*

The bubble motion equation describes how a bubble moves in a carrier fluid flow field. The equation form is first finalized in Tchen (1947) and corrected by Corrsin and Lumley (1956). They summarize Basset, Boussinesq and Oseen's works in the quiescent flow and extend the work toward a flowing background fluid. Johnson Jr. and Hsieh (1966) also propose another formulation that considers bubble expansions and contractions. However, not until Maxey and Riley (1983) was a comprehensive derivation based on Navier-Stokes equations via the perturbation method given. Most of the formulations are just the varied forms based on Johnson Jr. and Hsieh (1966) and Maxey and Riley (1983).

Bubble motion equations are generally in the form of

$$m_B \frac{d\mathbf{U}_B}{dt} = \mathbf{F}_A + \mathbf{F}_P + \mathbf{F}_S + \mathbf{F}_D + \mathbf{F}_L + \mathbf{F}_K + \mathbf{F}_H, \tag{2.31}$$

where m_B represents the net bubble mass and $\mathbf{U}_B$ the bubble velocity vector. The right-hand side represents the added mass force, pressure gradient force, hydrostatic force, drag force, lift force, Kelvin impulse force, and history force, one after another.

ADDED MASS FORCE Added mass, which has long been recognized since the potential flow theory, analogically indicates that the carrier fluid is displaced when the body or the flow accelerates:

$$\mathbf{F}_{\mathrm{A}} = -C_{\mathrm{AM}}\rho V_{\mathrm{B}}\left(\frac{\mathrm{d}\mathbf{U}_{\mathrm{B}}}{\mathrm{d}t} - \underline{\frac{\mathrm{d}\mathbf{U}}{\mathrm{d}t}}\right), \tag{2.32}$$

where C_{AM} is the added mass coefficient, V_{B} the bubble volume, and $\mathbf{U}$ the flow velocity vector. Meanwhile, there was a debate decades ago on which expression the underlined part should be (Thomas *et al.*, 1983, 1984),

$$\begin{aligned}
&\frac{\mathrm{D}\mathbf{U}}{\mathrm{D}t} && \left(= \frac{\partial \mathbf{U}}{\partial t} + \mathbf{U}\cdot\boldsymbol{\nabla}\mathbf{U}\right),\\
&\left.\frac{\mathrm{d}\mathbf{U}}{\mathrm{d}t}\right|_{\mathrm{B}} && \left(= \frac{\partial \mathbf{U}}{\partial t} + \mathbf{U}_{\mathrm{B}}\cdot\boldsymbol{\nabla}\mathbf{U}\right), \text{ or}\\
&\left.\frac{\mathrm{d}\mathbf{U}}{\mathrm{d}t}\right|_{\text{relative}} && \left(= \frac{\partial \mathbf{U}}{\partial t} + (\mathbf{U}_{\mathrm{B}} - \mathbf{U})\cdot\boldsymbol{\nabla}\mathbf{U}\right).
\end{aligned}$$

The first one represents the acceleration of a fluid parcel, the second one means the flow acceleration seen by the bubble, and the third one does not have any specific physical meaning. After a rigorous mathematical derivation, Auton *et al.* (1988) and Thomas *et al.* (1984) point out that the first one should be the correct formulation.

Sometimes, the underlined term is considered part of the pressure gradient force, such as Beelen (2018), Johnson Jr. and Hsieh (1966), and Ku *et al.* (2020). Nevertheless, in this research, the flow acceleration is left there and "the added mass force" refers to only the flow acceleration part if not explicitly mentioned. Meanwhile, the body acceleration part will be integrated into the left-hand side of Equation 2.31.

As for C_{AM}, it is a measurement of body bluntness (Magnaudet & Eames, 2000). The sphere's one is indeed 0.5 as derived from the potential flow formulation (Chang & Maxey, 1994). Although C_{AM} will vary with the distance toward the wall (Klaseboer *et al.*, 2014), it is assumed the bubble is sufficiently far from the boundary, and one can neglect the effect.

PRESSURE GRADIENT FORCE The pressure gradient force comes from the pressure difference between a sphere's front and rear parts. Intuitively, one will come up with the form of

$$\mathbf{F}_{\mathrm{P}} = -V_{\mathrm{B}} \boldsymbol{\nabla} P. \tag{2.33}$$

Nevertheless, Buevich (1966) points out, and Maxey and Riley (1983) completes the statement: "[the formulation of Tchen (1947) is] not consistent in that the effects of pressure gradient of the undisturbed flow have been singled out over the effects of viscous shear stress when in fact the two may well be comparable." According to them, the correct expression should be instead

$$\mathbf{F}_{\mathrm{P}} = \rho V_{\mathrm{B}} \frac{\mathrm{D}\mathbf{U}}{\mathrm{D}t}. \tag{2.34}$$

The researchers, who do not employ this and are based on Tchen (1947), still apply the simplified formulation such as Hsiao *et al.* (2006) and Johnson Jr. and Hsieh (1966). Still, the inferences from their results will not change a lot since the magnitudes of the other terms are usually negligible at a high Reynolds number. The difference between the two formulations will be investigated in this effort.

DRAG FORCE The drag force represents the viscous-pressure and friction drags exerted on an object. Intuitively, the boundary condition of a bubble surface could be assumed as the slip-wall if in ultra-clean carrier fluid so that the resulting coefficient will be different from the solid sphere particle (Brennen, 2013). Nevertheless, the Marangoni effect is also inevitable if surfactants are present in the fluid (Magnaudet & Eames, 2000). Motion-induced surfactant concentration at the rear part causes the pseudo-stress. Consequently, the stress-free condition is no longer applicable now; thus, the drag coefficient becomes comparable to the solid sphere one. It is safe to assume that the surfactant concentration and contamination sufficiently trigger the no-slip boundary condition in a usual cavitation tunnel and the sea environment. For the drag of a no-slip sphere, Goossens (2019) gives a comprehensive review on most of the applied empirical drag coefficients. Also, if the bubble is deforming, the drag coefficient would change. Since it is hard to track bubble shape

change, Dijkhuizen *et al.* (2010) and Roghair *et al.* (2011) propose to relate the change qualitatively/quantitatively to modified Eötvös number. However, the form change is not applicable in this study.

LIFT FORCE Shear-induced lift force (Saffman lift) resulting from vorticity surrounding the sphere is not given in Maxey and Riley (1983) because such a linearized Stokes flow cannot predict lateral force (Bretherton, 1962), and furthermore the downwash caused by the sphere bubble cannot be captured via the perturbation analysis. However, it is a vital force in the bubble motion and thus will be considered.

Sridhar and Katz (1995) carries out an experiment in which free bubbles are released in the horizontally rotating cylinder of fluid and measures forces from the bubble balance locations. The lift force yielded from their experiment differs from many existing analytical or numerical simulations. However, Oweis *et al.* (2005) says that the lift coefficient does not influence the final result much.

Another source of the lift force is the Magnus lift force from the self-rotation-induced circulation, but it is not considered here since, in reality, the bubble rotation caused by the interaction with other bubbles is more predominant (Beelen, 2018). Also, the rotational inertia of surfactants upon the bubble wall is negligibly small so that the solid-body rotation might be neglected.

KELVIN IMPULSE FORCE Kelvin impulse force starts from the original impulse formulation:

$$\mathbf{I} = C_{\mathrm{AM}} \rho V_{\mathrm{B}} (\mathbf{U}_{\mathrm{B}} - \mathbf{U}), \tag{2.35}$$

$$\mathbf{F}_{\mathrm{K}} = -\frac{\mathrm{d}\mathbf{I}}{\mathrm{d}t}; \tag{2.36}$$

see Blake *et al.* (2015) and Landau and Lifshitz (1987) for example. The equation is originally born for a sphere particle but Ohl *et al.*

(2003) confirm experimentally that Equation 2.36 still holds true even with bubble expanding or shrinking. The force becomes

$$\begin{aligned}\mathbf{F}_{\mathrm{K}} &= -\frac{\mathrm{d}\mathbf{I}}{\mathrm{d}t} \\ &= \underline{-C_{\mathrm{AM}}\rho V_{\mathrm{B}}\left(\frac{\mathrm{d}\mathbf{U}_{\mathrm{B}}}{\mathrm{d}t} - \frac{\mathrm{D}\mathbf{U}}{\mathrm{D}t}\right)} - C_{\mathrm{AM}}\rho 4\pi R^2\dot{R}(\mathbf{U}_{\mathrm{B}} - \mathbf{U}).\end{aligned} \tag{2.37}$$

The whole underlined term of the right-hand side is the added mass force, i.e., the added mass force is part of Kelvin impulse force. Conventionally, the added mass term is, however, isolated and the final form of Kelvin impulse force degenerates to only bubble volume changing term:

$$\mathbf{F}_{\mathrm{K}} = -C_{\mathrm{AM}}\rho 4\pi R^2\dot{R}(\mathbf{U}_{\mathrm{B}} - \mathbf{U}). \tag{2.38}$$

An appropriated derivation could be found in Appendix B.

HISTORY FORCE The history force comes from the delayed buildup of the surrounding boundary layer and the related wake since the aforementioned drag force is calculated in a quasi-static fashion, i.e., assuming steady uniform inflow at any moment and location. As a result, the history force should take the unsteady part left out by the steady drag force. It accounts for drag force from all the time before but with a decaying correlation with the passing time. As stated by Beelen (2018), the history force is normally implemented according to Mei and Adrian (1992) and Mei *et al.* (1991) for simplicity but without overestimation. Readers are referred to van Eijkeren (2016) for the deeper knowledge.

However, a drawback of the current Basset formulation is that the drag compartment is based on the Stokes drag instead of the forms similar to drag for higher bubble Reynolds number, Re_{B}. Talaei and Garrett (2020) changes the form based on high Re_{B} and also includes the effect of quadratic velocity dependency rather than the linear velocity relationship as suggested in the Stokes drag. In a free falling scenario, after their changes to the formulation, the revised history force is no longer negligible, which accounts for 15-25% force contribution for $\mathrm{Re}_{\mathrm{B}} = 0.2$-1100, while the simultaneous

calculation from the Basset form contributes to only 1% at the same scenario. Takemura and Magnaudet (2004) also points out that the radius change should be taken into account since the radius change will also affect the boundary layer buildup. After investigating the solid particle interaction with the solid rotation vortex, Candelier *et al.* (2004) even concludes that the trajectory is more sensitive to history force and wall effect than the lift force, and that added mass formulation correction argued by Auton *et al.* (1988) might even be less influential than the history forces.

All in all, as Talaei and Garrett (2020) points out, if Navier-Stokes equations are not analytically solved, all the particle motion equations are just some low-order approximations from the perturbation of the original equation, especially for history force term. However, this is clearly out of the scope of this study. This study will neglect the history force as many researchers suggested, and leave it as future work.

FINITE-SIZE CORRECTION Faxén force is a higher-order correction to each force component if the bubble scale is larger than the most miniature flow scale. However, Ruth *et al.* (2021) points out that the correction could be omitted if the attention is other than the acceleration spectrum.

TURBULENCE CORRECTION Very little literature has been dedicated to turbulence's influence on the bubble velocity, especially regarding the tip vertex inception. The flow physics solved by either RANS or LES has already been filtered or averaged, while most researchers directly plug the filtered physical quantities into the bubble motion equation.

The Reynolds number by Nanda *et al.* (2022)'s experiment is 7.07×10^5, so Taylor's and Kolmogorov's scales are roughly 470 (μm) and 5.15 (μm), where quite a few nuclei/bubbles are within the size: for example, see bubble size of Hsiao *et al.* (2006). Hsiao *et al.* (2006) also reports an increasing bubble dynamics trend when the artificial turbulence field is added back to the RANS solution.

Olsen *et al.* (2017) proposes to utilize a random walk model, originated from Gosman and loannides (1983), to estimate the fluctuation velocity. Z. Zhang *et al.* (2019) investigates microbubble's motion with turbulence probability density function. Vallier (2010), to the author's knowledge, is the first one who brings the turbulence correction with a random walk model into the tip vortex cavitation simulation. The turbulence dispersion contributes to different bubble distribution/-clustering along the wall-normal direction. However, the turbulence correction also relates to the size ratio between bubbles and eddies, which needs a separate function to model, but it is not thoroughly considered in the random walk model. Also, the random walk model will induce some nonphysical oscillations. As a result, the necessity of a more clever turbulence correction is left to future researchers.

FINAL FORM OF THE BUBBLE MOTION EQUATION As mentioned before, only the added mass, pressure gradient, hydrostatic, drag, lift and Kelvin impulse forces are considered. The final version of the bubble motion equation is

$$m_{\mathrm{B}}\frac{\mathrm{d}\mathbf{U}_{\mathrm{B}}}{\mathrm{d}t} = \mathbf{F}_{\mathrm{A}} + \mathbf{F}_{\mathrm{P}} + \mathbf{F}_{\mathrm{S}} + \mathbf{F}_{\mathrm{D}} + \mathbf{F}_{\mathrm{L}} + \mathbf{F}_{\mathrm{K}}. \tag{2.39}$$

Wherein,

$$\begin{aligned}
\mathbf{F}_{\mathrm{A}} &= -C_{\mathrm{AM}}\rho V_{\mathrm{B}}\frac{\mathrm{d}\mathbf{U}_{\mathrm{B}}}{\mathrm{d}t},\\
\mathbf{F}_{\mathrm{P}} &= (1+C_{\mathrm{AM}})\rho V_{\mathrm{B}}\frac{\mathrm{D}\mathbf{U}}{\mathrm{D}t},\\
\mathbf{F}_{\mathrm{S}} &= (\rho_{\mathrm{B}}-\rho)V_{\mathrm{B}}\mathbf{g},\\
\mathbf{F}_{\mathrm{D}} &= C_D\frac{1}{2}\rho\pi R^2(\mathbf{U}-\mathbf{U}_{\mathrm{B}})|\mathbf{U}-\mathbf{U}_{\mathrm{B}}|,\\
\mathbf{F}_{\mathrm{L}} &= \frac{3}{8}C_L\rho V_{\mathrm{B}}\frac{(\mathbf{U}-\mathbf{U}_{\mathrm{B}})\times\boldsymbol{\omega}}{\alpha},\\
\mathbf{F}_{\mathrm{K}} &= -C_{\mathrm{AM}}\rho 4\pi R^2\dot{R}(\mathbf{U}_{\mathrm{B}}-\mathbf{U}).
\end{aligned}$$

The added mass constant, C_{AM}, is chosen to be $1/2$ since only the spherical bubbles are considered.

The drag coefficient is expressed as a correction of the Stokes drag solution (Schiller & Neumann, 1933):

$$C_D = \begin{cases} \dfrac{24}{\mathrm{Re_B}}\left(1 + 0.15\,\mathrm{Re_B}^{0.687}\right) & \text{if} \quad \mathrm{Re_B} < 955, \\ 0.445 & \text{if} \quad \mathrm{Re_B} \geq 955. \end{cases} \tag{2.40}$$

The bubble Reynolds number is defined with its radius:

$$\mathrm{Re_B} = \frac{2|\mathbf{U} - \mathbf{U_B}|R}{\nu_l}. \tag{2.41}$$

α in lift force represents the normalized shear rate, $|\boldsymbol{\omega}|R/|\mathbf{U} - \mathbf{U_B}|$. Mainly, the Auton's formulation will be applied for the regime of the bubbles. Auton (1987) and Auton *et al.* (1988) from some analytical calculation propose

$$C_L = \frac{4}{3}\alpha, \tag{2.42}$$

under the conditions of the potential flow and the low shear rate.

For the analytical modeling, the simplified form of the bubble motion equation comes from a set of assumptions – (1) carrier phase density is far larger than the disperse one, and consequently, (2) bubble mass is much smaller than the added mass:

$$\frac{\mathrm{d}\mathbf{U_B}}{\mathrm{d}t} = 3\frac{\mathrm{D}\mathbf{U}}{\mathrm{D}t} - 2\mathbf{g} + \frac{3}{4}\frac{C_D}{R}|\mathbf{U} - \mathbf{U_B}|(\mathbf{U} - \mathbf{U_B}) + (\mathbf{U} - \mathbf{U_B}) \times \boldsymbol{\omega} + \frac{3}{R}(\mathbf{U} - \mathbf{U_B})\dot{R}. \tag{2.43}$$

In sequence, the terms on the right-hand side are pressure gradient and added mass, gravitational, drag, lift and Kelvin impulse terms. Another simpler form under the conditions of negligible gravity, applying the Stokes drag formulation, and insignificant bubble size change reads

$$\frac{\mathrm{d}\mathbf{U_B}}{\mathrm{d}t} = 3\frac{\mathrm{D}\mathbf{U}}{\mathrm{D}t} + \frac{9\nu_l}{R^2}(\mathbf{U} - \mathbf{U_B}) + (\mathbf{U} - \mathbf{U_B}) \times \boldsymbol{\omega}. \tag{2.44}$$

Both simplified forms are not implemented but present to elude the discussion.

2.3.2 *Bubble dynamics equation*

The bubble dynamics equation describes the bubble expansion and contraction behaviors. It is first introduced by Lord Rayleigh, O.M., F.R.S. (1917) and Plesset (1949) under the assumption of incompressible surrounding, namely carrier, fluid. Later, Keller and Miksis (1980) proposes another form considering the compressibility and is ultimately proven the most accurate one in the first-order theory by Prosperetti and Lezzi (1986).

The final form of the bubble dynamics equation is a combination of the Keller and Hsiao *et al.* (2000) formulations:

$$\left(1-\frac{\dot{R}}{c}\right)R\ddot{R}+\frac{3}{2}\left(1-\frac{\dot{R}}{3c}\right)\dot{R}=\frac{\left|\mathbf{U}-\mathbf{U}_{\mathrm{B}}\right|^{2}}{4} + \frac{1}{\rho}\left(1+\frac{\dot{R}}{c}\right)\left(P_{\mathrm{v}}+P_{\mathrm{g}}-P\right)+\frac{1}{\rho}\frac{R}{c}\frac{\mathrm{d}P_{\mathrm{g}}}{\mathrm{d}t}-4\nu_{1}\frac{\dot{R}}{R}-\frac{1}{\rho}\frac{2\eta}{R}, \quad (2.45)$$

η represents surface tension at the air-water interface. The gas pressure P_{g} is modeled via the ideal gas law with the polytropic process

$$P_{\mathrm{g}}(t)=P_{\mathrm{g}}(0)\left(\frac{R(0)}{R(t)}\right)^{3n}, \quad (2.46)$$

and n indicates the polytropic constant, which is the unity in isothermal condition and 1.4 for adiabatic condition. Brennen (2005) recommend regarding all dynamics with $\dot{R}>0$ as the isothermal condition but one with $\dot{R}<0$ as the adiabatic condition but the abrupt change results in the instability of the numerical integration, so the recommendation is abandoned. A constant of 1.4 is applied.

2.3.3 *Trick on the interpolation of variables*

The idea comes from one of the supervisors, Dr. Lidtke. Directly interpolating the flow variables from the unstructured grid for the bubble tracking is arduous, while the structured grid could significantly enhance the efficiency. As a result, the flow field variables are

Table 2.1: Overview of the equations.

Eulerian Simulation	Lagrangian Tracking
RANS Equations 2.7 and 2.9	Bubble Motion Equation 2.39
RSM Equations 2.11 and 2.22	Bubble Dynamics Equation 2.45
γ-$\tilde{\mathrm{Re}}_{\theta t}$ LCTM Equations 2.26 and 2.29	

first interpolated onto an agent structured grid. Then the Lagrangian part can easily access the flow field from the structured grid. The time-consuming interpolation from the original simulation is only carried out once, while the efficient interpolation from the agent structured grid is repeated several times. Consequently, a tremendous efficiency increase is gained. However, this method also suffers from numerical error, which will be discussed later. Note that if the carrier flow is formulated theoretically or without discretization such as the Lamb-Oseen vortex, then this interpolation is superfluous.

2.4 SOLUTION PROCEDURE

The procedure is separated into three parts: the Eulerian simulation, the Lagrangian tracking, and the post-processing. The Eulerian simulation gathers flow variables from the tip vortex flow field or the ideal vortex formulations. RANS, RSM, and γ-$\tilde{\mathrm{Re}}_{\theta t}$ models are applied to simulate the tip vortex flow, while the ideal vortex flow includes Lamb-Oseen vortex, for example. An in-house Lagrangian tracking code is fed with the interpolated flow field variables and simulates the bubble behavior with the modified bubble motion and dynamics equations. Finally, the outputs from the two aforementioned parts are post-processed to generate the targeted results, such as the capture time and the bubble population evolution. The related formulas are

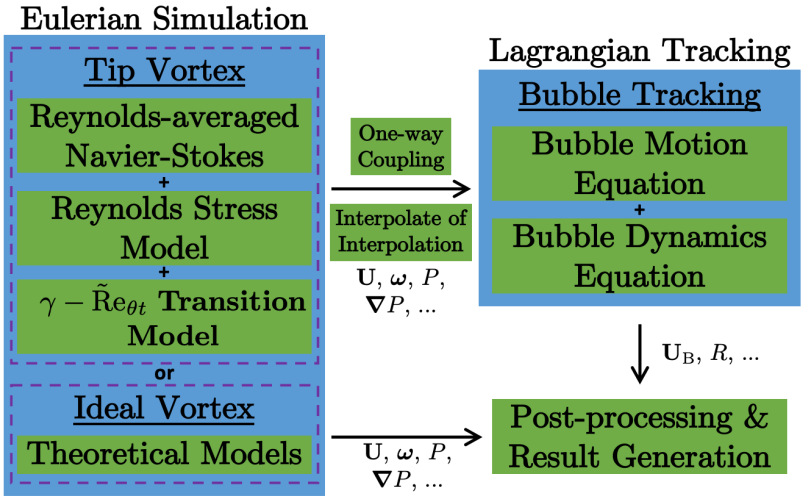

Figure 2.2: The solution framework.

organized in Table 2.1, while the flow chart for the whole procedure is shown in Figure 2.2.

This page intentionally left blank

3

VERIFICATION AND VALIDATION

A successful physics model is based on (two or) three pillars, namely the experiment, analytical, and/or numerical parts. The model is solved by analytical or numerical methods, and the results are compared to the experimental counterparts to guarantee the validity. This chapter confirms the implementations and settings in Lagrangian and Eulerian parts to be satisfactory by the verification and validation. The verification is mainly carried out by the code-wise comparison or the numerical error estimation, while the validation is performed against the available data from the literature.

An overview of the error sources will be given first with emphasizing the numerical ones. Then, the Lagrangian part will be examined. To begin with, the bubble dynamics implementation is validated against Ohl *et al.* (1999) for a bubble under the sound waves. After that, the bubble motion part is verified with the bubble settling points in the Lamb-Oseen vortex as suggested by Finn *et al.* (2011). Next, the results from Johnson Jr. and Hsieh (1966) are applied to verify the coupling part in the implementation. Note that the bubble motion and the coupling part are not validated since the rigorous experimental data dedicated to those topics are not available. Finally, the Eulerian part, i.e., the background flow field, is analyzed and validated against the available data from Pennings (2016).

3.1 OVERVIEW OF THE SIMULATION ERROR SOURCES

The physics model comes with some errors (or uncertainties), especially when the numerical simulation is carried out. The errors mainly cover the model, input, parameter, and numerical errors.

3.1.1 *Model error*

A set of mathematical models, mainly in the form of equations, are established to simulate the reality. In this case, the mathematical models are the bubble motion, bubble dynamics, RANS, RSM, and the transition equations with the corresponding assumptions. The so-called model errors come from the underlying assumptions. For example, the turbulence closure simplifies the under-resolved flow field and thus yields errors. Another example is the unresolved contribution from the bubbles to the carrier flow and the other bubbles. However, the model errors are unavoidable because the real world has to be simplified such that humans (or computers) can handle it.

3.1.2 *Input and parameter uncertainties*

The inputs toward the model also contribute to part of the errors, which is usually called input or parameter uncertainties. These inputs are usually demonstrated as the initial and boundary conditions. For instance, the inflow turbulence intensity and eddy viscosity in the simulation sometimes do not reflect the reality. The input and parameter uncertainties are sometimes due to the lack of measurement of the quantities.

3.1.3 *Numerical errors*

Intuitively, analytical tools should be applied to solve the model equations, but the inherent complexity suggests that the numerical solution is more reasonable. Numerical simulation yields several categories of errors: the iterative, machine, statistical, and discretization errors.

ITERATIVE AND MACHINE ERRORS Due to the nonlinearity of the models, iterative solvers such as the conjugated gradient method are applied to approximate the roots of the system. The deviations exist between the solved and true solutions, given a finite amount of iterations. Even if the iterative errors are ruled out, the machine error (precision) will hinder the solution from the actual roots. However, machine precision is seldom reached because of the physics complexity.

DISCRETIZATION ERRORS There are infinite degrees of freedom in spatial and temporal directions, but the computational capacity can never fully resolve the amount, which yields the so-called discretization errors. In the current research, the carrier simulation only needs to take care of the spatial errors since it is a steady-state simulation. The spatial discretization error can be assessed by the Richardson's extrapolation (Richardson & Glazebrook, 1911) or the least-square root methods (Eça & Hoekstra, 2014; Xing & Stern, 2015). However, the required computational effort is higher than the available capacity, so readers are referred to Liebrand (2019) on the related topics. On the other hand, the bubble simulation has to deal with the temporal integration errors, which, however, are easily addressed by the adaptive Runge-Kutta methods with a prescribed error tolerance.

STATISTICAL ERRORS The last numerical error is the statistical error caused by the unsteady flow oscillations.

For example, the von Karman vortex street behind the foil will yield an oscillating lift value, while the targeted values, the mean, and the associated uncertainty have to be addressed by advanced methods such as Brouwer *et al.* (2015). However, the Eulerian part of this study is free from this error due to the steady state simulation.

3.1.4 *Final remarks*

It is noteworthy that although the errors are categorized for simplicity, some are tangled with each other. Via the Sobol uncertainty index analysis, Katsuno *et al.* (2021) point out that the interaction between the parameter and the discretization errors contribute to a certain degree.

After recognizing or quantifying the errors, the simulated results are compared against the experimental ones, called the validation. If the deviations are sufficiently small, the case will be called a successful validation.

In the following sections, part of the verification and validation processes are applied to check the accuracy of the related simulations and implementations.

3.2 AN OSCILLATING BUBBLE UNDER SOUND WAVES

As designed in Ohl *et al.* (1999), a bubble is initially placed at the center of the flow field, and the sinusoidal sound waves are imposed to trigger the bubble dynamics. The ambient pressure is 100 (kPa), while the sound pressure oscillating around with the amplitude of 132 (kPa) and the frequency of 21.4 (kHz). The bubble is created with the size of 8 (μm) and the density of 1.225 (kg/m^3). Also, the bubble is assumed to deform in an adiabatic process ($n = 1.33$). The other flow parameters are $\eta = 0.07$ (N/m), $\rho = 1000$ (kg/m^3), $\mu = 0.006$ (Pa s), $P_\mathrm{v} = 2.5$ (kPa), and $\rho_\mathrm{v} = 0.024$ (kg/m^3).

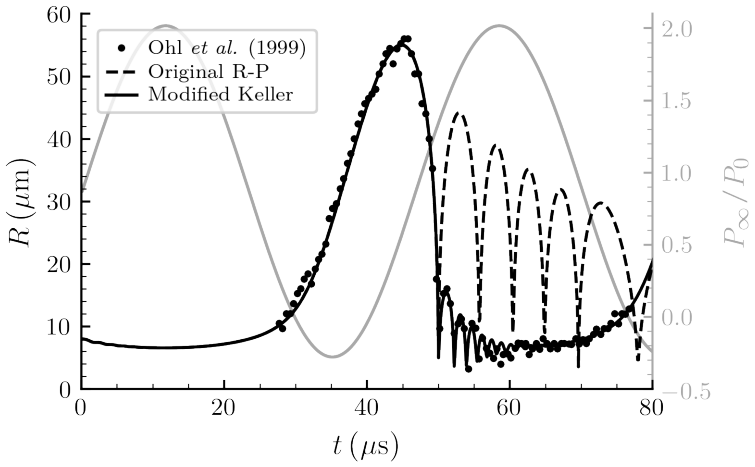

Figure 3.1: Bubble oscillating under the sound waves with different bubble dynamics equations.

Since the imposed wave frequency is less than the (linear) natural frequency of the bubble, some extreme behaviors such as the fierce bubble collapses are present to test the code capacity. As shown in Figure 3.1, the bubble dynamics implementation is sufficiently validated. It is also found that if the Rayleigh–Plesset equation is directly applied, the damping is inadequate, and the oscillating period becomes too long also.

3.3 SETTLING POINTS OF AN IDEAL VORTEX

This verification exercise is inspired by Finn *et al.* (2011) who investigate the balanced locations of a bubble in an ideal vortex flow. Sridhar and Katz (1995) also applies this method to determine the bubble lift and drag formulations in a solid-body vortex. Since the exercise applies the (modified) Lamb-Oseen vortex model, the section will be divided into two parts. The first part introduces the necessary information about the vortex and the second part elaborates on the exercise result.

3.3.1 *Modified Lamb-Oseen vortex model*

The modified Lamb-Oseen vortex, developed by Bosschers (2018), is a flow model as an analytical solution to the two-phase Navier-Stokes equations, which is described by

$$U_\theta = \frac{\Gamma_\infty}{2\pi r}\left(1 - \beta e^{-\varsigma r^2/r_v^2}\right), \tag{3.1}$$

$$\frac{\partial P}{\partial r} = \rho\frac{U_\theta^2}{r}. \tag{3.2}$$

Wherein, U_θ is the azimuthal flow velocity, Γ_∞ indicates the circulation evaluated at the infinity, and $r_v = \sqrt{4\nu_l\varsigma t}$ is introduced as the time-varying viscous radius at which the maximum azimuthal velocity occurs, while $\varsigma = 1.2564$[7] is set to fulfill the condition. β is the multiplication constant to indicate the cavitation strength:

$$\beta = \frac{r_v^2}{r_v^2 + \varsigma r_c^2} e^{\varsigma r_c^2/r_v^2}, \tag{3.3}$$

where r_c is the cavitation core radius. If it is fully wetted, β is 1, and the modified vortex degenerates to the original Lamb-Oseen vortex formulation. All of the cases planned to be investigated are flows before the cavitation inception, so β is unity throughout this study.

The flow vorticity and pressure are also provided to assist the following bubble motion and dynamics calculations:

$$\omega = \varsigma\frac{\Gamma_\infty}{\pi r_v^2}\beta e^{-\varsigma r^2/r_v^2}, \tag{3.4}$$

$$\begin{aligned} P(r) = P_\infty - \frac{\rho\Gamma_\infty^2}{(2\pi r)^2}\Bigg\{&\frac{1}{2} - \beta e^{-\varsigma r^2/r_v^2} + \frac{\beta^2}{2}e^{-2\varsigma r^2/r_v^2} \\ &+ \frac{\beta\varsigma r^2}{r_v^2}E_1\left(\frac{\varsigma r^2}{r_v^2}\right) - \frac{\beta^2\varsigma r^2}{r_v^2}E_1\left(\frac{2\varsigma r^2}{r_v^2}\right)\Bigg\}. \end{aligned} \tag{3.5}$$

Wherein, $E_1(z)$ is the exponential integral, defined as

$$E_1(z) = \int_z^\infty \frac{e^{-z}}{z}\,\mathrm{d}z\,. \tag{3.6}$$

7 Following its own definition, the expression of the constant is actually $\varsigma = \mathfrak{Re}\left(-\frac{1}{2} - W_{-1}\left(-\frac{1}{2}e^{-\frac{1}{2}}\right)\right)$, where $W_k(z)$ is the complex Lambert W function at the k^{th} branch.

The maximum azimuthal velocity is characterized in the inviscid vortex form with a deduction coefficient:

$$U_{\mathrm{v}} = \lambda \frac{\Gamma_\infty}{2\pi r_{\mathrm{v}}}, \tag{3.7}$$

where $\lambda = 0.7153$, or $1 - e^{-\varsigma} = 2\varsigma/(2\varsigma + 1)$ to be more precisely.

The radial flow profiles with different cavitation levels are recorded in Figure 3.2. The Lamb-Oseen vortex possesses similar properties to the Rankine vortex. The flow behaves like an irrotational vortex when it is far away from the vortex core, while it acts like the solid-body rotation inside the vortex core, where the viscosity effect dominates. This is also ascertained in Figure 3.3 where the angular velocity and vorticity match in the solid-body-like core. One could observe that the peak of the pressure gradient magnitude is not aligned with the maximum velocity position. Instead, it situates at a more inner position, $r/r_{\mathrm{v}} = 0.6617$ in the fully-wetted case, for instance, and the value is higher than the nominated acceleration defined at the viscous core radius. This will have some important effect when bubbles are being captured. Notice that some lines halt halfway to the vortex core because they stand for the cavitating cases, and the flow inside the cavitation core is not resolved in this model.

3.3.2 *Settling point calculation*

Typically, a vortex captures the bubbles via the pressure gradient and added mass forces, and then the bubble will eventually situate at the vortex center. However, supposed that a sufficiently large gravitation field normal to the vortex axis is applied, the final settling points will deviate from the vortex center since the hydrostatic force gives rise to another possibility of the force balance with three force directions: (1) radially-directed lift, pressure gradient, and added mass forces, (2) azimuthal-directed drag force, and (3) the upward-pointed hydrostatic force; see Figure 3.4. By the exercise, the errors in force formulations and the time integration can be identified much more quickly if there are some.

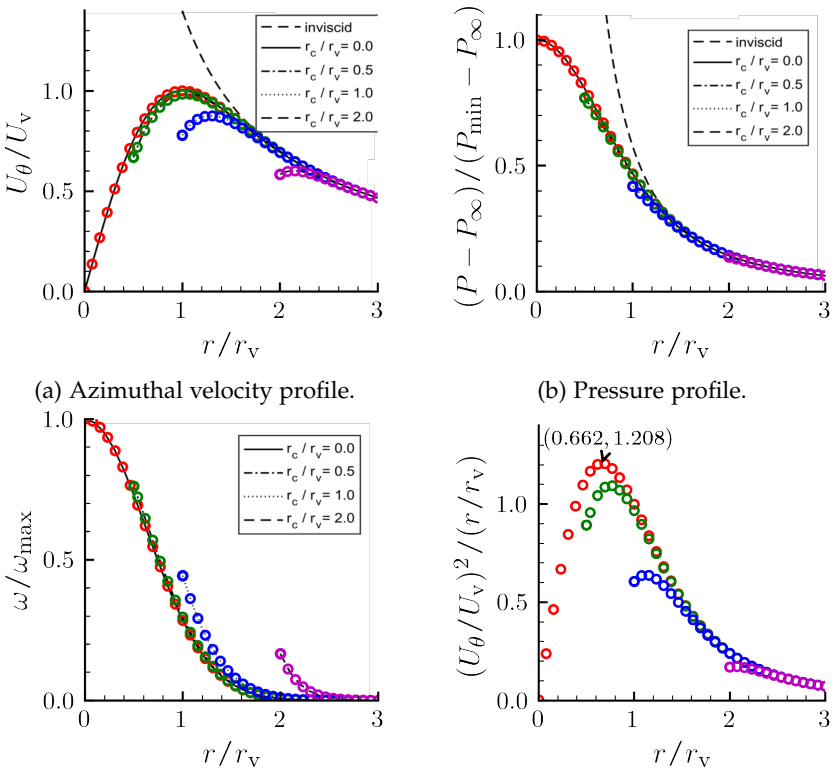

(a) Azimuthal velocity profile.

(b) Pressure profile.

(c) Vorticity profile.

(d) Pressure gradient profile.

Figure 3.2: Flow field profiles compared with Bosschers (2018). The hollow symbols represent this study's results, and the black lines in the background stand for the literature's analysis. Note that there is no verification data for the Pressure gradient profiles.

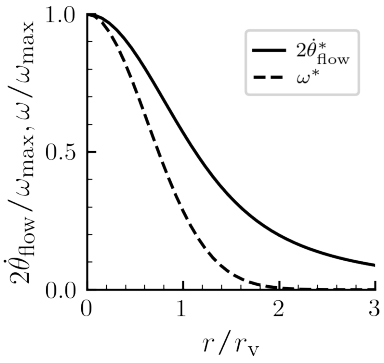

Figure 3.3: Comparison between twice the angular velocity profile and the vorticity profile of a fully-wetted flow.

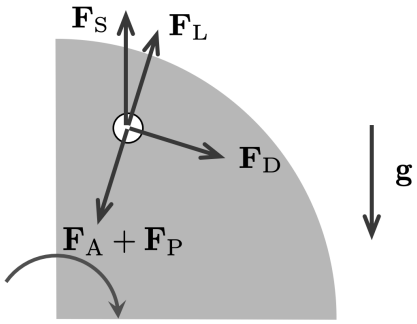

Figure 3.4: Force balance of a settling location.

There are two approaches to pinpoint the fixed points: via the root-finding method or by directly running the bubble simulations. Through comparing the two methods above, parts of the implementation are verified.

ROOT-FINDING METHOD The first method is to place static bubbles at multiple locations, and the total exerted forces are computed accordingly. The fixed points can be obtained from the root-finding algorithms like the Krylov subspace. Another root-finding technique is more involved and analytical but is still equivalent to the previous one. Given that the settling point is at (r_s, θ_s) in the polar coordinates. By decomposing the forces into the vertical and horizontal components, a set of force balances could be derived:

$$\begin{bmatrix} (F_P + F_A - F_L) & = F_S \sin(\theta_s) \\ F_D & = F_S \cos(\theta_s) \end{bmatrix}. \tag{3.8}$$

With some arrangement, the above equations become

$$\begin{aligned} \cos(\theta_s) &= \frac{3C_D U_\theta^2}{2gR\,(\rho_B/\rho - 1)}, \\ r_s &= \frac{(1 + C_{AM}) U_\theta^2}{(\rho_B/\rho - 1)\, g \sin(\theta_s) + C_L U_\theta \omega}. \end{aligned} \tag{3.9}$$

The settling points can also be found by applying some iterative methods, such as the Newton-Raphson algorithm.

DIRECT SIMULATION The other method is characterized by tracking the bubbles directly. In this case, the bubble motion equation does not account for the Kelvin impulse force, and the bubble dynamics equation is excluded in order to be more aligned with the root-finding way. Furthermore, the background Lamb-Oseen vortex is frozen in time for simplicity and partially for alignment considerations. The initial locations are set at the r_v and the null azimuthal angle direction without loss of generality.

The viscous radius is 11.45 (mm). The other parameters are $\nu_l = 1$ (mm^2/s), $\eta = 0.07$ (N/m). Totally 14 cases are introduced by varying

Table 3.1: Settling point case configurations (Finn *et al.*, 2011).

Case no.	$R(\mu m)$	$\Gamma_\infty(m^2/s)$	Case no.	$R(\mu m)$	$\Gamma_\infty(m^2/s)$
1	250	0.03	8	450	0.05
2	250	0.04	9	550	0.03
3	350	0.02	10	550	0.04
4	350	0.03	11	550	0.05
5	350	0.04	12	650	0.03
6	450	0.03	13	650	0.04
7	450	0.04	14	650	0.05

the bubble radius and the circulation strength, as listed in Table 3.1. The cases are deliberately set since there will be no distinguishable settling point other than the vortex center if the nominal drag force is far higher than the hydrostatic force.

Figure 3.5 shows both the comparisons between the methods and the literature (Finn *et al.*, 2011). In the literature, they apply the lift formulation from Sridhar and Katz (1995), different from this study's choice (Auton, 1987), so exercises based on both lift formulations are carried out and present. The results demonstrate a sufficient verification. Also, the Lamb-Oseen vortex in the literature evolves with time, so the result comparison might deviate in their own cases. From Figure 3.5, it is also observed that most of the settling locations lie at the low angle and small radius regime, clearly indicating that the azimuthal force, the drag, dominates the scenario.

3.4 BUBBLES TRAVELING OVER A RANKINE HALF-BODY

The case originates from Johnson Jr. and Hsieh (1966) who investigate the bubble migrations in the sheet cavitation scenario. The bubbles traveling around a Johnson body are investigated. Note that the body is more often called the Rankine half-body, i.e., a potential flow field

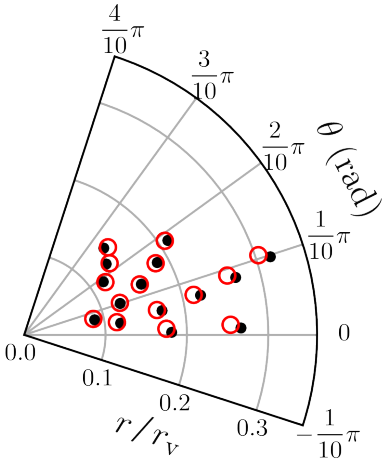

(a) Data from Finn *et al.* (2011).

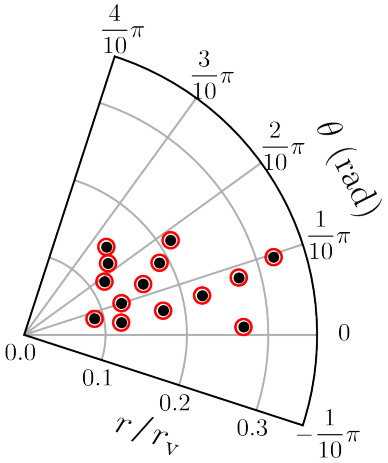

(b) Original lift coefficient.

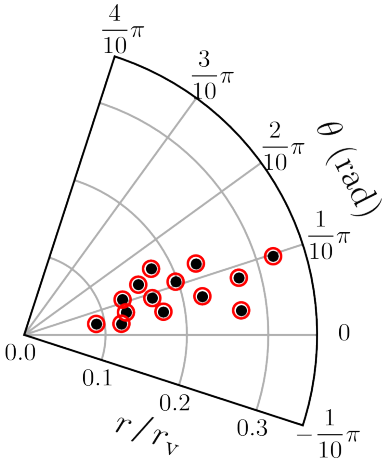

(c) Lift coefficient in this research.

Figure 3.5: Comparison of the settling points from different methods and the literature. The root-finding method is denoted with the solid black dots while the hollow red circles are the solutions predicted by the bubble motion equations.

induced by a source situated in a uniform inflow, of which the shape could be described as

$$x^* = -\frac{y^*}{\tan(\pi y^*)}. \tag{3.10}$$

The coordinates have already been normalized with the body radius, r_B, or equivalently the half-height at the infinite downstream. Note that the half-height at $x^* = \infty$ is still finite since the total flux emitted by the source is bounded.

The nondimensionalized flow field is analytically formulated as

$$U_x^* = 1 + \frac{x^*}{\pi\left(x^{*2} + y^{*2}\right)}, \tag{3.11}$$

$$U_y^* = \frac{y^*}{\pi\left(x^{*2} + y^{*2}\right)}, \tag{3.12}$$

$$C_P = \left(1 - \left(U_x^{*2} + U_y^{*2}\right)\right), \tag{3.13}$$

$$\frac{\mathrm{d}C_P}{\mathrm{d}x^*} = \frac{2\left(x^{*2} - y^{*2} + x^*/\pi\right)}{\pi\left(x^{*2} + y^{*2}\right)^2}, \tag{3.14}$$

$$\frac{\mathrm{d}C_P}{\mathrm{d}y^*} = \frac{2\left(2x^*y^* + y^*/\pi\right)}{\pi\left(x^{*2} + y^{*2}\right)^2}, \tag{3.15}$$

where the flow velocities are normalized by the unperturbed uniform inflow speed, U_∞, and the pressure by the corresponding dynamics pressure, $\frac{1}{2}\rho U_\infty^2$. The according flow field is shown in Figure 3.6 with a satisfied accurate result, $C_{P,\min} = -0.586$.

Two sets of cases are performed in the original literature, of which the common basic parameters are

$$r_B = 0.05\,(\mathrm{ft}) = 15.24\,(\mathrm{mm}), \text{ and } U_\infty = 50\,(\mathrm{ft/s}) = 15.24\,(\mathrm{m/s}).$$

The first set is by varying the initial vertical coordinates of five bubbles with the identical sizes of $R_0 = 0.02r_B$, which are all released at the far upstream, $x = -10r_B$. The second set is by altering the bubble radius but fixing the initial position at $(x, y) = (-10, 0.01)r_B$. Also, they only consider the bubble motion equation during the simulation,

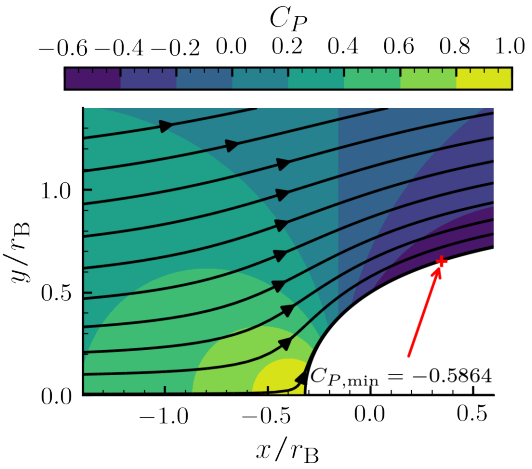

Figure 3.6: The pressure contours and the streamlines passing through a Rankine half-body.

and the bubble radii evolution is computed as a post-processing procedure with a quasi-equilibrium approach. Also, gravity is neglected in this case.

The results are shown in Figure 3.7. The paths match the original calculations adequately. To gain more insight into the bubble behaviors, the bubble motion equation is simplified to the form of Equation 2.44:

$$\frac{\mathrm{d}\mathbf{U}_\mathrm{B}}{\mathrm{d}t} = 3\frac{\mathrm{D}\mathbf{U}}{\mathrm{D}t} + \frac{9\nu_\mathrm{l}}{R^2}(\mathbf{U}-\mathbf{U}_\mathrm{B}) + (\mathbf{U}-\mathbf{U}_\mathrm{B})\times\boldsymbol{\omega}. \qquad \text{(2.44 revisited)}$$

As expected, the larger bubble is more sensitive to the pressure gradient than the drag and thus unable to reach the low-pressure zone behind the stagnation pressure field. Also, the further the initial position deviates from the body centerline, the less possible a bubble will be entrapped in the low-pressure zone. The aforementioned phenomena both represent bubble screening. Although the method Johnson Jr. and Hsieh (1966) applied is quite simple, and with some assumptions, the cases can still serve as decent verification exercises qualitatively.

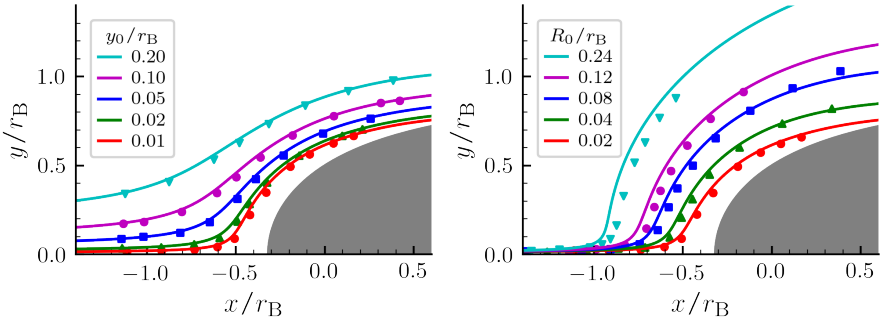

(a) Varying the initial vertical locations.

(b) Varying the bubble radii.

Figure 3.7: Comparison of bubble paths around a Rankine half-body. Solid lines represent the numerical result, while the scattered symbols stand for the results from Johnson Jr. and Hsieh (1966).

3.5 TIP VORTEX FROM THE LIFTING ELLIPTIC HYDROFOIL

The section compares the simulation results with the experimental and numerical ones in the literature. As mentioned previously, the verification study is not performed due to the computation limitation. An Arndt foil is mounted on the tunnel wall with Angle of Attack (AOA) of 9° to generate the tip vortex flow field. Apart from the direct flow field comparisons, the vortex properties such as the viscous radius and circulation evolution are also investigated.

3.5.1 *Case description*

The Arndt foil is a lofting surface of NACA66$_2$-415 airfoil sections whose chord length scales with the vertical half-elliptic contour. The geometry applied in the TU Delft cavitation tunnel has the root chord length, c_0, of 0.1256 (m) and the half-span (or height), b, of 0.15 (m).

The simulation serves as a preparation for performing the bubble motion analysis in the tip vortex, and part of the bubble motion will be compared with the experimental data from Ir. Nanda in the following chapter so that the configuration will resemble its setup. However, only Pennings (2016) provides a comprehensive

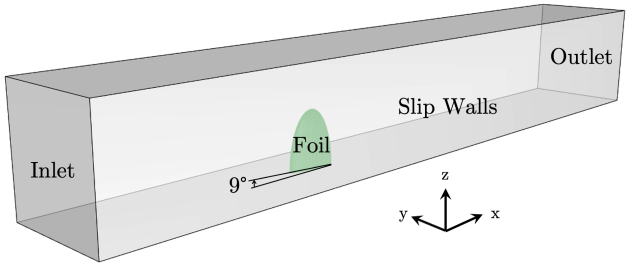

Figure 3.8: The computational domain.

flow field measurement, and also, plentiful literature has performed the case in the following-mentioned velocity (Klapwijk, 2021), so a compromise is necessary. The inflow velocity will be $7.15\,(\mathrm{m/s})$ with $\nu_1 = 1.002 \times 10^{-6}\,(\mathrm{m^2/s})$ and $\rho = 998\,(kg/m^3)$, yielding a base chord Reynolds number of 8.96×10^5, a bit lower than the Penning's one, 9.39×10^5, but it is definitely tolerable for flow field comparison

Figure 3.8 shows the configuration of the computational domain. $+x$ stands for the streamwise direction pointing from inlet to outlet, $+z$ represents the spanwise direction pointing from bottom to top, while $+y$, following the lift direction, is designated by the right-hand rule Cartesian coordinate system. The suction and pressure sides are in $+y$ and $-y$ directions, respectively.

The physical cavitation tunnel has the cross section evolving from $0.30 \times 0.30\,(\mathrm{m})$ to $0.30 \times 0.31\,(\mathrm{m})$ to compensate the momentum deficit from the boundary layers of the side walls. However, the slip-wall boundary condition is set on all of the side walls to circumvent the difficulty in the simulation so that a uniform section of $0.30 \times 0.30\,(\mathrm{m})$ is applied in CFD simulation.

Figure 3.9 shows the strategy of meshing with a roughly 20M grids. A set of manual grid refinements around the tip vortex is applied based on a coarser grid simulation result. Also, the wake region are resolved by another set of grid refinement. The viscous layers cover the blade to guarantee that the wall y^+ is of $\mathcal{O}(1)$.

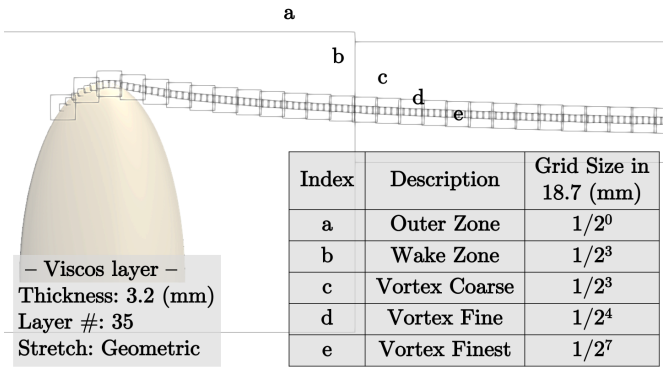

Index	Description	Grid Size in 18.7 (mm)
a	Outer Zone	$1/2^0$
b	Wake Zone	$1/2^3$
c	Vortex Coarse	$1/2^3$
d	Vortex Fine	$1/2^4$
e	Vortex Finest	$1/2^7$

Figure 3.9: Grid strategy.

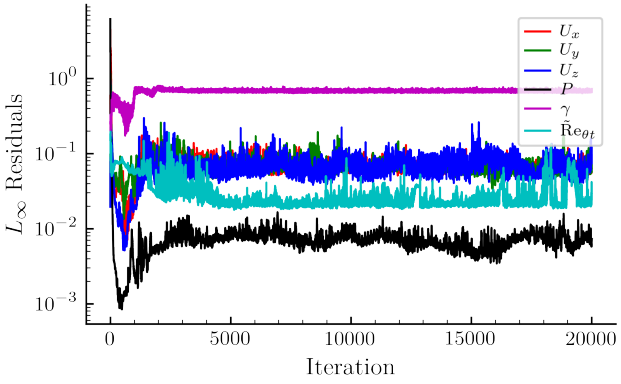

Figure 3.10: The L_∞ residual histories.

The inlet is placed $5c_0$ in front of the leading edge while the outlet is placed $10c_0$ behind the trailing edge to efficiently prevent the numerical reflection waves from the boundaries as suggested in Klapwijk (2021). The inlet is a Dirichlet boundary of the inflow velocity, and the outlet is that for the pressure. The inflow turbulence intensity and the eddy viscosity ratio are chosen to be 1.0% and 1.0, respectively.

L_∞ is essentially the maximum of the absolute residual values.

The convergence histories are shown in Figures 3.10 and 3.11. The grid quality near the blade surface impeded the convergence, especially for the transition variables, which are particularly unstable along the grids (Liebrand, 2019). However, the instabilities are locally confined between the adjacent cells, so the histories of the integral

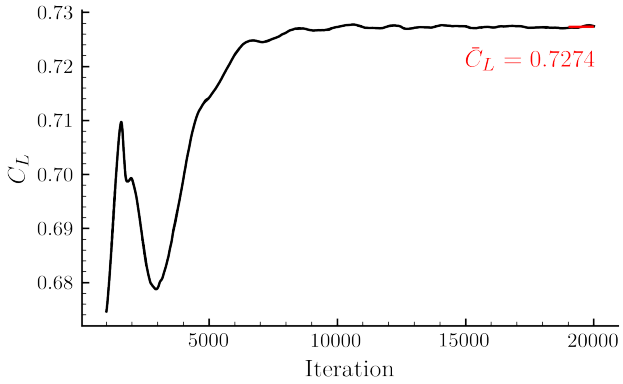

Figure 3.11: The lift histories. The mean lift coefficient is calculated via averaging the values within the red range.

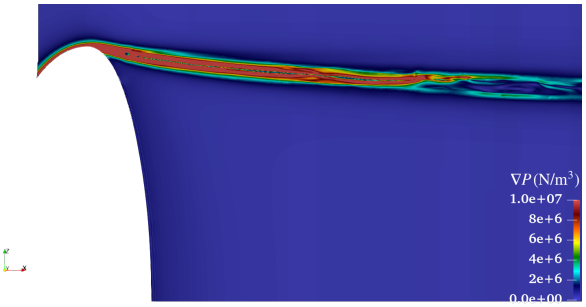

Figure 3.12: Distribution of pressure gradients through the vortex center surface.

value, such as the lift coefficient, are still a decent indicator for convergence.

The resultant foil lift coefficient is 0.7274, while the experimental one is 0.65. The overpredicted phenomenon is also observed in Klapwijk (2021), and is probably due to the turbulence modeling.

3.5.2 *Special topic on the material derivatives and the pressure gradients*

As argued in Section 2.3.1, the pressure gradient is insufficient to resolve all the present first-order forces, while the material derivative

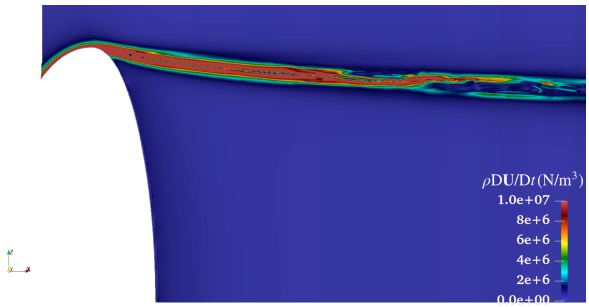

Figure 3.13: Distribution of material derivatives through the vortex center surface.

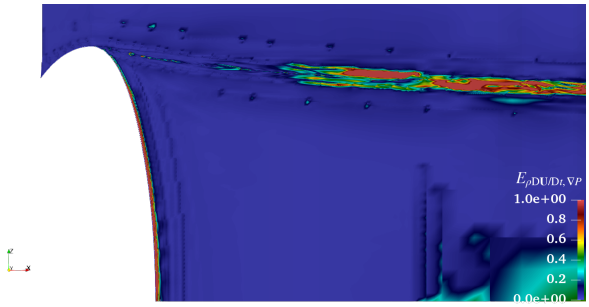

Figure 3.14: Relative difference between the pressure gradients and material derivatives.

Figure 3.15: Distribution of viscous stress gradients through the vortex center surface.

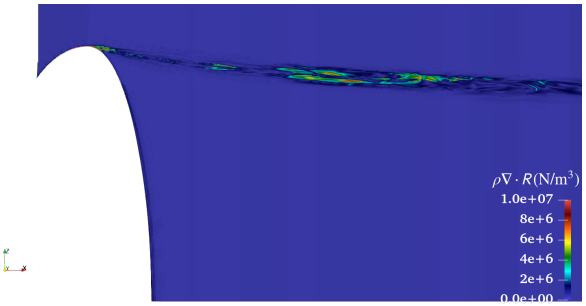

Figure 3.16: Distribution of Reynolds stress gradients through the vortex center surface.

is a more prominent one to include the pressure gradient, viscous stress gradient, and Reynolds stress gradient contributions:

$$\frac{\mathrm{D}\rho\left\langle U_i\right\rangle}{\mathrm{D}t} = -\frac{\partial\left\langle P\right\rangle}{\partial x_i} + \frac{\partial\left\langle T_{ij}\right\rangle}{\partial x_j} - \frac{\partial\rho R_{ij}}{\partial x_j}. \tag{3.16}$$

From Figures 3.12 to 3.14, it is found that there are substantial differences between the pressure gradient and the material derivatives downstream because the Reynolds stresses are pronounced there, which is indicated in Figure 3.16. Remarkably, the viscous stresses do not contribute to the difference, as in Figure 3.15.

The pressure gradient force in both forms will be examined to answer the question. However, since the rigorous comparison of the bubble motions between numerical and experimental results is nearly impossible, only the differences between the two forms are present in the following study.

3.5.3 *Direct flow field comparisons*

The targeted flow field measurements are available from Pennings (2016). The flow field is measured at several streamwise cross sections. The main idea is to check if the flow field near the vortex core is sufficiently resolved.

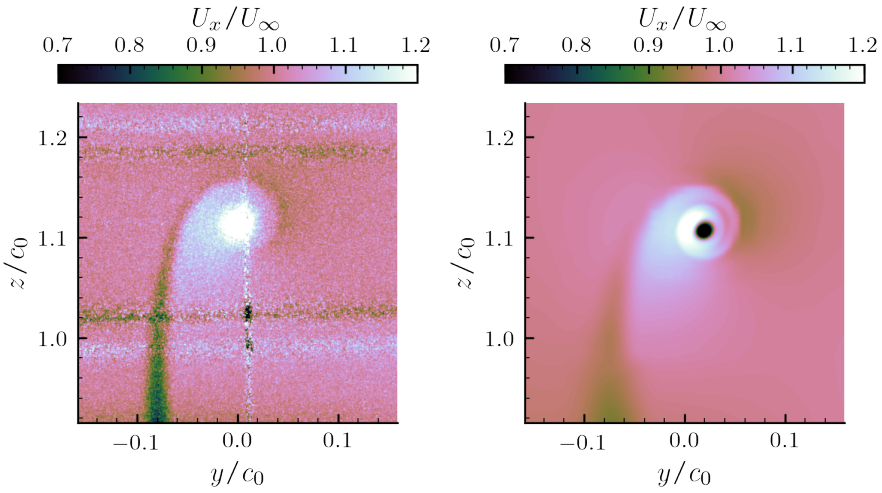

(a) Experimental measurement. (b) Numerical simulation.

Figure 3.17: Axial velocity normalized with the inflow velocity and the origin aligned with the wing root coordinates.

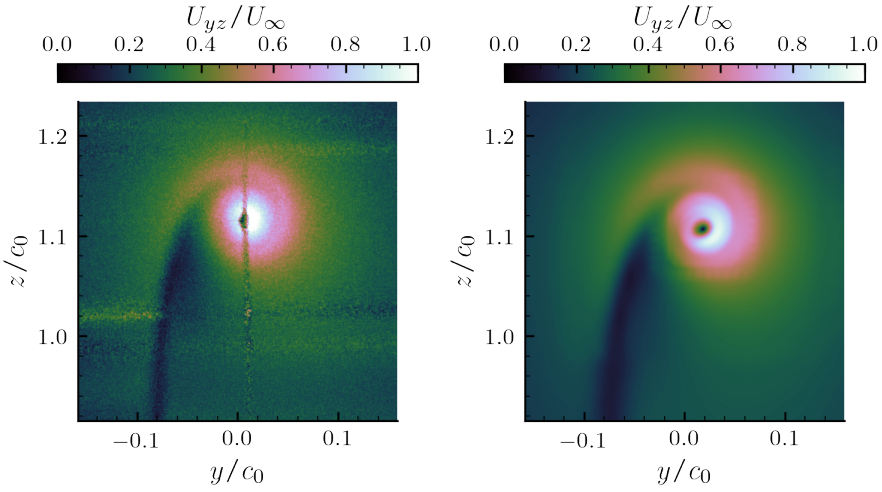

(a) Experimental measurement. (b) Numerical simulation.

Figure 3.18: In-plane velocity normalized with the inflow velocity and the center aligned with the wing tip planar coordinates.

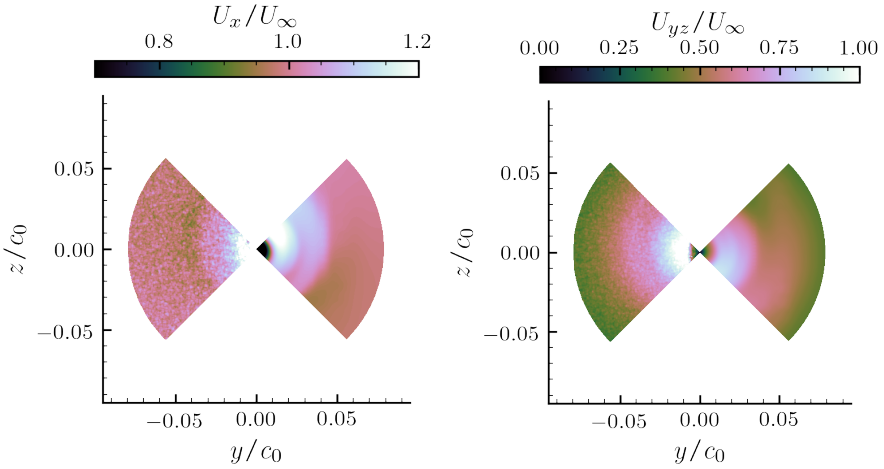

(a) Axial velocity.

(b) In-plane velocity.

Figure 3.19: Near-core velocity distribution of the foremost section ($x/c_0 = 0.5$). The left-hand side is the experimental data, and the right-hand side is the numerical result.

Among the slices, the foremost slice ($x/c_0 = 0.5$) is chosen to examine the roll-up process during the vortex formulation. The axial and in-plane velocity comparisons are separately present in Figures 3.17 and 3.18, while Figure 3.19 gives a closer comparison. The prescience of the tip cavity causes the shadows in the experimental data. Although the roll-up pattern is not clearly shown in the experiment measurement, there are distinguishable flow regimes in the numerical one. The flow regimes of a roll-up vortex, as proposed by Phillips (1981), are characterized by (I) viscous-dominated solid body rotation, (II) turbulent diffusion flow, (III) spiral merging zone, and (IV) outer (mainly inviscid) zone. Figure 3.20 visualizes the zones.

A noteworthy discrepancy is that the axial velocity shows a momentum deficit in the numerical simulation but a jet-like behavior in the experimental measurement, which is also observed in Liebrand (2019) and Xie *et al.* (2021). The phenomenon is more obvious in Figure 3.21a. Liebrand (2019) points out that the excessive diffusion in the RSM model causes the large deviation, and the DDES and IDDES share the same diffusive nature to some extent. Figure 3.22 shows that only if the LES is applied with a proper grid resolution the jet-like

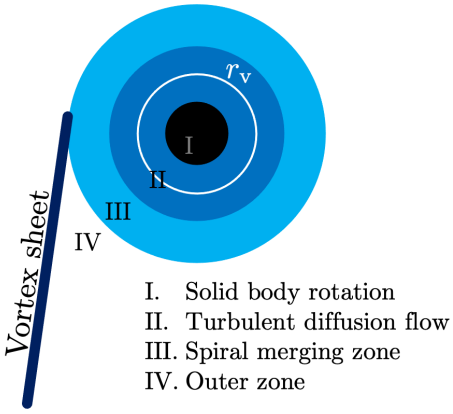

Figure 3.20: Schematic diagram of a roll-up process, modified from Phillips (1981).

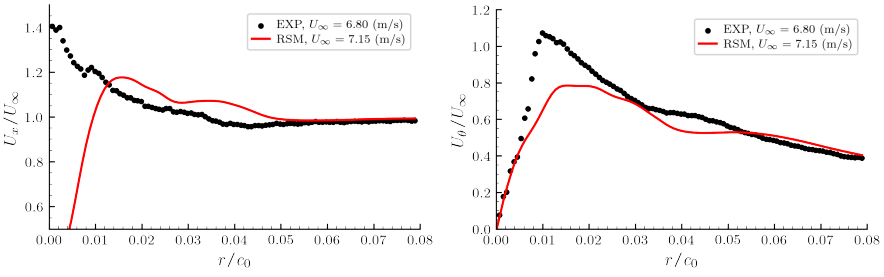

(a) Axial velocity.

(b) In-plane velocity.

Figure 3.21: Vortex velocity profiles of the section at $x/c_0 = 0.5$.

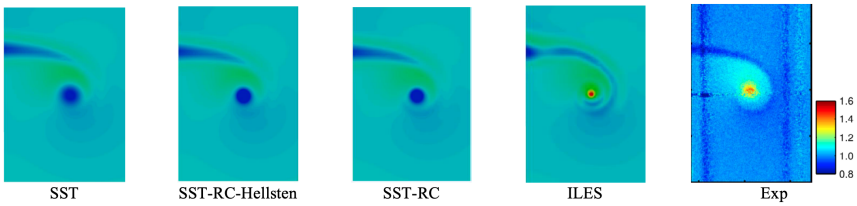

Figure 3.22: Axial velocity in vortex core by different turbulence modelling (Asnaghi *et al.*, 2017a).

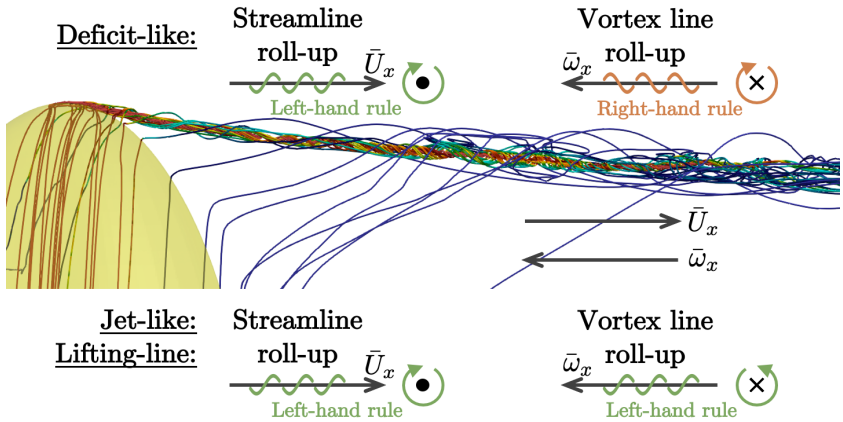

Figure 3.23: Vortex line roll-up from the numerical simulation.

nature can be sufficiently captured (Asnaghi *et al.*, 2017a). Asnaghi *et al.* (2017a), Asnaghi *et al.* (2020) also mention that the prediction of the boundary layer on the blade and the suction zone near the tip vortex initiation location all contribute to the axial velocity discrepancy in RANS simulation. Nevertheless, the jet-like or velocity deficit behaviors are all possible in a real tip vortex, and are highly determined at least by the tip geometry, aspect ratio, and the generated lift (Anderson & Lawton, 2003).

Unlike the axial velocity, the azimuthal velocity is not over-sensitive to the diffusion from the turbulence models or grid resolution. Generally, the numerical simulation has successfully captured the velocity trend, but it is still far from accurate from the quantitative point of view.

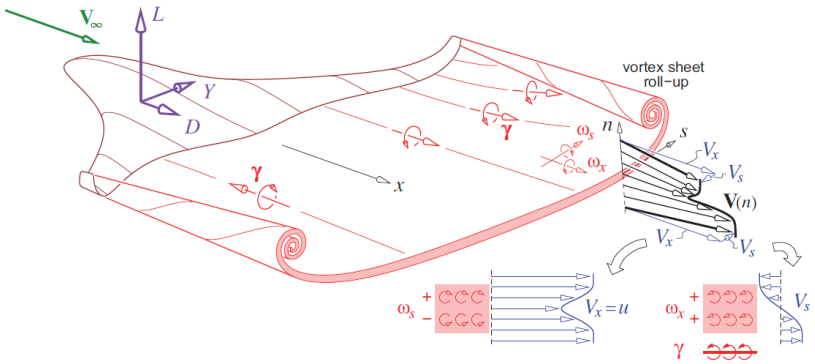

Figure 3.24: Vortex sheet (filaments) roll-up from the lifting-line theory (Drela, 2014). The current elliptic foil is analog to the left part of the present aircraft.

The rolling up process itself yields a critical difference from a 2D vortex model: the vorticity vectors are somewhat tilted in the azimuthal direction of the streamwise plane instead of perpendicular to the plane, as shown in the vortex lines[8] of Figure 3.23. As a result, attention should be paid to the connection between the 2D vortex model and the CFD results. Another thing worth noticing is the roll-up direction of the vortex lines. Intuitively, it is expected that the vortex line roll-up direction (right- or left-hand thumb rule)[9] should be similar to the description of the traditional lifting-line theory: the roll-up direction is identical to that of streamlines; see Figure 3.24. However, in the present numerical simulation, the vortex lines inside the tip vortex core rotate contrary to the expectation, as shown in the dense vortex lines near the core, also in sketches of the deficit-like part in Figure 3.23.

8 A vortex or vorticity line, analog to the streamline, is a line tangent to the local vorticity field everywhere. Although the vortex line and the streamline are similar to each other conceptually, one should note that the describing objects – vorticity and velocity fields – are still different. Also, the vortex line is different from the vortex center line. The former one visualizes the behavior of the vorticity field, while the latter one describes where the vortex center is on each coordinate plane.

9 The direction of the vortex line roll-up direction and the direction of the induced velocity by the vortex line are two different concepts. The swirling of the induced velocity is controlled by the Biot-Savart law, which is always of the right-hand thumb

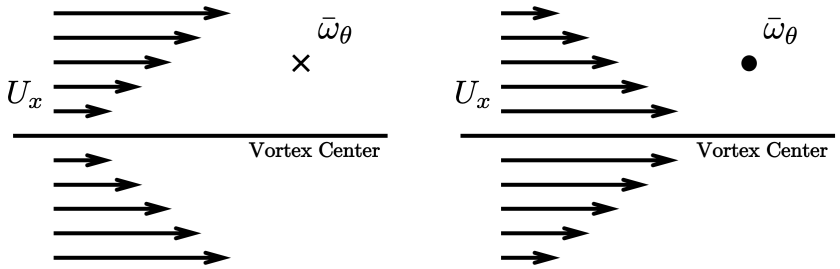

(a) Deficit-like axial velocity.

(b) Jet-like axial velocity.

Figure 3.25: The relationship between the axial velocity profile and the azimuthal vorticity direction.

The roll-up direction of the vorticity line reflects the azimuthal component of the vorticity. Especially, the axial velocity profile contributes the most to that vorticity component, which Figure 3.25 clearly shows. A jet-like or a deficit-like velocity profiles yields two different directions of velocity shear and thus the direction of the azimuthal vorticity component. As shown previously, the axial velocity profiles are predicted differently among CFD and experiment (or the lifting-line theory). As a result, the rolling-up direction predicted by the current CFD is different from the normal one.

3.5.4 *Properties of the derived quantities*

The viscous radius and the circulation characterize the evolution of the tip vortex flow field. The vortex center is selected to be the minimum point in the pressure field, and the viscous radius is calculated from the distance between the position of the maximum angular-averaged azimuthal velocity and the vortex center. On the other hand, the circulation is obtained by integrating the vorticity on a streamwise section plane. Apart from the aforementioned variables,

rule. However, the rolling up of the vortex line highly depends on the surrounding flow field, where the right- or left-hand thumb rules are both possible.

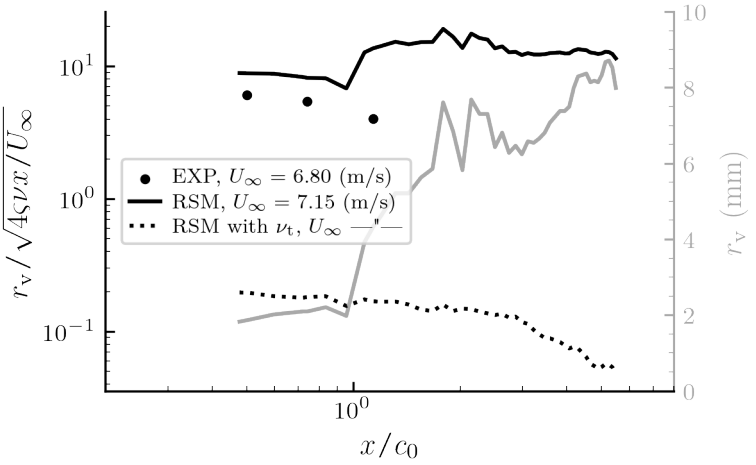

Figure 3.26: Evolution of the viscous radii. Dashed lines represent results considering the eddy viscosity.

an interesting behavior of the tip vortex asymptotic location is also analyzed

The viscous radius evolution is shown in Figure 3.26. The dimensional viscous radii from the numerical simulation vary quite a bit, roughly growing from 2.0 to 8.0 (mm) from the near to far downstream. For simplicity, a nominal value of 5.0 (mm) will be considered the mean viscous radius in the main study without loss of generality. The viscous radii are also normalized, assuming that the vortex behaves like a 3D advection-dominant Lamb-Oseen vortex:

$$r_v \propto \sqrt{\frac{4\varsigma\nu x}{U_\infty}}, \quad \text{and} \quad \nu = \nu_l. \tag{3.17}$$

The numerical simulation clearly overestimates the viscous radius in comparison to the measurement. The underlying reason could be that the numerical simulation is suffered from excessive diffusion and that the numerical flow field inside the core is more chaotic at certain sections, while some even have more than one core. It is also found that the magnitude proposed by the laminar Lamb-Oseen vortex is incorrect. As a result, the turbulence eddy viscosity is incorporated into the formulation, which is the dashed lines:

$$\nu = \nu_l + \nu_t, \tag{3.18}$$

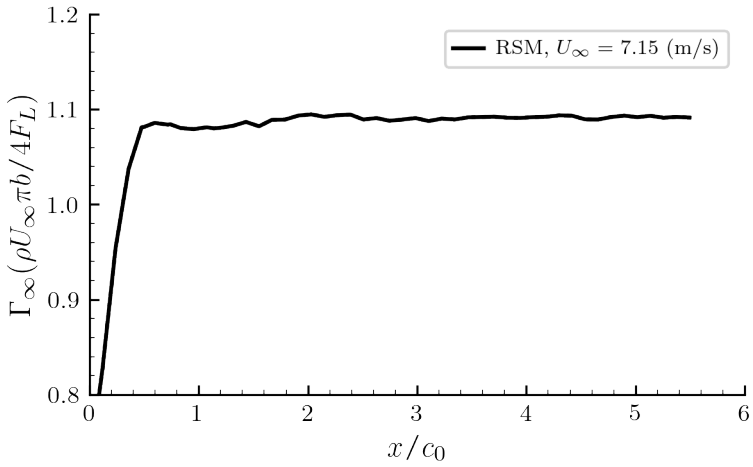

Figure 3.27: Evolution of the circulation.

where ν_t is the eddy viscosity. Although the order of magnitude can roughly be captured via the manipulation, the decaying values still indicate that the eddy viscosity, in reality, does not fully contribute to the vortex core diffusion due to the anisotropic nature in the RSM.

Circulation, on the other hand, is normalized by the Kutta-Joukowski (Zhukovsky) lift-circulation relationship, present in Figure 3.27. The normalization has also considered the elliptic shape effect, i.e., an ellipse only occupies $\pi/4$[10] of the bounding rectangular area. Since the computational domain sides are the slip walls, the circulation or, more basically, the vortex field cannot pass through the boundaries to the outer domain or be dissipated by the walls. As a result, the circulation remains constant downstream from the foil with only minor fluctuations due to the discretization errors. The deviation between the mean value and the unity could be attributed to the finite-span and viscous effects.

10 One may argue that the scale factor should be $(\pi/4)^2$ because the camber is scaled down simultaneously. However, according to the thin airfoil theory, the dipole strength density $\gamma(x)$ is proportional to the local camber slope, which is identical when the airfoil section is scaled down. As a result, the section circulations are only affected by the chord length: $\Gamma(z) = c(z)\int_0^1 \gamma(x^*)\,\mathrm{d}x^*$. Collicott *et al.* (2016) also get a similar expression in its Equation 7.29 with more rigorous approach.

The other thing worth mentioning is the asymptotic vertical location of the tip vortex. According to the lifting-line trailing vortex theory, the centroid of the vorticity should remain at the same position across x direction if no obvious outer forces are applied (Betz, 1933; Rule & Bliss, 1998):

$$\bar{\xi} = \frac{1}{\Gamma_0} \int_0^{\xi} \frac{\mathrm{d}\Gamma(\chi)}{\mathrm{d}\chi} \chi \, \mathrm{d}\chi \,, \tag{3.19}$$

in which ξ represents the spanwise coordinate, Γ_0 the maximum circulation strength of the foil, and the result is $\pi b/4$ by the lifting-line theory if the foil is elliptically loaded (or, equivalently, in elliptical shape):

$$\Gamma(\xi) = \Gamma_0 \sqrt{1 - \left(\frac{\xi}{b}\right)^2}. \tag{3.20}$$

The asymptotic location of the tip vortex matches with the calculation with a relative error of only 1%.

3.5.5 *Equally-spaced Cartesian structured grid interpolation*

As mentioned in the previous chapter, the interpolation trick comes with some errors. Therefore, the interpolation errors of important variables are necessary to identify. The extracted grid data spans only from $(-1.5c_0, -0.25b, 0.66b)$ to $(6.0c_0, 0.25b, 1.16b)$, and the number of grid points on each side is identical ($N_x = N_y = N_z$). The relative discretization errors are presented in Figure 3.28, which are sampled at several points near the vortex core at different x coordinates. Generally, the errors decrease with the expected second-order accuracy, and the most refined grid performs the best, so it is applied for the bubble tracking simulation. Although there are still some deviations, the limited computational capacity obstacles further refinement. The drawback is compensated by carrying out simulations in the small-scale grid boxes where some interesting phenomena are found locally.

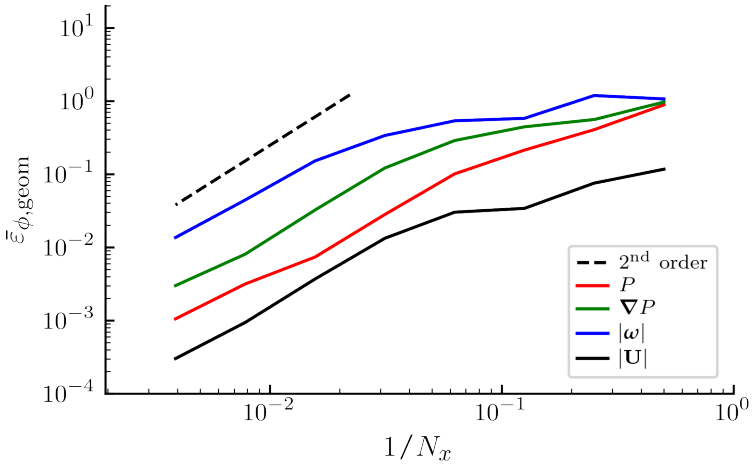

Figure 3.28: Geometrically-averaged interpolation errors of different streamwise slices.

4

BUBBLE MOTIONS IN IDEAL VORTEX MODELS

The chapter focuses on the bubble motions induced by the ideal vortical flow fields, mainly the Lamb-Oseen vortex models. The main investigation topics are the capture time, where the numerical simulation and the analytical solutions are applied to sustain the proposed statements. Also, a general overview and some results of the regime plot are given. Note that there will be no experimental result present in the chapter since this is an idealized case.

4.1 CASE DESCRIPTIONS

The set of cases is performed in a stationary fully-wetted Lamb-Oseen vortex with $\Gamma_\infty = 0.29$ (m^2/s) and $r_v = 0.1$ (m), which resembles the cases appear in several literature (Oweis *et al.*, 2005; Peters & el Moctar, 2020; L. Zhang *et al.*, 2016). The stationary flow field, indicating the viscous radius is a constant throughout the simulation, is employed to simplify the circumstance. Although the result in this study is mainly based on $\Gamma_\infty = 0.29\,(m^2/s)$, the cases of circulation strength from 0.29 to $29.0\,(m^2/s)$ have also been carried out to investigate its influence. In each circulation case, a total of seventy bubbles are seeded as a matrix of seven different bubble sizes and

ten different released radial locations, each of which is a geometric progression:

$$\begin{aligned} R_0/r_\mathrm{v} &= 0.100, 0.064, 0.041, 0.027, 0.017, 0.011, 0.007; \\ r_0/r_\mathrm{v} &= 0.316, 0.431, 0.586, 0.799, 1.088, 1.481, 2.017, \\ &\quad 2.746, 3.740, 5.093. \end{aligned}$$

Each bubble is released with a velocity identical to the flow.

The cavitation number is chosen to be identical to the one defined in Peters and el Moctar (2020), which is in a special form of viscous core velocity and the corresponding pressure:

$$\sigma_\mathrm{v} = \frac{P_\mathrm{vc} - P_\mathrm{v}}{\frac{1}{2}\rho U_\mathrm{v}^2} = 3.602, \tag{4.1}$$

where P_vc is the pressure at the viscous core edge and U_v is the azimuthal velocity at the viscous core edge. The cavitation number is fixed at each circulation strength to reach a fair comparison.

Since the material derivatives and pressure gradients are identical in the stationary Lamb-Oseen vortex, the difference between the two forms cannot be investigated in this chapter.

4.2 CAPTURE TIME ANALYSIS

To investigate the bubble population around the vortex core, the entrapment time is a directly-related parameter. The entrapment time, also called the capture time, is the elapsed time for a bubble traveling from the released points to a given radial criteria. Apart from analyzing the capture time trend, the following text addresses the observations, development and limitations of the analytical capture time models. The capture time model is inspired by Oweis *et al.* (2005), but a far more rigorous inference and the correct foundation will be present.

Without loss of generality, the capture criterion is set to be a small radial coordinate value, $r_\mathrm{cap}/r_\mathrm{v} = 0.1$, which is large enough to allow some space for the numerical errors around the center but is also small enough to preserve the capture time trend.

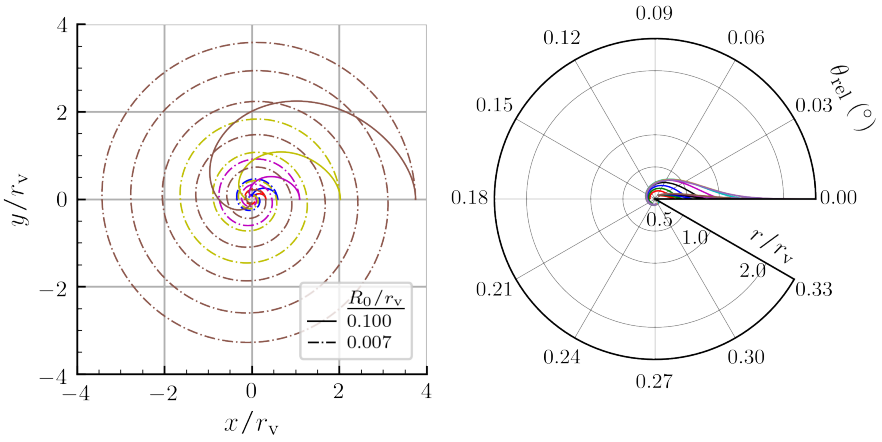

(a) Paths under the absolute frame. (b) Paths relative to the fluid carrier.

Figure 4.1: The bubble paths in different initial conditions. The different colors represent the different released locations.

4.2.1 *Observations*

This piece of text helps to build the foundation of the capture time model from the observations based on the numerical simulation. There are totally four observations that assist the analysis.

The first one is that the polar coordinate mechanics assists to describe the bubble motion in the planar vortical flow. The paths with different conditions are sketched in Figure 4.1a. As one may notice, the paths are spiral lines, which sustains the statement. Readers are referred to Appendix C for an introduction to the polar coordinate planar motion.

Another observation comes from Figure 4.1b, where $\theta_{\text{rel}} = \int \dot{\theta} - \dot{\theta}_{\text{flow}}\, \mathrm{d}t$. The former $\dot{\theta}$[11] represents the bubble motion, and the latter one is from the flow field. θ_{rel}, as a measurement of the accumulated deviation between the bubble and the flow in the azimuthal coordinate, reaches its maximum with only 0.33°, meaning that the bubble mainly follows the azimuthal flow velocity all over the traveling time.

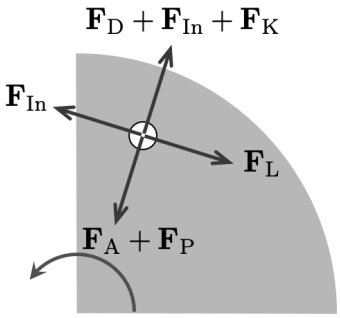

Figure 4.2: Free-body diagram of a bubble traveling with the flow.

This further confirms that the relative velocity, $\mathbf{U}_B - \mathbf{U}$, only has the components of the radial direction, i.e.,

$$\mathbf{U}_B - \mathbf{U} = \dot{r}\hat{\mathbf{e}}_r, \tag{4.2}$$

and only the radial component of the kinematics is important in the capture time analysis. Already, an image of the free-body diagram on the bubble could be depicted as Figure 4.2. Surprisingly but reasonably, the lift acts in the azimuthal direction and the drag in the radial direction, contrary to the settling point cases due to the relative velocity direction. The directions partially reveal the force's role, which will be elaborated further in the final part of the chapter.

Oweis et al. *(2005) implicitly states that the lift force acts in the radial direction.*

The third observation originates from Figure 4.3. The apparent radial acceleration could be appropriately neglected, even if the bubbles are released under different initial parameters. The plateau shape is dominant, and the accelerations seem to be mild in each case. However, applying this observation/assumption has some potential risks and will be addressed later when verifying the proposed model.

The last observation is about the bubble size changes. It is clear that the bubble radius changes are not apparent under such cavitation number. As a result, it is safe to assume that $\dot{R} \approx 0$ and $R = R_0$ anytime. The bubble dynamics and the Kelvin impulse force are thus not necessary to be accounted for in the model.

11 The suffixes of the bubble kinematic in Newton's notation have been neglected for simplicity, such as $\dot{r}$, $\ddot{\theta}$ and $\dot{x}$.

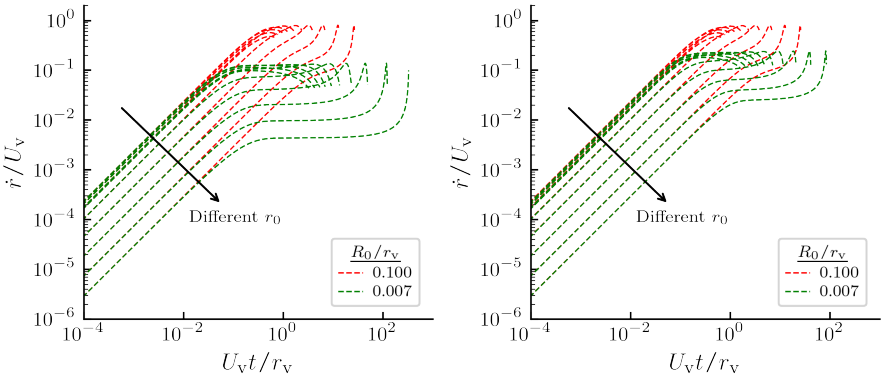

(a) $\Gamma_\infty = 0.29\,(\mathrm{m}^2/\mathrm{s})$. (b) $\Gamma_\infty = 29.0\,(\mathrm{m}^2/\mathrm{s})$.

Figure 4.3: History of normalized radial velocity with regards to different circulation strengths.

In a nutshell, the polar coordinate mechanics is applied to assist the analysis, and three other observations are applied to form the modeling:

$$\dot{\theta} - \dot{\theta}_\mathrm{flow} \approx 0, \quad \dot{R} \approx 0, \quad \ddot{r} \approx 0.$$

4.2.2 *Discussion on the velocity profile*

The velocity profile is essential to uncover the model's validity, so it is present before the model development and analysis. The dimensionless radial velocity profiles are plotted against the dimensionless simulation time (Figure 4.3) and the dimensionless radial distance to the vortex core (Figure 4.4[12]) in order to give a more thorough insight into the background mechanism.

Figure 4.5, as an extraction of Figure 4.3, presents that a bubble generally experiences three stages:

- Initial acceleration stage (the inclined straight lines):

12 Please focus on the simulation lines now. The lines named with "Schiller+LO" will be introduced later.

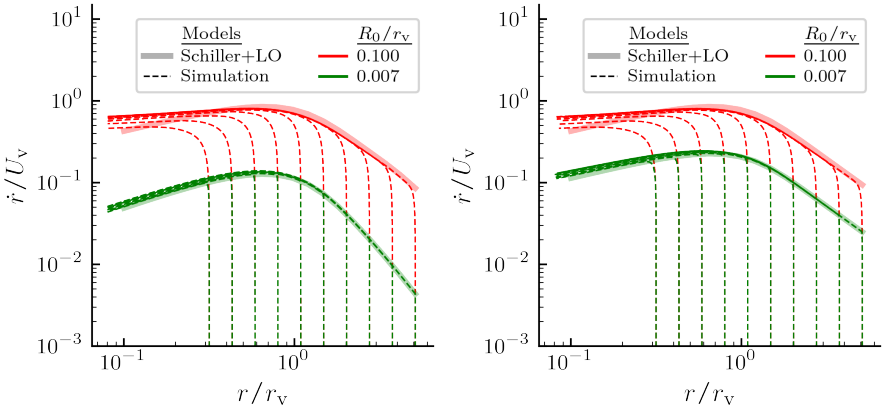

(a) $\Gamma_\infty = 0.29\,(m^2/s)$. (b) $\Gamma_\infty = 29.0\,(m^2/s)$.

Figure 4.4: Radial history of normalized radial velocity with regards to different circulation strengths.

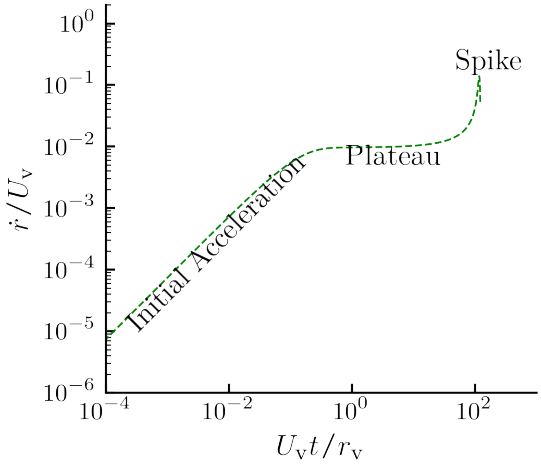

Figure 4.5: Different stages of the radial velocity.

The bubble accelerates because the initial radial velocity is not prescribed in the numerical simulation. The stage is dominated by the pressure gradient force and terminates when the drag force becomes comparable, or namely, the bubble reaches a (quasi-) balance stage in the radial direction.

The velocity profiles of the stage are also similar between different bubble sizes, shown as the overlap of different color lines in Figure 4.3. The reason is that the pressure gradient accelerations are identical at the same location even if the sizes are different; see the related term in Equation 2.43.

A higher vertical intercept indicates a larger initial pressure gradient felt by the bubble. The pressure gradient force has a global maximum at $r/r_v = 0.66$ and decays from the point in all directions, as shown in Figure 3.2d. Apparently, a higher intercept does not necessarily indicate a closer release point.

- Path to the vortex core (the plateau):

  The bubble reaches an approximately force equilibrium from the previous stage and maintains the situation because the pressure gradient changes within the bubble response time. This state will be slightly broken if the bubble is too large or the released points are too close to the vortex center.

  Interestingly, the velocity profiles of the large bubbles share an almost identical shape across the circulation strength, as in Figures 4.3 and 4.4. The underlying reason is that the constant C_D due to the high $\mathrm{Re_B}$ (Equation 2.40) makes $\dot{r}$ purely proportional to U_θ, thus Γ_∞, and finally the U_v. As a result, the dimensionless process with U_v collapses the large bubble data. Remind that the dimensional velocities are still different.

- From the core to the final point (the spikes):

  The bubble reaches a maximum velocity when the pressure gradient force reaches the maximum at roughly $r/r_v = 0.66$, as indicated in Figure 3.2d. This explains why the spikes occur at a similar spatial location and have the same magnitude for the

same bubble size, as in Figure 4.4. After the spikes, the bubble migrates until it reaches the prescribed capture radial location with a decrease in velocity.

Figure 4.4 share roughly the same narratives as Figure 4.3, but it shows a more explicit evidence that the radial velocity is nearly a stage variable with regards to the radial position. All the lines from different release positions will finally collapse together, which is important for developing a model.

4.2.3 *Development of the capture time model*

The three assumptions mentioned in the previous section will be employed to derive several capture time models. The idea is that the apparent radial force balance could predict the bubble radial velocity from the azimuthal flow velocity. Then the bubble capture time could be calculated from the temporal integral of the reciprocal of the radial velocity.

As already shown in Figure 4.2, the radial force balance means

$$F_{\mathrm{A}} + F_{\mathrm{P}} = F_{\mathrm{D}} + F_{\mathrm{In}}, \tag{4.3}$$

where F_{In} here represents the centrifugal force, an inertial force from the polar coordinate reference frame. Given that the total apparent mass is equal to the added mass, the force balance could be easily transformed into an acceleration balance:

$$\underbrace{\frac{U_\theta^2}{r}}_{\text{Added mass}} + \underbrace{2\frac{U_\theta^2}{r}}_{\text{Pressure gradient}} = \underbrace{\frac{3C_D}{4R}\dot{r}^2}_{\text{Drag}} + \underbrace{r\dot{\theta}^2}_{\text{Centrifugal}}, \tag{4.4}$$

where the azimuthal flow velocity U_θ has been shown mostly identical to the bubble one $r\dot{\theta}$. The added mass and centrifugal components can cancel out each other:

$$2\frac{U_\theta^2}{r} = \frac{3C_D}{4R}\dot{r}^2. \tag{4.5}$$

The bubble radial velocity can then be deduced from the flow azimuthal velocity.

Table 4.1: Variations of the capture time model.

C_D \ U_θ	Inviscid vortex	Lamb-Oseen vortex
Stokes	✓	✓
Schiller	✗	✓

Two formulations for both the azimuthal velocity (inviscid and the current Lamb-Oseen ones) and the drag coefficient (Stokes and Schiller ones) are applied to test the limit of the simplifications. With those formulations, four representations of $\dot{r}$ could be derived, but the combination of the inviscid vortex and Schiller drag would be neglected since the other three can already provide a clear and abundant insights into the modeling. Those variations are organized in a chart, Table 4.1.

Those with the Stokes drag formulation can be expressed analytically, while one with the Schiller drag cannot. The derivation process for the combination of Lamb-Oseen vortex and Stokes drag is displayed as an example. From the apparent radial acceleration balance, the corresponding inward radial velocity is

$$\dot{r} = \frac{2R^2}{9\nu_1}\frac{U_\theta^2}{r}. \tag{4.6}$$

The captured time, with some tedious integration, is thus

$$\begin{aligned} t_c &= \int_{r_0}^{r_{cap}} \frac{1}{\dot{r}}\,\mathrm{d}r \\ &= \frac{9\nu_1\pi^2 r_v^4}{\Gamma_\infty^2 R^2}\left(\frac{r^{*4}}{2} + \frac{\log\left(1-e^{-\varsigma r^{*2}}\right)}{\varsigma^2} - \frac{r^{*2}e^{-\varsigma r^{*2}}}{\varsigma(1-e^{-\varsigma r^{*2}})} + \frac{\mathrm{Li}_2(e^{-\varsigma r^{*2}})}{\varsigma^2}\right)\Bigg|_{r_{cap}}^{r_0}, \end{aligned} \tag{4.7}$$

where r^* is the normalized radial coordinate by the viscous radius, and Li_2 is known as the Spence's function or the dilogarithm defined as

$$\mathrm{Li}_2(z) = \int_1^z \frac{\log t}{1-t}\,\mathrm{d}t\,. \tag{4.8}$$

The capture time formulation could be reformed using the Buckingham Π theorem. The governing physical quantities are

$$R_0,\ r_\mathrm{v},\ \Gamma_\infty,\ r_0,\ t_\mathrm{c},\ \text{and}\ \nu_\mathrm{l},$$

of which the number is six, and the unique physics dimensions add up to two (length and time), which means that four carefully-chosen dimensionless parameters could describe the system:

$$\Pi_1 = \frac{\Gamma_\infty t_\mathrm{c}}{r_\mathrm{v}^2},\ \Pi_2 = \frac{R_0}{r_\mathrm{v}},\ \Pi_3 = \frac{r_0}{r_\mathrm{v}},\ \text{and}\ \Pi_4 = \frac{\Gamma_\infty}{\nu_\mathrm{l}}.$$

With the knowledge of

$$U_\mathrm{v} = \lambda \frac{\Gamma_\infty}{2\pi r_\mathrm{v}}, \qquad \text{(3.7 revisited)}$$

those dimensionless quantities are formulated in a more meaningful way:

$$t_\mathrm{c}^* = \frac{t_\mathrm{c} U_\mathrm{v}}{r_\mathrm{v}},\ R_0^* = \frac{R_0}{r_\mathrm{v}},\ r_0^* = \frac{r_0}{r_\mathrm{v}},\ \text{and}\ \mathrm{Re}_\mathrm{v} = \frac{U_\mathrm{v} r_\mathrm{v}}{\nu_\mathrm{l}}.$$

Wherein the capture time is normalized by the revolution time scale of the vortex, and the circulation is embedded into a Reynolds number characterized by the vortex diffusion scale. Thus, the capture time could be re-expressed in a dimensionless way:

$$t_\mathrm{c}^* = \frac{9}{4}\frac{\lambda^2}{\mathrm{Re}_\mathrm{v} R_0^{*2}} \left(\frac{r^{*4}}{2} + \frac{\log\left(1 - e^{-\varsigma r^{*2}}\right)}{\varsigma^2} - \frac{r^{*2} e^{-\varsigma r^{*2}}}{\varsigma\left(1 - e^{-\varsigma r^{*2}}\right)} + \frac{\mathrm{Li}_2\left(e^{-\varsigma r^{*2}}\right)}{\varsigma^2} \right) \Bigg|_{r_\mathrm{cap}^*}^{r_0^*}. \tag{4.9}$$

In the original narrative of Oweis *et al.* (2005), the flow velocity is simplified with an inviscid vortex field of the same circulation strength, so their capturing time is formulated similarly but without the shaded terms in Equation 4.9, i.e., the capture time formulation with the Stokes drag and the Lamb-Oseen vortex contains only the non-shaded term in Equation 4.9.

The assumption of applying the Stokes drag harshly limits the analysis of the large bubble, where the real drag coefficient reaches

the plateau of 0.445 if the bubble Reynolds number is sufficiently large, as shown in the Schiller's sphere drag formulation:

$$C_D = \begin{cases} \dfrac{24}{\mathrm{Re_B}}\left(1 + 0.15\,\mathrm{Re_B}^{0.687}\right) & \text{if} \quad \mathrm{Re_B} < 955, \\ 0.445 & \text{if} \quad \mathrm{Re_B} \geq 955. \end{cases} \tag{2.40 revisited}$$

Thus the combination of the Schiller drag formulation and the Lamb-Oseen vortex is thus of the most interest. The Schiller drag formulation is complex, but the radial velocity could still be easily found by Equation 4.5 via the nonlinear root-finding algorithms such as Newton-Raphson or other similar methods. Then the capturing time could be obtained using numerical integration techniques such as the quadrature or Simpson methods.

In this subsection, three (quasi-) analytical variations for the capturing time model are derived. All are based on the apparent radial acceleration balance in the polar coordinates. The first two are based on the Stokes drag formulation with different complexities in the azimuthal velocity profile. The last one is the most complex variation with the Schiller drag formulation and the Lamb-Oseen vortex.

4.2.4 *Comparison between model variations*

The subsection explains how the choices among the vortex and drag formulations alter the capture time results.

Figure 4.6 shows the deviation between the model variations and the numerical simulation of bubbles released from different radial positions. Generally, the deviations between the simulation's and model's values increase when approaching the vortex center because the further bubble has a longer time scale and thus the more negligible acceleration effect, which is an essential foundation of the model. The variations using the Stokes formulation significantly underestimate the capture time because the Stokes drag is incredibly small in the large $\mathrm{Re_B}$ zone, so the inward radial velocity is hugely amplified by the pressure gradient, resulting in the low capture time. This is

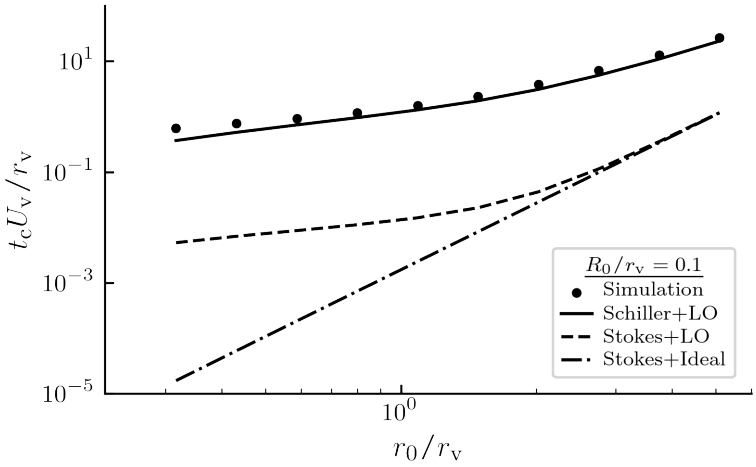

Figure 4.6: Comparison between capture time model variations.

also the reason why the original model in Oweis *et al.* (2005) deviates from their simulation results. Although the gap caused by the Stokes drag is too tremendous to fill, including the Lamb-Oseen vortex in the model enhances the accuracy a bit since the pressure gradient of an inviscid vortex deviates from the Lamb-Oseen one, especially within the viscous core.

In short, the model with either the inviscid vortex or the Stokes drag can cause the underestimation of the capture time. As a result, only the combination of Lamb-Oseen vortex and Schiller formulation will be included in the following discussions and detailed examinations.

4.2.5 *The capture time trend and the model limitations*

Figures 4.7 and 4.8 sequentially show the capture time comparisons concerning the released position and the bubble radius. Intuitively, the bubble with a closer initial released position indeed will be entrapped faster. In general, the larger bubbles are also captured more rapidly than the smaller ones since the influence of the pressure gradient term in Equation 2.43 prevails over the drag one when R

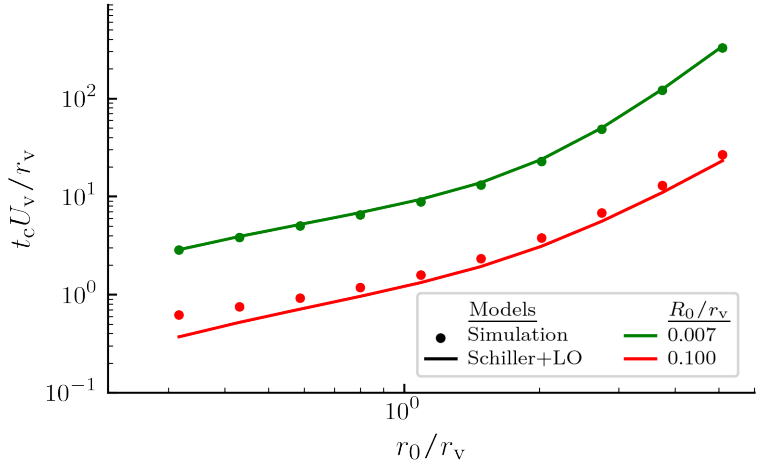

Figure 4.7: Captured time as a function of the released position via the analytical and numerical approaches.

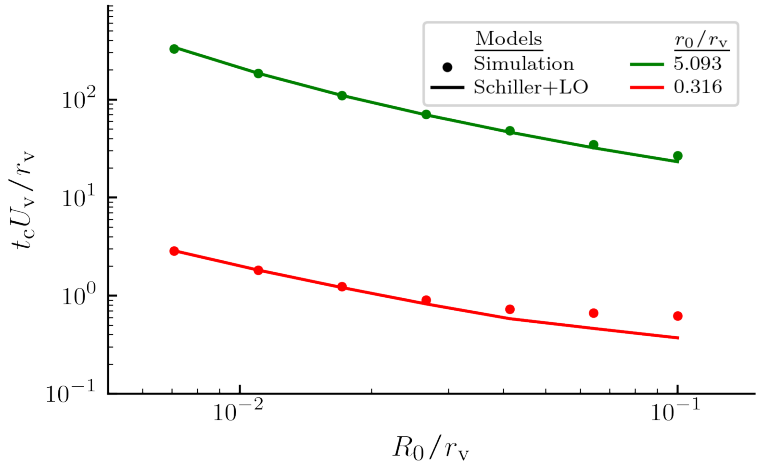

Figure 4.8: Captured time as a function of the bubble size via the analytical and numerical approaches.

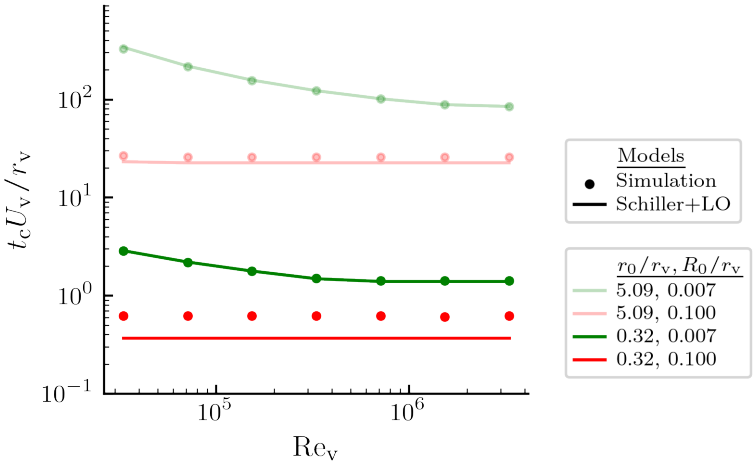

Figure 4.9: Captured time as a function of the vortex Reynolds number via the analytical and numerical approaches.

increases. In other words, the large bubble is more susceptible to the pressure gradient force. Figure 4.9 shows the rest influencing parameters – the core Reynolds number (effectively the circulation strength). It is found that the circulation strength indeed makes the bubble captured more quickly. Not to be disguised by the normalization process, the dimensional capture time decreases when the core Reynolds number increases. The only difference is that the dimensional capture time decrease with Γ_∞^2 for the small core Reynolds number but Γ_∞ for the large core Reynolds number. The plateau in the dimensionless capture time is also a result of the drag coefficient plateau in the high bubble Reynolds number zone, where the inward radial velocity is proportional to the azimuthal velocity and thus the circulation strength to the power of unity; see Equation 4.5. The inference is more explicit in Figure 4.4. The normalized inward radial velocities do not change with the circulation strength for the large bubble, so the resultant capture time should also be nearly identical throughout the core Reynolds number.

The capture time model based on the Schiller drag can almost accurately predict the capture time. This indicates that the assumption of the force balance can generally be accepted. Another evidence is shown in Figure 4.4. The velocity profiles predicted by the model ade-

quately match with the simulation results. However, one can observe that the large bubble cases yield a more significant deviation. The underlying reason is that the large bubble has a shorter time scale and will also reach a higher velocity level, so the acceleration effect is sometimes unavoidable, breaking the model foundation. Another possible reason is that the initial acceleration stage indicated in Figure 4.3 occupies a significant portion of the simulation time. Whereas the large bubble's time scale is short, so the portion of the stage is not negligible. This is quite apparent in Figure 4.4. The transition from the initial acceleration stage to the next stage (model-predicted velocity zone) of the large bubble is not as sharp as the small bubble, so there is a general underprediction of the bubble capturing time for the large bubble.

Briefly speaking, the large bubble, closer released position and higher pressure gradient force will cause a shorter capture time. On the other hand, the model reaches its limitation for the following reasons. The first one is that if the time scale is too small, which happens when the large bubble is being captured, for example, the acceleration will be too pronounced to neglect. The second one, attributed to the deficit in the numerical simulation, is that the initial acceleration stage sometimes contributes to a noticeable portion of the total traveling time, which also likely occurs when the time scale is small.

4.3 THE ROLES OF DIFFERENT FORCES

The acceleration analysis shows how different forces interact in various stages and which roles they play. Note that the bubble accelerations instead of the forces are analyzed to concentrate on the kinematic effects. Also, only the furthest released bubbles are investigated, for they cover most of the motion stages. Furthermore, the accelerations are all normalized based on U_v and r_v, which could be regarded as the nominal centrifugal acceleration. Recall that the relative velocity is dominated by the radial component, so the force directions in principle could be simplified as Figure 4.2.

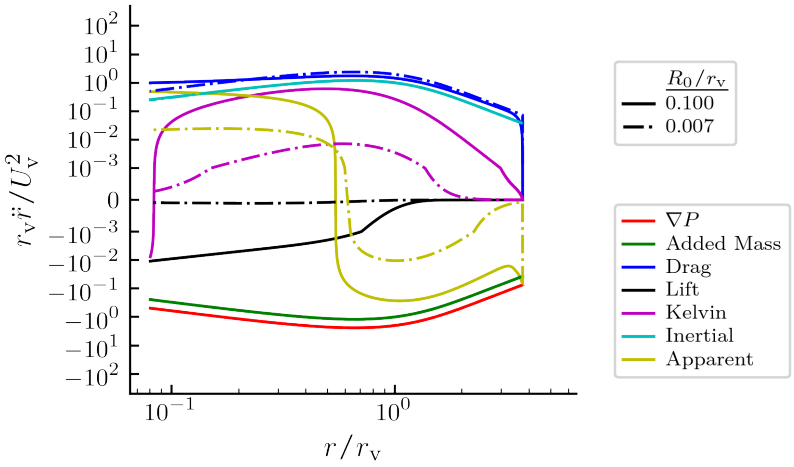

(a) Radial components.

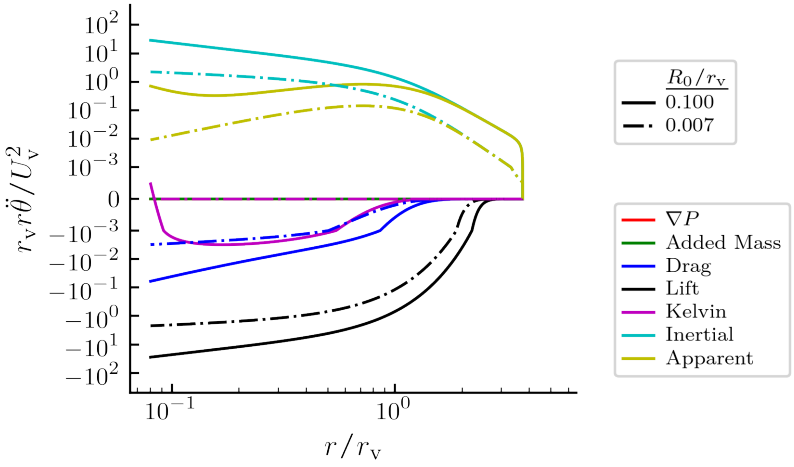

(b) Azimuthal components.

Figure 4.10: The acceleration terms from $r_0/r_v = 3.74$ in different directions.

The acceleration profiles are shown in Figure 4.10. The figures are plotted in a so-called symmetric logarithmic scale (corresponding to the `symlog` commands). If the absolute value of the ordinate value is greater than a threshold, $\pm 10^{-3}$ in this case, the plot is in logarithmic scale, while in linear scale (normal `plot` commands) within the thresholds. The advantage is to show the transitions from the positive to negative values without reaching the singular points caused by the logarithmic function.

The radial acceleration components are normalized by U_v^2/r_v. There are four dominant forces in the radial direction: pressure gradient, added mass, drag, and inertial (centrifugal) forces. Generally, when a bubble is far from the vortex core, the time scale of the bubble is relatively slow. Thus the acceleration is not prominent, and the forces are roughly balanced. Consequently, if bubbles are released further away, the deviation of the capture times between the model and the simulation is typically smaller. Interestingly, the aforementioned four accelerations seem to be not a function of bubble size. The added mass, pressure gradient, and inertial accelerations are only proportional to U_θ^2/r or to $r\dot{\theta}^2$, so the size effect disappears. The drag acceleration is linked to the pressure gradient term since the apparent radial acceleration is roughly null among the cases.

The azimuthal accelerations, $\ddot{\theta}$, are normalized with U_v^2/rr_v. In this direction, only two forces dominate: the lift and inertial (Coriolis) forces. As mentioned in the previous section, the relative azimuthal velocity is roughly zero, reflected in the magnitudes of the drag and Kelvin impulse accelerations. Lift force, in this case, plays a crucial role in balancing the inertial force, especially inside the viscous core. This is not coincidence but a feature of the solid body rotation: $\omega = 2\dot{\theta}$; see Figure 3.3. With the preceding relationship and the characteristic of the relative motion, one can easily show that the lift is balanced with the inertial force:

$$\begin{aligned} \text{Lift acceleration:} \quad & (\mathbf{U} - \mathbf{U}_B) \times \boldsymbol{\omega} = \omega \dot{r}, \\ \text{Coriolis acceleration:} \quad & 2\dot{r}\dot{\theta} \qquad\qquad\quad = \omega \dot{r}, \end{aligned} \tag{4.10}$$

where $\mathbf{U} - \mathbf{U}_B$ is the relative velocity who has a radial dominant value, $\dot{r}$, and ω currently represents the vorticity magnitude.

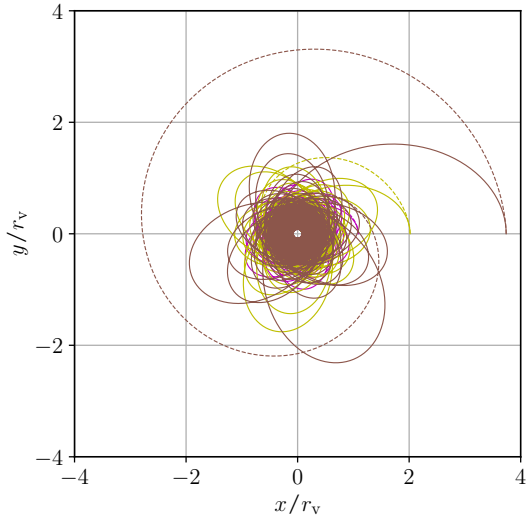

Figure 4.11: The bubble paths without the lift. The colors represent the different released locations while the dash and solid lines stand for $R_0/r_v = 0.01, 0.1$, respectively.

4.3.1 *The role of lift – an exhaustive analysis*

Abiding the conservation law of angular momentum, the azimuthal bubble velocity will increase when migrating into the core if the lift force is taken away. However, the excessive centrifugal force in such a high level of the azimuthal velocity will throw the bubble again into a larger radial distance, which is analog to the apsidal orbital precession in celestial mechanics. Thus, the motion near the center will be chaotic, especially for the large bubble, whose damping from the drag is not predominant, as shown in Figure 4.11. The angular momentum[13] evolution, Figure 4.12, shows more insightful data. The bubbles tend to stay at the same angular momentum level instead of going downward, indicating that there is no sufficient azimuthal-force-induced moment to reduce the angular momentum.

13 Again, the angular momentum here focuses on only the kinematic part, so the specific angular momentum $r^2\dot{\theta}$ is introduced.

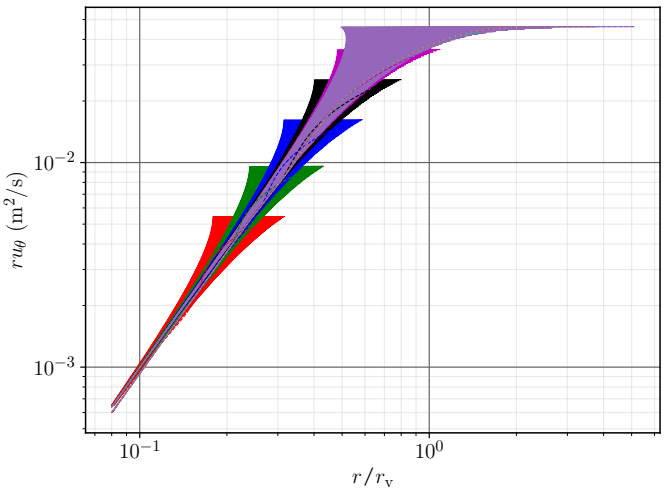

Figure 4.12: The bubble angular momentum evolution without the lift ($R_0/r_v = 0.1$). The different colors represent the different released locations.

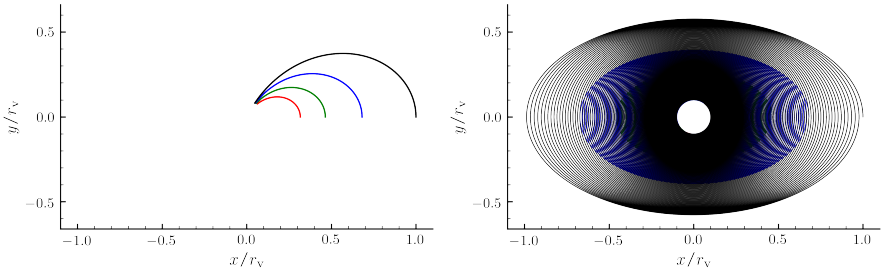

(a) Paths with the lift.

(b) Paths without the lift.

Figure 4.13: Analytical path solutions from the system of ODE.

Successively, a linearized Ordinary Differential Equation (ODE) model is introduced to elaborate the issue, which is inspired by L. Zhang *et al.* (2016). If the vortex is simplified into the solid-body part of an equivalent Rankine vortex, i.e., the vorticity is concentrated but evenly distributed in the viscous core, the bubble motion equation, with the lift, could be simplified into a system of two-dimensional ODE:

$$\begin{aligned} \frac{\mathrm{d}^2x}{\mathrm{d}t^2} + a\frac{\mathrm{d}x}{\mathrm{d}t} + \omega\frac{\mathrm{d}y}{\mathrm{d}t} + \frac{1}{4}\omega^2 x &= -\frac{1}{2}a\omega y, \\ \frac{\mathrm{d}^2y}{\mathrm{d}t^2} + a\frac{\mathrm{d}y}{\mathrm{d}t} - \omega\frac{\mathrm{d}x}{\mathrm{d}t} + \frac{1}{4}\omega^2 y &= \frac{1}{2}a\omega x, \end{aligned} \tag{4.11}$$

where

$$a = \frac{9\nu_1}{R^2}, \quad \text{and} \quad \omega = \frac{\Gamma_\infty}{\pi r_\mathrm{v}^2}.$$

The system of ODE could be analytically solved by the conversion of ODE and matrix eigenvalue technique; readers are referred to any engineering mathematics textbook for further information; see Kreyszig (2011) for example. As shown in Equation 4.11, even if the bubbles are too large, the third term at the left-hand side can still be the source of damping and eventually stabilize the system. However, the equations of motion without the lift read

In the literature, they view Equation 4.12 as the simplified equation with lift, but the correct one should be Equation 4.11.

$$\begin{aligned} \frac{\mathrm{d}^2x}{\mathrm{d}t^2} + a\frac{\mathrm{d}x}{\mathrm{d}t} + \frac{3}{4}\omega^2 x &= -\frac{1}{2}a\omega y, \\ \frac{\mathrm{d}^2y}{\mathrm{d}t^2} + a\frac{\mathrm{d}y}{\mathrm{d}t} + \frac{3}{4}\omega^2 y &= \frac{1}{2}a\omega x. \end{aligned} \tag{4.12}$$

The lift-induced damping terms diminish, so the system becomes an underdamped oscillation if the bubble is large enough. The comparison of the analytical path solutions is depicted in Figure 4.13. One with the lift indeed shows an overdamped behavior, while one without the lift shows an underdamped behavior.

In a nutshell, the lift force acts in the azimuthal direction and is a retarding source for the angular momentum. By balancing out the Coriolis force, it stabilizes the system.

4.4 REGIME PLOT

The regime plot is a kind of phase plot describing the state of a bubble group, which is initially proposed by Ir. Nanda. Several bubbles are seeded numerically, and their physical quantities are recorded throughout the tracking time. Plotting the physical quantities against each other reveals some secrets behind the spiral lines, as he suggested.

4.4.1 *Underlying idea of the regime plot*

The bubble motion equation is consulted to find the dominant physical quantities. By assuming the added mass coefficient is one-half, water density is far higher than that of the bubble, and the Kelvin Impulse term is not pronounced enough, the bubble motion equation could be simplified toward

$$\frac{\mathrm{d}\mathbf{U}_\mathrm{B}}{\mathrm{d}t} = 3\frac{\mathrm{D}\mathbf{U}}{\mathrm{D}t} - 2\mathbf{g} + \frac{3}{4}\frac{C_D}{R}|\mathbf{U}-\mathbf{U}_\mathrm{B}|(\mathbf{U}-\mathbf{U}_\mathrm{B}) + (\mathbf{U}-\mathbf{U}_\mathrm{B})\times\boldsymbol{\omega} + \frac{3}{R}(\mathbf{U}-\mathbf{U}_\mathrm{B})\dot{R}. \quad (2.43 \text{ revisited})$$

Thus, the representative quantities are

$$\mathbf{U}_\mathrm{B},\ \mathbf{U},\ \boldsymbol{\omega},\ g,\ R,\ C_D,\ C_L,\ \text{and}\ \alpha.$$

With the knowledge of

$$\left|\frac{\mathrm{D}\mathbf{U}}{\mathrm{D}t}\right| \gg g,\ C_D = C_D(\mathrm{Re}_\mathrm{B}),\ \mathrm{Re}_\mathrm{B} = \frac{2|\mathbf{U}-\mathbf{U}_\mathrm{B}|R}{\nu_\mathrm{l}},\ \text{and}\ \alpha = \frac{|\boldsymbol{\omega}|R}{|\mathbf{U}-\mathbf{U}_\mathrm{B}|},$$

the set of quantities degenerate to

$$\mathbf{U},\ \mathrm{Re}_\mathrm{B},\ \text{and}\ \alpha. \quad (4.13)$$

Meanwhile, the flow field quantities are dependent on the radial position r, so the final three quantities are

$$r,\ \mathrm{Re}_\mathrm{B},\ \text{and}\ \alpha. \quad (4.14)$$

Ir. Nanda suggests that recording the three physical quantities might reveal the mechanism of bubble behaviors near the vortex.

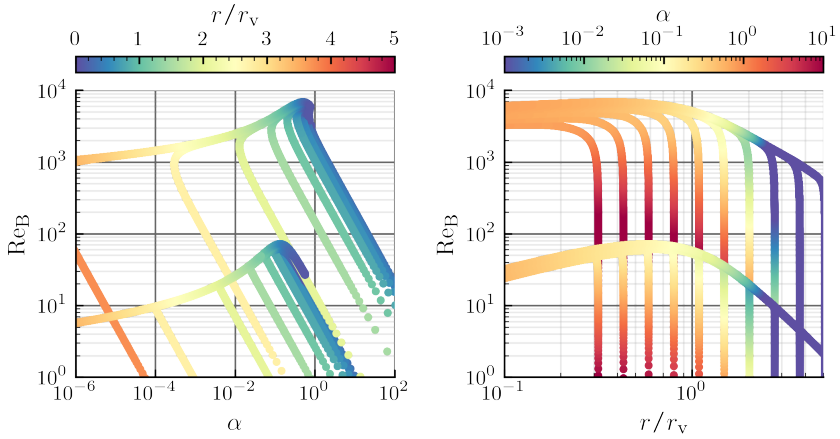

Figure 4.14: Regime plot of the numerical simulation. The upper bundle represents the large bubble at different released positions while the lower ones for the small bubbles.

4.4.2 *Results from the numerical simulation*

The numerical regime plot, Figure 4.14, only presents the largest and smallest bubbles, while all the others resemble the demonstrated behaviors but lie between lines of the extreme bubble sizes. Since all the bubble sizes do not change much throughout history, Re_B can be regarded as an indicator for the bubble radial velocity.

The Re_B-α line also consists of three stages, analog to the velocity stages, which are shown separately in Figure 4.15. The narrative is also similar to Section 4.2.2, but with more attention to the abscissas of the regime plot:

- Initial acceleration stage (left-leaning line segment):

  The bubble is accelerating because the initial radial velocity is not prescribed. Also, because Re_B is proportional to the radial velocity and α is inversely proportional to that, the lines have the slope of negative unity. Another reason is that the bubble does not move much during the initial acceleration stage, so the experienced vorticity stays nearly constant.

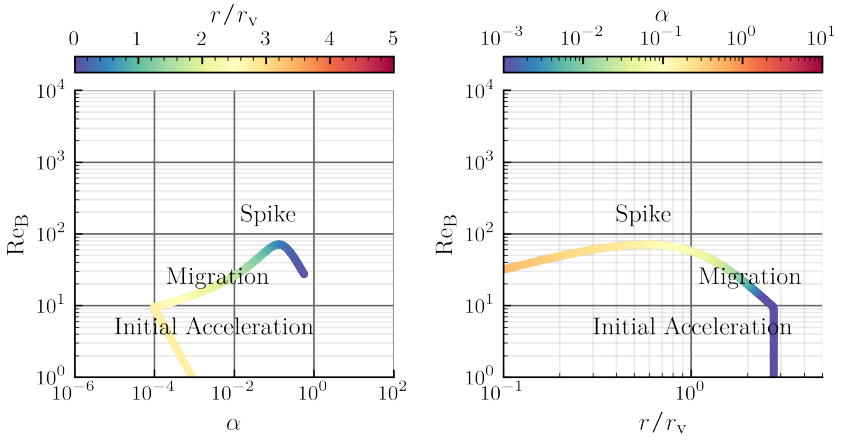

Figure 4.15: Different stages in the bubble regime plot.

- Path to the vortex center (right-leaning curve segment):

  The bubble is still moderately migrating, but the experienced vorticity also increases since it starts migrating inward effectively. Besides, the curves of different released points coincide with each other owing to the state-dependent nature of the radial velocity, as mentioned before.

- Entrapment by the vortex center (blue peak of line clustering):

  The bubble has kept traveling to the near center point, although there is still some deceleration at the ending stage, which can be observed from the Re_B-r/r_v plot. The peak velocity comes from the maximum pressure gradient occurring at $r/r_v = 0.66$ and is characterized by the blue peak. The ending line also has a negative unity slope because the core's vorticity is nearly constant.

On the other hand, the Re_B-r/r_v plot has only two distinguishable parts: first, the initial acceleration stage and the path to the vortex center. The arguments are similar to the Re_B-α plot with a clearer view of the velocity evolution. Actually, the plot resembles Figure 4.4 because Re_B, as mentioned above, could serve as an indicator of the radial velocity. Further secrets should be unveiled in the realistic tip vortex simulation case.

This page intentionally left blank

5

BUBBLE MOTIONS IN THE REALISTIC TIP VORTEX FLOW

The chapter directly applies the CFD simulations validated in Chapter 3 as the background flow field and investigates the bubble motion around the tip vortex. The results will be compared to some aspects of the previous ideal vortex and the experimental ones.

5.1 CASE DESCRIPTIONS

The inflow velocity is chosen to be 7.15 (m/s), and the corresponding base chord Reynolds number Re_c is 8.96×10^5, a bit higher than the Ir. Nanda's one, 7.07×10^5, but is still comparable.

As motioned before, the bubbles are not tracked throughout the flow domain. Instead, three domain clips are extracted to let the bubbles travel inside, as shown in Figure 5.1. The domain clips are exactly the agent interpolation grid as mentioned in Section 2.3.3. The large domain includes the foil to investigate its effect. The first small domain is designated to explore an interesting phenomenon called stagnation bubble which will be addressed later. The second small domain is extracted to achieve the accuracy and the direct regime plot comparison with the experimental one. The maximum simulation time is set when most bubbles have passed through the domain box. For example, it takes about 0.1 (s) for most bubbles to exit the general domain.

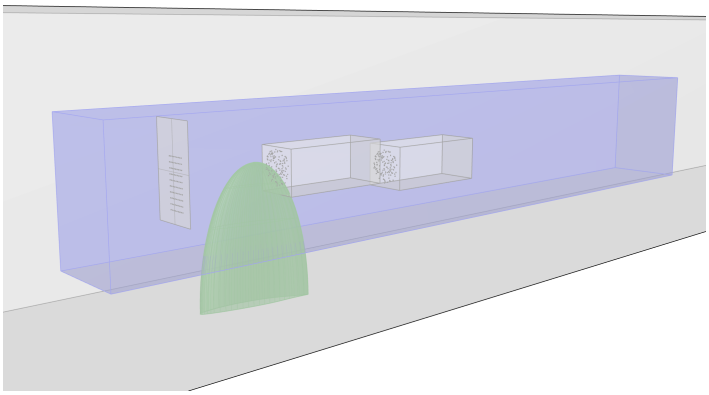

Figure 5.1: The original CFD flow domain with two clipped sub-domain and the corresponding initial bubble locations.

The seeding locations are shown as the black dots in Figure 5.1. In the general large-domain simulation, bubbles are seeded on an upstream plane with $x/c_0 = -0.75$, of which the crossing point of the two perpendicular lines on the plane is the projection point of the foil tip. The bubble seeding locations are similar to the streamlines into the vortex core to eliminate particle locations that are potentially useless (Hsiao & Pauley, 1999), so they are asymmetric about x-z plane. On the other hand, the bubbles are placed randomly around the local upstream center in the small-scale simulation.

Contrary to the narrow range of the bubble sizes in the ideal vortex case, the bubble size ranges from a micron to a millimeter to cover most sizes of a usual bubble population:

$$R_0 = 1.00, 3.16, 10.00, 31.62, 100.00, 316.22, 1000.00\ (\mu\mathrm{m}).$$

The cavitation number is 1.6 as in Ir. Nanda's experiment setting. Furthermore, the corresponded simulations without bubble dynamics are also carried out, i.e., $\sigma = \infty$ to inspect the bubble expansion effect.

Previously, it has been argued that the pressure gradient force should be expressed in the material derivative form. However, the material derivative introduces numerical instability to the time marching due to its chaotic nature and the interplay with the discretization

error, so only the pressure gradient is applied for all the following simulations.

5.2 LIMITATIONS OF THIS SIMULATION

Constrained by the applied methods and the computational capacity, the tip vortex cavitation case has several limitations.

The first one is that the current LPT method might not be adequate to resolve the shape and motion of the giant bubble. To estimate when a bubble will not be spherical, Weber number,

$$\mathrm{We} = \frac{2\rho|\mathbf{U} - \mathbf{U}_\mathrm{B}|^2 R}{\eta}, \tag{5.1}$$

is introduced as a ratio between drag (form-breaking effect) and surface tension (form-maintaining effect). When the Weber number is larger than the unity, the bubble tends to deform away from a sphere and thus challenges the validity of the current LPT method. In the simulation, the Weber numbers of some large bubbles, especially when the bubble dynamics is included, are already far larger than unity, so the result is highly limited.

Next, the computational capacity also highly limits this part of the research. The cases are carried out without the adequate resolution around the tip vortex due to the memory-intensive agent structured grid as mentioned in Section 2.3.3. Nevertheless, thanks to Dr. Lidtke, he runs a general case with the full capacity directly through a self-developed tool upon ReFRESCO. That is to say, the agent interpolation grid is removed, and the required flow variables are directly interpolated from the original unstructured grid. The simulation data is integrated into this chapter to discuss the influence of the interpolation error. The case will be called "performance case" hereafter for simplicity.

In consequence, the chapter focuses more on qualitative reasoning, while the quantitative discussions will be somewhat avoided.

5.3 WINDOW ANALYSIS

Not all the bubbles from the upstream ambiance can travel into the vortex core and contribute to the tip vortex cavitation. Unlike the previous case with only the ideal vortex, the tip vortex case comes with a foil and a finite streamwise length limit. The pressure field induced by the hydrofoil will hinder the bubble from reaching the core, such as the leading edge stagnation pressure or the finite-span effect. On the other hand, the finite streamwise distance limits the maximum bubble evolution time. As a result, it is of interest to classify under which circumstance a bubble will enter the core.

Whether or not the vortex can capture the bubble is the function of the initial bubble positions, the initial bubble size, the cavitation number, and the vortex strength, as shown in the previous chapter. The research is mainly focused on the initial bubble positions and sizes. Only the bubbles that go into the core within $x/c_0 = 0.05\text{-}2.5$ are considered since those more downstream seldom contribute to the cavitation inception, and those further upstream are just experiencing a strong initiating roll-up process and are hard to measure accurately. The capturing radius is set to be the radial distance smaller than a certain fraction of the averaged viscous core radius $2.5\,(\mathrm{mm})$, where a typical viscous core radius is about $5.0\,(\mathrm{mm})$ as present in Chapter 3.

A bubble can be captured via two mechanisms: following streamline into the vortex center from the upstream or via the vortical pressure gradient after the bubble passes the foil. The small bubbles generally follow the former method, while the large bubbles usually get entrapped by the latter approach. As a result, the large bubbles are captured more possibly, as shown in Figure 5.2.

From the shape in Figure 5.2, it is deduced that the bubbles can only be captured if not located near the lower suction side. Due to the spanwise downward $(-z)$ velocity induced by the finite-span effect, the bubbles situated among the aforementioned locations are pulled down. It is thus more impossible for them to reach the vortex core.

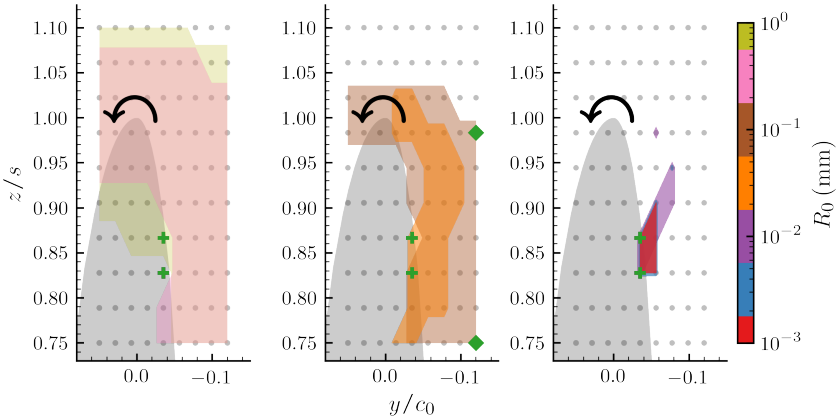

(a) Normal simulation.

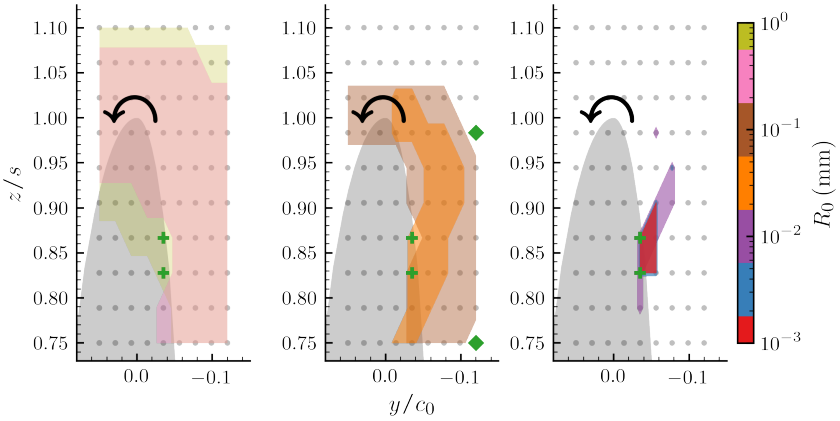

(b) Simulation without bubble dynamics.

Figure 5.2: Window analysis for two simulation scenarios. Panel from left to right roughly represents the large, medium, and small bubbles. The green diamonds represent the bubble expansion effect across different σ and the green plus symbols stand for the bubble screening effect across different R_0. Note that the y direction is flipped viewing from the upstream.

It is also found that the large bubbles, especially for those who are shaded with pink and brown, cannot be easily captured at the pressure side of the projected foil shade (green plus symbols). On the other hand, the small bubbles, such as the orange-shaded and red-shaded ones, can be entrapped effortlessly. The reason behind it is similar to the one in the sheet cavitation. The strong stagnation pressure gradient field in front of the hydrofoil screens the large bubbles, which are more sensitive to the pressure gradient and has less possibility of entering the capturing zone, unless the original bubble size is sufficiently large so that it can be quickly captured after passing the pressure screening zone.

The green diamonds indicate that the medium bubble could be captured with the bubble dynamics even if the initial released position is far from the tip vortex. The bubble can expand to a larger one and finally be captured by the tip vortex. However, the bubble capturing zone does not deviate much with or without the bubble dynamics. This could probably be a result that large bubbles have already passed the threshold to be captured, so any expansion is only the accelerator instead of the catalyst, while the small bubbles, of which the size changes are reluctant to the pressure change and which mainly follow the streamlines, behave similarly in both cavitation numbers.

In this section, it is observed how the bubble capturing is influenced by the cavitation number and how the surrounding flow field induced by the foil affects the bubble motion. The large bubble has more possibility of being captured than the small one but is also more influenced by the pressure field, such as the stagnation pressure field.

5.4 BUBBLE POPULATION EVOLUTION

Bubbles close to the tip vortex are explicitly related to the cavitation inception. Apart from the bubble capture, it is crucial to quantify the bubble population in every section to devise conclusions such as the cavitation hotspots. The flow field is split into sub domains with

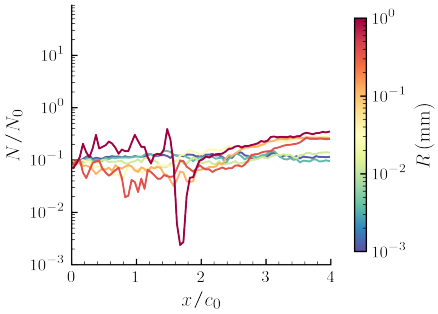

(a) Normal simulation.

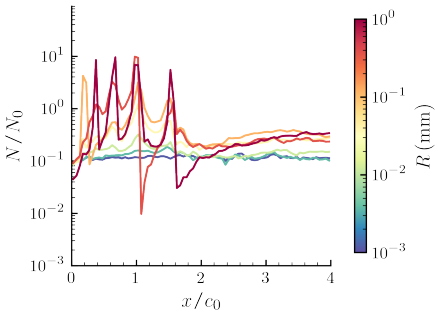

(b) Simulation without bubble dynamics.

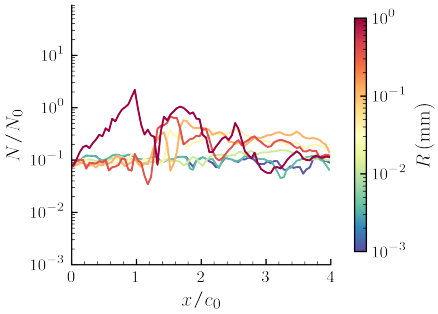

(c) Performance case.

Figure 5.3: Bubble population for several simulation scenarios.

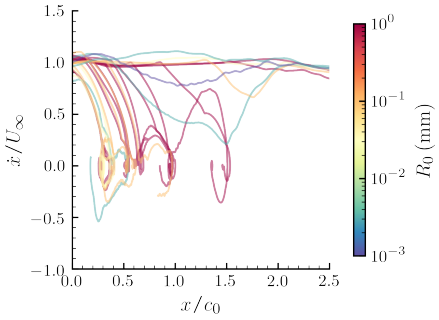

(a) Normal simulation.

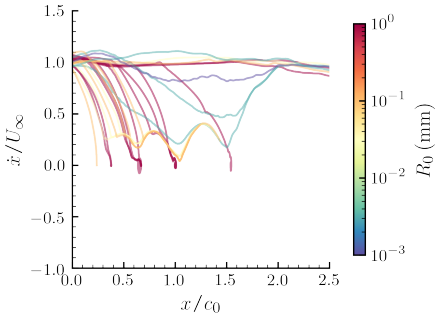

(b) Simulation without bubble dynamics.

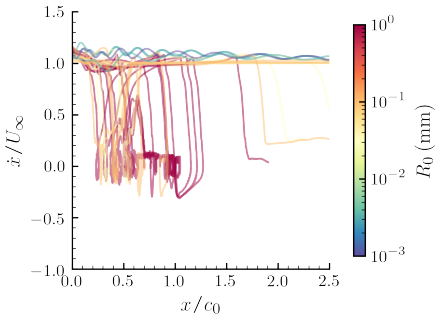

(c) Performance case.

Figure 5.4: Axial velocity with regard to the axial coordinates, with window averaging along time interval of 1 (ms) to extract the trends.

$\delta x/c_0 = 0.1$, and then the ratios of the bubbles near the tip vortex to the original number of bubbles are recorded for each bubble size and each sub domain. The "near" region is defined by a radial distance of 7 mm to cover roughly $1.5r_v$. Note that N/N_0 can be larger than 100% since the apparent bubble number increases if some bubbles spend more time there.

From Figure 5.3, the large bubbles tend to accumulate at the near downstream, while the small bubbles can be successfully advected downstream after being captured. The phenomenon can also be clearly seen in Figure 5.4. The large bubbles are more readily being captured to the (quasi-) limit cycles or the stable nodes. The phenomenon also reflects in several spikes of Figure 5.3b. The accumulation of the large bubble upstream is caused by the stagnation bubbles, of which the theoretical base and detailed analysis will be present in the next section.

The number of bubbles from the simulation without bubble dynamics surpasses one with bubble dynamics because the bubble dynamics will propel the bubble growth to an unrealistic size and eventually be driven away from the tip vortex due to the numerical instability and interpolation errors. Still, the accumulation of the large bubble is observed upstream. In the simulation with bubble dynamics, the medium bubbles with the size of $\mathcal{O}(100)$ (μm), characterized by the yellow colors, have expanded to larger sizes, so there are observable number deductions, while the simulation without the bubble dynamics does not have this effect.

The performance case has provided the opportunity to explore the effect of the interpolation error. It is observed that the bubbles possess different detailed behaviors before and after the grid refinement, either in the bubble population or the axial velocity profiles. The bubble capturing speeds, slopes in the axial velocity profiles, are even different. However, the qualitative behaviors are still similar. Hence, the chapter focuses on the phenomenon explanation instead of the quantitative description as mentioned before.

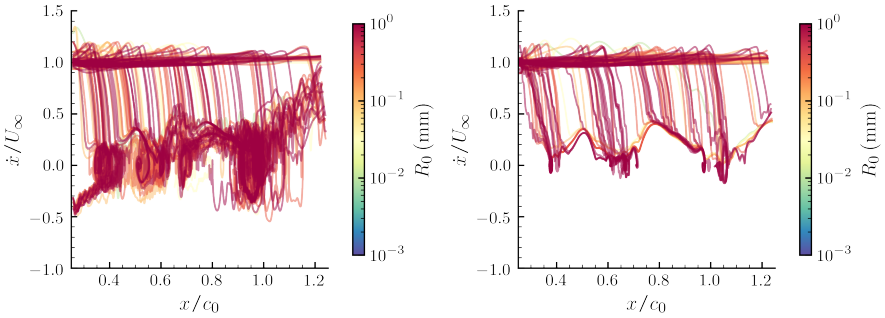

(a) Normal simulation.

(b) Simulation without bubble dynamics.

Figure 5.5: Axial velocity with regard to the axial coordinates, with window averaging along time interval of 1 (ms) to demonstrate the trend.

5.5 STAGNATION BUBBLE

As mentioned in the previous section, the stagnation bubble phenomenon dominates the bubble population evolution to some extent. However, since the general solution does not fully resolve the background carrier flow field, there is still a possibility that the stagnation bubble is a side effect of the interpolation error. Consequently, another specific small-scale simulation is carried out to rule out the effect. Figure 5.5 shows the simulation result. All the fine grid simulations indicate the existence of the stagnation bubbles. Figure 5.4c has also sustain the statement. Some of the bubbles are even driven upstream. It is more confident to declare that the likelihood of the interpolation error has drastically reduced. A series of attempts to describe the phenomenon with models are carried out afterward.

5.5.1 *A possibility of developing the model*

The drag force acts in the $+x$ direction, while the axial pressure gradient and added mass forces act in the $-x$ direction if a static bubble is placed in the center. One would reasonably expect that, due to the interplay of the drag, pressure gradient and added mass

forces, the bubbles might stagnate, and some will even be adversely advected.

A fully roll-up vortex model from Moore *et al.* (1973) is applied to gain some qualitative insight into the force balance at each streamwise point. The pressure profile along the vortex center is expressed in

$$P(x) = \frac{\rho\zeta^2}{2(\nu_1 x/U_\infty)^m}\int_{-\infty}^{0}\chi^{-1}V_m^2(\chi)\,\mathrm{d}\chi\,, \tag{5.2}$$

where

$$\begin{aligned}\zeta &= \frac{U_\infty\alpha_{\text{foil}}\sqrt{6c_0}}{\pi},\\ V_m(\chi) &= 2^{-m}\Gamma(1.5-0.5m)(-\chi)^{0.5}{}_1F_1(0.5+0.5m;2;\chi).\end{aligned} \tag{5.3}$$

$\Gamma(z)$ is the mathematical Gamma function, not to be confused with the circulation strength, while ${}_1F_1(a;b;z)$ is the Kummer confluent hypergeometric function. α_{foil} is the foil angle of attack in radian. m is the lifting line distribution factor, which is $1/2$ for the elliptical loading case. The axial pressure gradient can be easily found by the numerical integration and analytical method dealing with x. The axial velocity is predicted by roll-up mass balance and the momentum deficit from the boundary layer:

$$-\frac{U_x(0)}{U_\infty} = -\frac{6\alpha_{\text{foil}}^2}{\pi^2}\left(\frac{c_0}{x}\right)^{0.5}\mathrm{Re_c}^{0.5}\varepsilon_m + 0.28\left(\frac{c_0}{x}\right)^{0.5}, \tag{5.4}$$

from which the drag force could be deducted. ε_m is a variable constant with regard to the loading condition, which is -0.128.

Reader should notice that the vortex formulation is merely acceptable. It is found that the axial velocity within a particular range becomes negative, which is nonphysical. As a result, the model can only provide a qualitative picture.

Figure 5.6 shows that, in this model, the bubble is not necessarily staying at a particular force balance position but instead reaching the point and going backward since it predicts an unstable fixed point, which is contrary to the observation from the simulation. On the

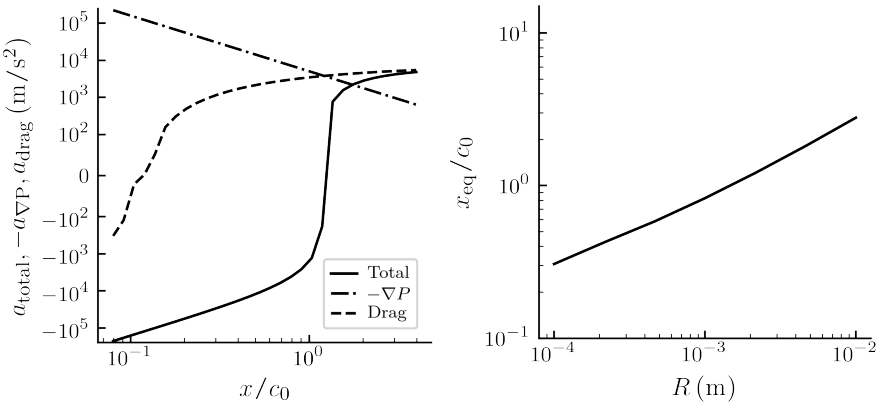

(a) Example of force on a fix bubble ($R = 2.15\,(\text{mm})$) on each streamwise point.

(b) Force balance point of different bubble sizes.

Figure 5.6: Force balance of different scenarios. In the symmetric logarithmic scale with the threshold of 10^{-3}.

other hand, the model correctly explains that the stagnation point of the large bubble is further downstream than that of the small bubble. This is also observed in Figure 5.4a, where the small bubbles stagnate only near the stable upstream points.

5.5.2 *An additional factor to be further investigated*

Although it is appealing to develop an intuitive model from the opposite forces, the drag, pressure gradient and added mass forces, the model can only predict the backward tendency, but the bubble oscillation around a steady node is not even modeled. It is suspected that the lift force also plays an important role but is not accounted for in the model.

To verify the statement, Lissajous curves plotted between the axial acceleration components of the forces are shown in Figure 5.7. Parts of the graph tend to collapse into an 135°-inclined line, meaning that the lift force component truly fills the gap to make the bubble oscillate. Otherwise, purely the drag and the pressure gradient force

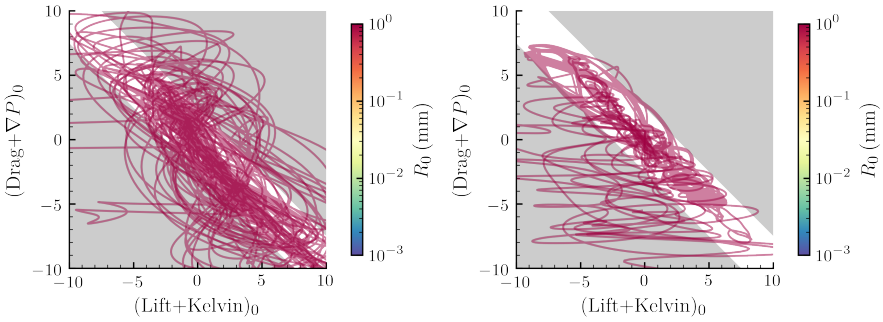

(a) Normal simulation.

(b) Simulation without bubble dynamics.

Figure 5.7: Normalized acceleration in the axial coordinates with inflow velocity and the chord length, with window averaging along time interval of 1 (ms) to demonstrate the trend.

cannot make the characteristic Lissajous curve. The lift force indeed contributes to the stagnation phenomenon.

Only acknowledging the lift effect is inadequate for building a more robust model describing this phenomenon. Details are still to be addressed, such as the detailed force direction evolution and a more exact bubble position prediction. However, the tip vortex simulation is not a sufficiently controlled environment for developing a model. A better setup could be a swirling element inside a tube with some bubbles seeded inside (inspired by Ir. Stigter, the daily supervisor, setup). Restrained by the research scope, the phenomenon shall be investigated by the future researcher.

5.5.3 *Remarks*

As a result of the interplay of several forces, the stagnation bubble phenomenon plays a critical role in the bubble population evolution of the current case and is possibly related to the cavitation hotspot. However, the influence from the drag force points out that the deficit- and jet-like axial velocity profile might affect the behavior or even the existence of the stagnation bubble. Also, the axial velocity profile, as is stated in Section 3.5.3, might contribute to different vorticity roll-up

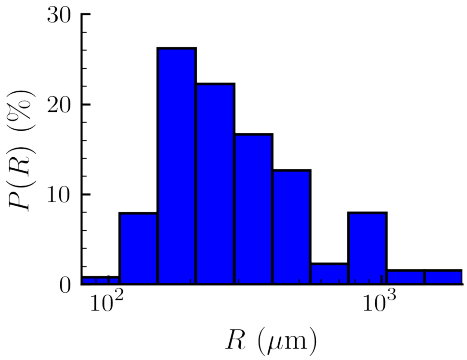

Figure 5.8: The estimated bubble probability distribution.

directions, and thus the varied lift force might yield the different behavior. Consequently, its mechanism and behavior are to be further explored by future researchers.

5.6 REGIME PLOT

The bridge between the numerical analysis and the experimental data is built statistically via the regime plot. By tracking r, $\mathrm{Re_B}$, and α, the statistical bubble behaviors could be unrevealed, and comparing the numerical and experimental results thus becomes possible. This section presents all the Lamb-Oseen, CFD tip vortex, and experimental results to gain more insight.

In Ir. Nanda's experiment, the regime plot is composed by recording plentiful bubbles within only a small streamwise range, $\delta x/c_0 \approx 0.3$. As a result, apart from the original full domain simulation, this study also carries out the numerical simulation of a small sub-domain. However, due to the initial acceleration effect, this study applies a longer streamwise distance and cuts off part of the beginning to achieve a fairer comparison. The small domain spans $x/c_0 = 1.5\text{-}2.5$, as shown previously in Figure 5.1.

The estimated experimental bubble distribution is centered around $\mathcal{O}(300)$ (μm), as shown in Figure 5.8, so only the data of the size is present.

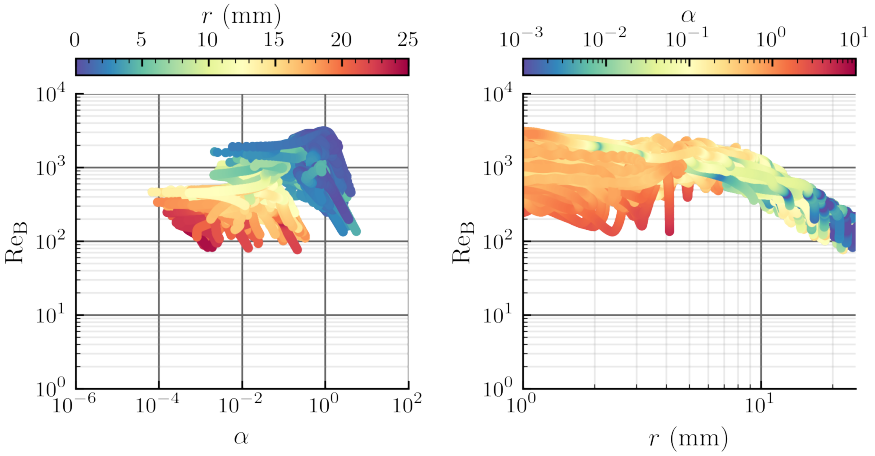

(a) Normal result from partial CFD tip vortex ($R_0 = 316\,(\mu\mathrm{m})$).

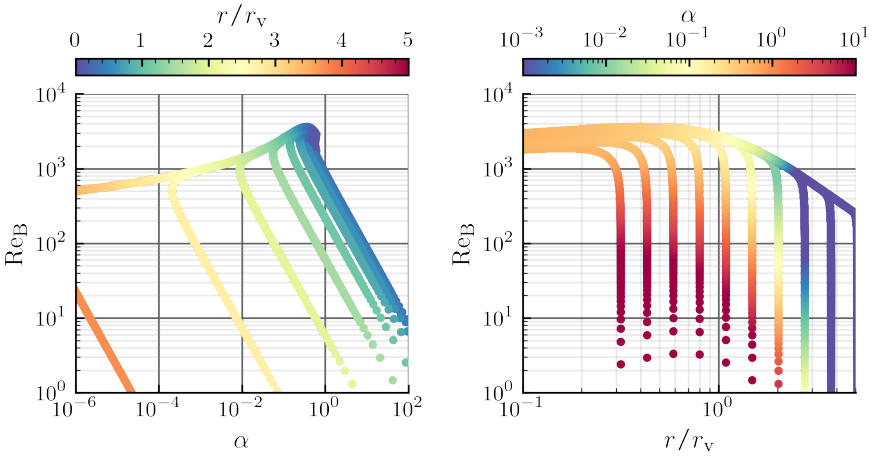

(b) Result from Lamb-Oseen vortex ($R_0 = 316\,(\mu\mathrm{m})$).

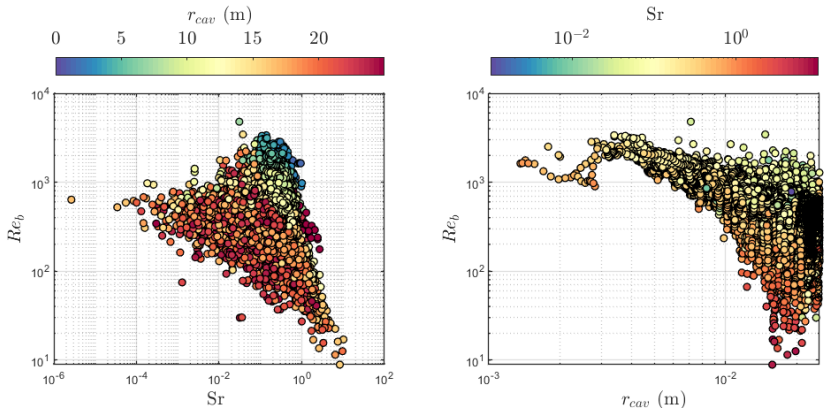

(c) Experimental result from Ir. Nanda. Sr, Re_b, and r_{cav} are his variations of α, $\mathrm{Re_B}$, and r in this study. The unit of r_{cav} in the left panel should be mm instead.

Figure 5.9: Collections of the regime plots.

The real flow CFD (Figure 5.9a) yields similar result with the Lamb-Oseen case (Figure 5.9b), especially for the r-$\mathrm{Re_B}$ sub-plot. They both follow a narrow $\mathrm{Re_B}$ trace to enter the core, meaning the radial velocity profiles are still quite similar for the bubble released at different radial positions. However, the $\mathrm{Re_B}$ behaves more chaotic around the viscous core of the CFD simulation. The reason is that the stagnation bubble comes with the velocity oscillations around a point so that $\mathrm{Re_B}$ is also oscillating in a fairly large amplitude, which is also reflected in the blue inclined lines in the α-$\mathrm{Re_B}$ sub-plot of the CFD one. Furthermore, the viscous core of the CFD tip vortex simulation is undoubtedly more complex than the Lamb-Oseen vortex. There is more than one core in a single streamwise section. Consequently, the bubble behaviors near the viscous vortex are destined to differ across the two settings. However, there are still some other optimistic results. The blue peak in the α-$\mathrm{Re_B}$ sub-plot is present in both the Lamb-Oseen and the CFD tip vortex, indicating the peak radial pressure gradient is sufficiently captured. Also, the top-left inclined envelope in the α-$\mathrm{Re_B}$ sub-plot behaves similarly across the two simulation results, indicating different bubbles share a similar radial velocity profile.

The real flow CFD (Figure 5.9a) gives an acceptable comparison with the experimental one (Figure 5.9c). Again, the blue peak and the top-left inclined envelope in the α-Re_B sub-plot are sufficiently present in both scenarios. However, the experimental data present only a looming trend of the Re_B trace in the r-Re_B sub-plot. Also, the bubbles are rarely present within the viscous core. The reasons are anticipated to be that the total record time in the experimental study is relatively short, the other bubble sizes are also not negligible, and the CFD flow field is different from the experimental one. It is acknowledged that the experimental flow field has a persistent cavity, but CFD is a fully-wetted simulation.

The regime plots from three different sources have been compared. Several essential features, such as the narrow Re_B trend and the blue Re_B peak, are present in all the sources. However, some apparent deviations are also observed, so further improvements in the CFD simulation and the experimental measurement should be taken care of to make the comparison more optimistic.

This page intentionally left blank

6

DISCUSSION

This chapter merges the previous chapters' results and some preliminary discussions from the associated simulations to provide a bird's-eye answer to the original research questions.

6.1 THE ROLES OF THE FORCES

Understanding forces' roles in the bubble motion might not be as effective in observing a phenomenon as directly running a simulation. However, these understandings are crucial to developing and dissecting the mechanism behind the phenomenon.

The bubbles are subjected to the following forces inside the flow field: (1) pressure gradient, (2) added mass, (3) drag, (4) lift, (5) hydrostatic and gravity, and (6) Kelvin impulse forces. They play different roles in the vortical flow field.

The pressure gradient and added mass forces act as the suction force to trap the bubble into the vortex core in the radial direction. However, the continuous acceleration will yield the non-negligible radial velocity; thus, the drag force grows and tries to balance the suction force. This study exploits the force balance feature to develop a series of the capturing time model in the Lamb-Oseen vortex flow field.

On the other hand, the lift force is crucial in the stability through acting in the azimuthal direction, especially in a Lamb-Oseen vortex flow field. It reduces the azimuthal velocity effectively and sufficiently balances out the Coriolis force. Thus, the lift force avoids the oscillating behavior when bubbles migrate inward. One may notice that the drag force should also provide the retarding force if there is a velocity difference in the azimuthal direction. However, the drag acceleration magnitude is relatively limited, especially for the large bubble, so the lift force still plays a critical role in stabilizing the bubble paths.

The gravitation-induced force is relatively weak compared to other accelerations, such as the pressure gradient force, so it is often ignored. Notwithstanding, if the vortex field is weak enough, the gravitational field is sufficient to affect the bubble behaviors, such as the settling bubbles in the verification study. The Kelvin impulse force is also negligible most of the time since the bubble growth is only confined in the vortex core, where the bubbles spend the least time during the capturing process.

The discussion based on the ideal Lamb-Oseen vortex can provide some basic understanding of the real tip vortex case, but there is still more to be explained. The stagnation bubble, observed in the CFD tip vortex simulation, is not spotted in the ideal case since the stagnation bubble is essentially a 3D phenomenon. All the forces other than the hydrostatic and Kelvin impulse forces contribute to the event, but instead of the radial or azimuthal direction, the interplay occurs mainly in the axial direction.

Each force plays a different role in the different flow scenarios. The pressure gradient and the added mass forces generally act as a suction around the vortex but sometimes also contribute to the axial behaviors. The drag and lift forces flexibly adjust their roles with the relative velocity vector in different flows, while the Kelvin impulse and gravitational forces are generally negligible in the context of this study.

6.2 BUBBLE POPULATION EVOLUTION AND PARAMETER INFLUENCE

The bubble population around the tip vortex is important in revealing the cavitation inception hotspots. A capture time model based on the force balance is first developed to facilitate the analysis of the Lamb-Oseen vortex. Then, the bubble motions around the CFD tip vortex are studied.

It is found that three quantities have a deterministic effect on the capturing time: initial bubble radius, initial release location, and vortex Reynolds number. The Lamb-Oseen vortex case points out that a bubble with a larger size or closer release location is entrapped more quickly than the opposite. A higher vortex Reynolds number also indicates a lower capture time.

The corresponding capture time model is developed by exploiting the apparent radial acceleration balance to identify different parameter effects on the bubble capturing phenomenon and the model gives optimistic results compared to the Lamb-Oseen case. Initially, the research aims to develop a capturing time model that can predict the 2D stationary Lamb-Oseen vortex and the realistic tip vortex flow field. However, the real tip vortex is too complex to be simplified into the flow field similar to the ideal vortex. The rolling-up process introduces the inclined vortex vector, non-axial-symmetric velocity field, and the multi-core structure in the CFD tip vortex. All the non-ideal behaviors, however, qualify the application of the model.

The tip vortex simulation analyses are thus focused more on the bubble population evolution. The first point is to understand what window upstream has to pass in order to be captured into the tip vortex in a certain finite downstream distance. It is found that both the screening and the finite-span effects are crucial parts along with the well-regarded pressure gradient suction force.

After passing the foil, it is essential to understand the bubble population evolution. The small bubble typically maintains a constant level of number because they mostly follow the streamlines and are

hard to capture if situated at the downstream ambient flow. Conversely, a large bubble can easily be captured even if distanced away from the tip vortex far downstream. It is also spotted that the large bubbles tend to accumulate at the near downstream due to the aforementioned stagnation bubble. As mentioned in the previous section, the lift, drag, pressure gradient and added mass forces dominates the stagnation bubble and pull them into either steady nodes or limit cycles situated on the tip vortex. As could be inferred, the attractors are anticipated to be the hotspot for the cavitation inception.

The capture time model developed in the Lamb-Oseen vortex helps to understand the dominating parameters in the entrapment process, but the tip vortex flow introduces the stagnation bubble phenomenon that needs additional care. These two events together yield the complex behaviors in the bubble population evolution.

6.3 COMPARISON WITH THE EXPERIMENTAL DATA

The regime plot bridges the numerical results to the experimental one, but the comparison is only acceptable. The regime plots from all the sources show limited similarities. It is anticipated that the fundamental flow field difference and the bubble recording time difference cause the deviation. However, the regime plot can successfully combine and show the bubble stages in the ideal Lamb-Oseen case. As a result, if the numerical simulation is more aligned with the experimental setups, the regime plot should provide more insight into the comparison and the mechanism.

7

CONCLUDING REMARKS

7.1 CONCLUSIONS

This research aims to better understand the bubble behaviors around the tip vortex and the related mechanisms, as a foundation of the tip vortex inception study. The research is based on a one-way coupling Eulerian-Lagrangian approach to resolve bubble motions in different flow fields.

The bubble tracking inside a CFD tip vortex flow field clearly shows the entrapment and the accumulation of the large bubbles at the near upstream, which are expected to be the hotspots of the tip vortex cavitation inception.

Driven by curiosity, the research scrutinizes the capturing events and the stagnation bubble phenomenon with the acceleration (or equivalently the force) analysis. This research develops a series of models to determine the capture time with the bubble size, initial location, and the circulation strength of a surrogate flow field, the stationary Lamb-Oseen vortex. The model reveals the radial bubble force balance between the drag, the added mass and pressure gradient, and the centrifugal forces. As an unintentional discovery while developing the model the bubble lift force is emphasized as a stabilizer of the system. The other model about the stagnation bubble phenomenon is relatively immature, but it also heralds the significance of the lift along with the other forces. It could be argued that

this study highlights the role of some common forces, such as the drag and pressure gradient forces, but also dives into the importance of the lift force, which has long been ignored.

Comparison against the experiment is also carried out via the regime plot, a more statistical way proposed by Ir. Nanda. Due to the difference in flow fields and the recording method, there are some deviations between the numerical and the experimental results. However, the idea of the regime plot has been proven capable of revealing some velocity evolution details, so it should be helpful in future research.

Nevertheless, several aspects have deducted the credibility of the research. The RSM model applied in the thesis, as stated in the literature review, shares the diffusive nature in the RANS family. Thus the axial velocity is falsely predicted, while LES is highly recommended to capture the flow field in the real world. Secondly, the bubble tracking model in this research can only deal with spherical bubbles, but the magnitude of the Weber number has already surpassed the limit drawn by the model. Also, the interpolation error, specifically in the tip vortex flow simulation, sets the ceiling the research can reach.

Despite some unavoidable limitations, the insights into the force analysis, the bubble population evolution, and the comparison against the experiment still build a solid foundation for future tip-vortex cavitation research.

7.2 RECOMMENDATIONS

The prescribed research scope and time span highly restricts the research. Consequently, some interesting potential research directions which cannot be investigated in the period are present.

INVESTIGATION OF THE LPT MODEL IN DEPTH The current LPT models include only the most common forces, but the history force, the finite-size effect and the turbulence contribution are not included in the modeling. Although some literature argues that the effect

should be negligible, a decent study with a rigorous and direct comparison to the experiment is necessary, especially in the context of the vortical flow. Also, the bubble lift force deserves further investigation either in formulation comparison or devise a new one. The deviations between different lift force models have to be described with the logarithmic scale, resulting in totally different bubble behaviors. Although some literature has presented the capture time comparison between the different models, the difference in the lift force's role should also be addressed.

CALL FOR THE BUBBLE INITIAL CONDITIONS The bubble released numerically in a flow field experiences a weird initial acceleration stage at the beginning, owing to the wrong bubble initial conditions. The initial acceleration stage shall be ruled out to make the simulation more precise. Currently, the bubbles are released with the carrier flow velocity, meaning that only the drag force is considered. This would be acceptable if released far away from the target research zone. However, it would be doubtful otherwise, especially after incorporating the history force. It is proposed that the bubble could be released with the force equilibrium velocity, through which the issue could at least be partially solved.

INVESTIGATION OF THE STAGNATION BUBBLE It is still uncertain if the stagnation bubble is a realistic phenomenon or merely a consequence of the discretization error since no experimenter or simulation expert has reported this phenomenon in the tip vortex flow. Still, Ir. Stigter has provided an optimistic evidence that the phenomenon might exist at least in the confined vortex in a pipe. If the phenomenon indeed occurs, the next step is to set up a more controlled flow field instead of the tip vortex to discover the mechanism behind it and finally model it in the context of the tip vortex.

This page intentionally left blank

APPENDICES

A

DETAILS OF THE TURBULENCE AND TRANSITION MODELS

A.1 RSM

Again, if not explicitly stated, the theory is highly based on Rumsey (2017, 2022). The transport equation for Reynolds stress reads

$$\frac{\partial \rho R_{ij}}{\partial t} + \frac{\partial \rho \left\langle U_k \right\rangle R_{ij}}{\partial x_k} = \rho P_{ij} + \rho \Pi_{ij} - \rho \varepsilon_{ij} + \rho D_{ij}. \tag{A.1}$$

The transport equation for the specific dissipation rate is defined as

$$\begin{aligned}\frac{\partial \rho \omega}{\partial t} + \frac{\partial \rho \left\langle U_k \right\rangle \omega}{\partial x_k} = \frac{\alpha_\omega \omega}{k} \frac{\rho P_{kk}}{2} - \beta_\omega \rho \omega^2 \\ + \frac{\partial}{\partial x_k} \left[\left(\mu + \sigma_\omega \frac{\rho k}{\omega} \right) \frac{\partial \omega}{\partial x_k} \right] + \sigma_d \frac{\rho}{\omega} \max \left(\frac{\partial k}{\partial x_j} \frac{\partial \omega}{\partial x_j}, 0 \right).\end{aligned} \tag{A.2}$$

The formulations of the different terms in Reynolds stress transport equation are

$$\begin{aligned}\rho P_{ij} &= -\rho R_{ik} \frac{\partial \left\langle U_j \right\rangle}{\partial x_k} - \rho R_{jk} \frac{\partial \left\langle U_i \right\rangle}{\partial x_k}, \\ \rho \Pi_{ij} &= -\left(C_1 \rho \varepsilon + \frac{1}{2} C_1^* \rho P_{kk} \right) a_{ij} \\ &\quad + C_2 \rho \varepsilon \left(a_{ik} a_{kj} - \frac{1}{3} a_{kl} a_{kl} \delta_{ij} \right) \\ &\quad + \left(C_3 - C_3^* \sqrt{a_{kl} a_{kl}} \right) \rho k \left\langle T_{ij} \right\rangle\end{aligned}$$

$$
\begin{aligned}
&+ C_4 \rho k \left(a_{ik} \left\langle S_{jk} \right\rangle + a_{jk} \left\langle S_{ik} \right\rangle - \frac{2}{3} a_{kl} \left\langle S_{kl} \right\rangle \delta_{ij} \right) \\
&+ C_5 \rho k \left(a_{ik} \left\langle W_{jk} \right\rangle + a_{jk} \left\langle W_{ik} \right\rangle \right), \\
\rho \varepsilon_{ij} =& \frac{2}{3} \rho \varepsilon \delta_{ij}, \\
\rho D_{ij} =& \frac{\partial}{\partial x_k} \left[\left(\mu \delta_{kl} + D \frac{\rho R_{kl}}{C_\mu \omega} \right) \frac{\partial R_{ij}}{\partial x_l} \right].
\end{aligned} \tag{A.3}
$$

For the pressure-strain coefficients, Launder *et al.* (1975) and Speziale *et al.* (1991) have separately provided a set of the values for the near-wall and away-from-wall treatments. All the model constants are blended in an SST fashion with

$$\phi = F_1 \phi^{(\omega)} + (1 - F_1) \phi^{(\varepsilon)} \tag{A.4}$$

$$F_1 = \tanh\left(\zeta^4 \right) \tag{A.5}$$

$$\zeta = \min \left[\max \left(\frac{\sqrt{k}}{C_\mu \omega d}, \frac{500\mu}{\rho \omega d^2} \right), \frac{4 \sigma_\omega^{(\varepsilon)} \rho k}{(CD) d^2} \right] \tag{A.6}$$

$$(CD) = \sigma_d^{(\varepsilon)} \frac{\rho}{\omega} \max \left(\frac{\partial k}{\partial x_k} \frac{\partial \omega}{\partial x_k}, 0 \right), \tag{A.7}$$

where d is the distance to the nearest wall. Table A.1 shows model coefficients for the near (with (ω)) and far-wall (with (ε)) conditions. Here, the equilibrium parameter, C_μ, is 0.09, and $C_2^{\mathrm{LLR}} = 0.52$ has been modified to better agree with the log layer of a zero-pressure gradient boundary layer.

Table A.1: Model coefficients for of RSM.

	α_ω	β_ω	σ_ω	σ_d	C_1	C_1^*	C_2	C_3	C_3^*
$\phi^{(\omega)}$	0.5566	0.075	0.5	0	1.8	0	0	0.5	0
$\phi^{(\varepsilon)}$	0.44	0.0828	0.856	1.7142	1.7	0.9	1.05	0.8	0.65

	C_4	C_5	D
$\phi^{(\omega)}$	$0.5(18C_2^{\mathrm{LLR}} + 12)/11$	$0.5(-14C_2^{\mathrm{LLR}} + 20)/11$	$0.75C_\mu$
$\phi^{(\varepsilon)}$	0.625	0.2	0.22

A.2 TRANSITION MODEL

The transport equation of intermittency reads

$$\frac{\partial \rho\gamma}{\partial t} + \frac{\partial \rho \left\langle U_j \right\rangle \gamma}{\partial x_j} = \rho P_\gamma - \rho E_\gamma + \frac{\partial}{\partial x_j}\left(\left(\mu + \frac{\mu_t}{\sigma_f}\right)\frac{\partial \gamma}{\partial x_j}\right). \tag{A.8}$$

The transport equation of the local transition Reynolds number is

$$\frac{\partial \rho \tilde{\mathrm{Re}}_{\theta t}}{\partial t} + \frac{\partial \rho \left\langle U_j \right\rangle \tilde{\mathrm{Re}}_{\theta t}}{\partial x_j} = \rho P_{\theta t} + \frac{\partial}{\partial x_j}\left(\sigma_{\theta t}(\mu + \mu_t)\frac{\partial \tilde{\mathrm{Re}}_{\theta t}}{\partial x_j}\right). \tag{A.9}$$

The production and destruction terms in the transport equation are formulated as

$$\begin{aligned} E_\gamma &= c_{a2}\bar{\Omega}\gamma F_{\mathrm{turb}}(c_{e2}\gamma - 1), \\ P_\gamma &= F_{\mathrm{length}} c_{a1}\bar{S}\left(\gamma F_{\mathrm{onset}}\right)^{0.5}(1 - c_{e1}\gamma), \\ P_{\theta t} &= c_{\theta t}\frac{1}{\mathfrak{T}}\left(\mathrm{Re}_{\theta t}^{\mathrm{eq}} - \tilde{\mathrm{Re}}_{\theta t}\right)(1.0 - F_{\theta t}). \end{aligned} \tag{A.10}$$

For F_{turb},

$$F_{\mathrm{turb}} = e^{-(R_T/4)^4}, \quad \text{with} \quad R_T = \frac{\rho k}{\mu\omega}. \tag{A.11}$$

For F_{length},

$$F_{\mathrm{length}} = F_{\mathrm{length},1}(1 - F_{\mathrm{sublayer}}) + 40F_{\mathrm{sublayer}}, \tag{A.12}$$

with

$$F_{\mathrm{length},1} = \begin{cases} 39.8189 - 0.011927\tilde{\mathrm{Re}}_{\theta t} - 0.000132567\tilde{\mathrm{Re}}_{\theta t}^2, & \tilde{\mathrm{Re}}_{\theta t} \in [0, 400), \\ 263.404 - 1.23939\tilde{\mathrm{Re}}_{\theta t} + 0.00194548\tilde{\mathrm{Re}}_{\theta t}^2 & \\ \quad -101.695 \cdot 10^{-8}\tilde{\mathrm{Re}}_{\theta t}^3, & \tilde{\mathrm{Re}}_{\theta t} \in [400, 596), \\ 0.5 - 0.0003\left(\tilde{\mathrm{Re}}_{\theta t} - 596.0\right), & \tilde{\mathrm{Re}}_{\theta t} \in [596, 1200), \\ 0.3188, & \tilde{\mathrm{Re}}_{\theta t} \in [1200, +\infty), \end{cases} \tag{A.13}$$

and

$$F_{\text{sublayer}} = e^{-(\text{Re}_\omega/200)^2}, \quad \text{with} \quad \text{Re}_\omega = \frac{\rho\omega d^2}{\mu}. \tag{A.14}$$

For F_{onset},

$$F_{\text{onset}} = \max(F_{\text{onset2}} - F_{\text{onset3}}, 0), \tag{A.15}$$

with

$$\begin{aligned} F_{\text{onset3}} &= \max\left(1 - \left(\frac{R_T}{2.5}\right)^3, 0\right), \\ F_{\text{onset2}} &= \min(\max(F_{\text{onset1}}, F_{\text{onset1}}^4), 2), \\ F_{\text{onset1}} &= \frac{\text{Re}_V}{2.193\text{Re}_{\theta c}}, \\ \text{Re}_V &= \frac{\rho \bar{S} d^2}{\mu}, \end{aligned} \tag{A.16}$$

with momentum thickness Reynolds number determined by

$$\text{Re}_{\theta c} = \begin{cases} -3.96035 + 1.0120656\tilde{\text{Re}}_{\theta t} - 0.00086823\tilde{\text{Re}}_{\theta t}^2 \\ +696.506 \cdot 10^{-9}\tilde{\text{Re}}_{\theta t}^3 - 174.105 \cdot 10^{-12}\tilde{\text{Re}}_{\theta t}^4, & \tilde{\text{Re}}_{\theta t} \leq 1870; \\ \tilde{\text{Re}}_{\theta t} - \left(593.11 + 0.482\left(\tilde{\text{Re}}_{\theta t} - 1870.0\right)\right), & 1870 < \tilde{\text{Re}}_{\theta t}. \end{cases} \tag{A.17}$$

For $F_{\theta t}$,

$$F_{\theta t} = \min\left(\max\left(F_{\text{wake}} e^{-(d/\delta)^4}, 1 - \left(\frac{c_{e2}\gamma - 1}{c_{e2} - 1}\right)^2\right), 1\right), \tag{A.18}$$

with

$$\delta = \frac{375\bar{\Omega}\mu\tilde{\text{Re}}_{\theta t} d}{\rho U^2}, \tag{A.19}$$

$$F_{\text{wake}} = e^{-(\text{Re}_\omega/10^5)^2}, \tag{A.20}$$

$$U = \sqrt{U_k U_k}. \tag{A.21}$$

For $\mathfrak{T}$,

$$\mathfrak{T} = \frac{500\mu}{\rho U^2}. \tag{A.22}$$

For $\mathrm{Re}_{\theta t}^{\mathrm{eq}}$,

$$\frac{\mathrm{Re}_{\theta t}^{\mathrm{eq}}}{F(\lambda_\theta)} = \begin{cases} 1173.51 - 589.428I + 0.2196I^{-2}, & I \leq 1.3, \\ 331.50(I - 0.5658)^{-0.671}, & I > 1.3, \end{cases} \tag{A.23}$$

with

$$F(\lambda_\theta) = \begin{cases} 1 + \left(12.986\lambda_\theta + 123.66\lambda_\theta^2 + 405.689\lambda_\theta^3\right) e^{-(I/1.5)^{1.5}}, & \lambda_\theta \leq 0, \\ 1 + 0.275\left(1 - e^{-35\lambda_\theta}\right) e^{-I/0.5}, & \lambda_\theta > 0, \end{cases} \tag{A.24}$$

where the turbulence intensity (without percentage) and effective factor read

$$I = 100\frac{\sqrt{2k/3}}{U_\infty}, \tag{A.25}$$

$$\lambda_\theta = \frac{\rho\theta_t^2}{\mu}\frac{\mathrm{d}U}{\mathrm{d}\mathbf{s}}, \tag{A.26}$$

and the streamwise velocity gradient together with momentum thickness Reynolds number say

$$\frac{\mathrm{d}U}{\mathrm{d}\mathbf{s}} = \frac{U_i U_j}{U^2}\frac{\partial U_i}{\partial x_j}, \tag{A.27}$$

$$\mathrm{Re}_{\theta t}^{\mathrm{eq}} = \frac{\rho U\theta_t}{\mu}. \tag{A.28}$$

Afterwards, γ_{eff} is computed:

$$\gamma_{\mathrm{eff}} = \max(\gamma, \gamma_{\mathrm{sep}}), \tag{A.29}$$

where

$$\gamma_{\mathrm{sep}} = \min\left(s_1 \max\left(0, \left(\frac{\mathrm{Re}_V}{3.235\mathrm{Re}_{\theta c}}\right) - 1\right) F_{\mathrm{reattach}}, 2\right) F_{\theta t}, \tag{A.30}$$

Table A.2: Constants for LCTM model.

c_{a1}	c_{a2}	c_{e1}	c_{e2}	$c_{\theta t}$	s_1	σ_γ	$\sigma_{\theta t}$
2.0	0.06	1.0	50	0.03	2	1.0	2.0

with

$$F_{\text{reattach}} = e^{-(R_T/20)^4}. \tag{A.31}$$

In Table A.2, the previously-unmentioned constants are given.

B

DERIVATION OF KELVIN IMPULSE FORCE

This chapter will demonstrate how to derive the Kelvin impulse force, including the added mass force, under the potential flow assumption. Unlike other references, this article illustrates how the impulse and force at the infinite surface vanish.

Consider a translating bubble inside a quiescent fluid, as shown in Figure B.1. Wherein, $\mathbf{n}$ represents the surface normal, $\mathbf{x}_B$ the bubble centroid, $\mathbf{x}$ an arbitrary flow field point, S_∞ an infinitely large *material* surface that encloses the whole flow field, S_B the bubble wall, and V the flow domain enclosed by the two aforementioned surfaces. The goal is to assess the fluid's force on the bubble (wall). By investigating the momentum change in the fluid flow, the force bubble exerting on the fluid is computed, and thus the force from the fluid to the bubble is obtained through Newton's third law of motion.

Newton's second law of motion of the whole fluid reads

$$\frac{\mathrm{d}\mathbf{P}}{\mathrm{d}t} = \sum \mathbf{F} = \mathbf{F}_b + \mathbf{F}_\infty + \mathbf{F}_B, \tag{B.1}$$

where $\mathbf{P}$ represents fluid momentum, $\mathbf{F}_b$ the body force, $\mathbf{F}_\infty$ the forces from S_∞, $\mathbf{F}_B$ the force from the bubble. In this scenario, the gravitational effect, thus the body force, is intentionally neglected for simplicity:

$$\frac{\mathrm{d}\mathbf{P}}{\mathrm{d}t} = \mathbf{F}_\infty + \mathbf{F}_B. \tag{B.2}$$

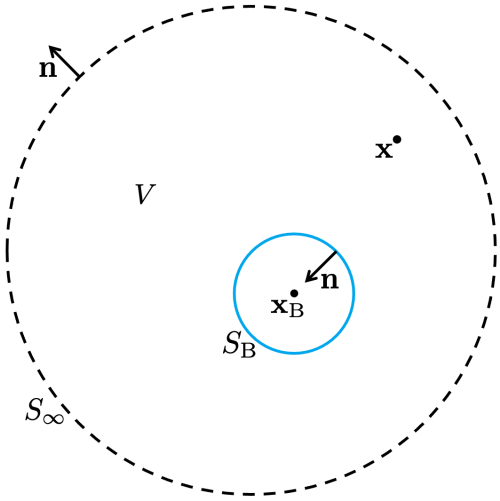

Figure B.1: Schematic diagram of a translating bubble.

The fluid momentum is calculated via a volumetric integral of the fluid velocity and mass:

$$\mathbf{P} = \int_V \rho_l \mathbf{U} \, \mathrm{d}V \,. \tag{B.3}$$

By applying the potential flow formulation and the scalar gradient theorem,

$$\mathbf{P} = \int_V \rho_l \boldsymbol{\nabla}\phi \, \mathrm{d}V = \underbrace{\int_{S_\infty} \rho_l \phi \mathbf{n} \, \mathrm{d}S}_{=\mathbf{I}_\infty} + \underbrace{\int_{S_B} \rho_l \phi \mathbf{n} \, \mathrm{d}S}_{=\mathbf{I}_B}, \tag{B.4}$$

where ϕ is the flow potential. Rearranging terms in Equations B.2 and B.4 yields

$$\mathbf{F}_B = \frac{\mathrm{d}\mathbf{I}_B}{\mathrm{d}t} - \mathbf{F}_\infty + \frac{\mathrm{d}\mathbf{I}_\infty}{\mathrm{d}t} \tag{B.5}$$

Followingly, it will be shown that the last two terms at RHS vanish if S_∞ is allowed to extend to infinity.

A translating dipole could describe the flow potential of the scenario ($\mathcal{O}(r^{-2})$) to remain the shape and a moving source ($\mathcal{O}(r^{-1})$) to account for the volume changing. Given the integral element in

$\mathbf{I}_\infty$ scales with $\mathcal{O}(r^2)$ and that the flow potential scales with $\mathcal{O}(r^{-1})$, directly evaluating $\mathbf{I}_\infty$ before temporal differentiation yields an unbounded integral. To evaluate the time derivative integral, a Reynolds-similar transport theorem should be applied:

$$\frac{\mathrm{d}}{\mathrm{d}t}\int_S \phi\mathbf{n}\,\mathrm{d}S = \int_S \frac{\mathrm{D}\phi}{\mathrm{D}t}\mathbf{n}\,\mathrm{d}S - \int_S \phi\boldsymbol{\nabla}(\mathbf{n}\cdot\mathbf{U})\,\mathrm{d}S + \int_S \phi\boldsymbol{\nabla}\cdot\mathbf{U}\mathbf{n}\,\mathrm{d}S\,, \tag{B.6}$$

of which the derivation is are given in Batchelor (2000) (page 134) and Volokh (2008). Given the incompressibility condition, the time derivative of $\mathbf{I}_\infty$ becomes

$$\frac{\mathrm{d}\mathbf{I}_\infty}{\mathrm{d}t} = \frac{\mathrm{d}}{\mathrm{d}t}\int_{S_\infty}\rho_l\phi\mathbf{n}\,\mathrm{d}S = \int_{S_\infty}\rho_l\frac{\mathrm{D}\phi}{\mathrm{D}t}\mathbf{n}\,\mathrm{d}S - \int_{S_\infty}\rho_l\phi\boldsymbol{\nabla}(\mathbf{n}\cdot\mathbf{U})\,\mathrm{d}S\,. \tag{B.7}$$

Next, the $\mathbf{F}_\infty$ term is calculated via the Bernoulli equation:

$$\begin{aligned}\mathbf{F}_\infty &= -\int_{S_\infty} P\mathbf{n}\,\mathrm{d}S \\ &= -\int_{S_\infty}\left(P_\infty - \rho\frac{\partial\phi}{\partial t} - \frac{1}{2}\rho_l|\mathbf{U}|^2\right)\mathbf{n}\,\mathrm{d}S \\ &= \int_{S_\infty}\left(\rho\frac{\partial\phi}{\partial t} + \frac{1}{2}\rho_l|\mathbf{U}|^2\right)\mathbf{n}\,\mathrm{d}S\,,\end{aligned} \tag{B.8}$$

where P_∞ term vanishes since S_∞ is a closed surface. With the information above,

$$\begin{aligned}&-\mathbf{F}_\infty + \frac{\mathrm{d}\mathbf{I}_\infty}{\mathrm{d}t} \\ &= \rho_l\int_{S_\infty}\left(-\frac{\partial\phi}{\partial t}\mathbf{n} - \frac{1}{2}|\mathbf{U}|^2\mathbf{n} + \frac{\mathrm{D}\phi}{\mathrm{D}t}\mathbf{n} - \phi\boldsymbol{\nabla}(\mathbf{n}\cdot\mathbf{U})\right)\mathrm{d}S \\ &= \rho_l\int_{S_\infty}\left(-\frac{1}{2}|\mathbf{U}|^2\mathbf{n} + \mathbf{U}\cdot\boldsymbol{\nabla}\phi\mathbf{n} - \phi\boldsymbol{\nabla}(\mathbf{n}\cdot\mathbf{U})\right)\mathrm{d}S \\ &= \rho_l\int_{S_\infty}\left(-\frac{1}{2}|\boldsymbol{\nabla}\phi|^2\mathbf{n} + \boldsymbol{\nabla}\phi\cdot\boldsymbol{\nabla}\phi\mathbf{n} - \phi\boldsymbol{\nabla}(\mathbf{n}\cdot\boldsymbol{\nabla}\phi)\right)\mathrm{d}S \\ &= \rho_l\int_{S_\infty}\left(\frac{1}{2}|\boldsymbol{\nabla}\phi|^2\mathbf{n} - \phi\boldsymbol{\nabla}(\mathbf{n}\cdot\boldsymbol{\nabla}\phi)\right)\mathrm{d}S\,.\end{aligned} \tag{B.9}$$

Given that the differential area element scales with $\mathcal{O}(r^2)$ and that the integrand is at least of $\mathcal{O}(r^{-4})$[14], so Equation B.9 will go to zero. Physically speaking, that means the total fluid kinematic energy is bounded since the applied work is bounded. Plugging the inference into Equation B.5 results in

$$\mathbf{F}_\mathrm{B} = \frac{\mathrm{d}\mathbf{I}_\mathrm{B}}{\mathrm{d}t}. \tag{B.10}$$

Finally, by applying Newton's third law of motion, $\mathbf{F}_\mathrm{B}$ becomes the additive inverse of the targeted value, $\mathbf{F}_\mathrm{K}$:

$$\mathbf{F}_\mathrm{K} = -\frac{\mathrm{d}\mathbf{I}_\mathrm{B}}{\mathrm{d}t}. \tag{B.11}$$

The remaining problem is evaluating $\mathbf{I}_\mathrm{B}$.

The fluid potential in this scenario is, as mentioned before, composed of a source and a dipole, as presented in Kundu *et al.* (2015):

$$\begin{aligned}\phi &= -\frac{R^2\dot{R}}{|\mathbf{x}-\mathbf{x}_\mathrm{B}|} - \frac{R^3}{2|\mathbf{x}-\mathbf{x}_\mathrm{B}|^3}\mathbf{U}_\mathrm{B}\cdot(\mathbf{x}-\mathbf{x}_\mathrm{B}) \\ &= -\frac{R^2\dot{R}}{\xi} - \frac{R^3}{2\xi^2}\mathbf{U}_\mathrm{B}\cdot\hat{\mathbf{r}}\end{aligned} \tag{B.12}$$

Here, $\hat{\mathbf{r}}$ is the unit vector pointing from the bubble centroid to the flow field point $\mathbf{x}$, and ξ represents the distance from the bubble centroid to the flow field point. The flow potential at the bubble surface is

$$\phi\Big|_{\xi=R} = -R\dot{R} - \frac{1}{2}R\mathbf{U}_\mathrm{B}\cdot\hat{\mathbf{r}}. \tag{B.13}$$

Thus, $\mathbf{I}_\mathrm{B}$ is evaluated as follows:

$$\begin{aligned}\mathbf{I}_\mathrm{B} &= \rho_\mathrm{l}\int_{S_\mathrm{B}} \phi(\xi=R)\mathbf{n}\,\mathrm{d}S \\ &= \rho_\mathrm{l}\int_{S_\mathrm{B}} \left(-R\dot{R} - \frac{1}{2}R\mathbf{U}_\mathrm{B}\cdot\hat{\mathbf{r}}\right)\mathbf{n}\,\mathrm{d}S\,.\end{aligned}$$

14 $\phi \sim \mathcal{O}(r^{-1})$, and $\nabla\phi \sim \mathcal{O}(r^{-2})$.

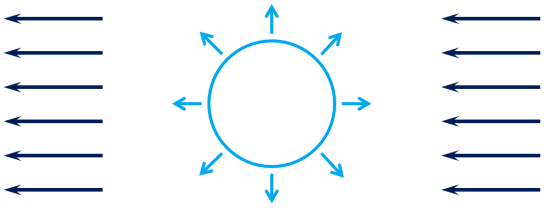

Figure B.2: Schematic diagram to explain Kelvin impulse intuitively.

Since $R\dot{R}$ is constant over the bubble wall,

$$\begin{aligned}\mathbf{I}_\mathrm{B} &= \rho_\mathrm{l} \int_{S_\mathrm{B}} \left(-\frac{1}{2} R \mathbf{U}_\mathrm{B} \cdot \hat{\mathbf{r}} \right) \mathbf{n} \, \mathrm{d}S \\ &= \rho_\mathrm{l} \int_{\theta=0}^{\pi} \int_{\phi=0}^{2\pi} -\frac{1}{2} R (\mathbf{U}_\mathrm{B} \cdot \hat{\mathbf{r}}) \mathbf{n} R^2 \sin\theta \, \mathrm{d}\phi \, \mathrm{d}\theta \\ &= \rho_\mathrm{l} \int_{\theta=0}^{\pi} \int_{\phi=0}^{2\pi} -\frac{1}{2} R^3 (\mathbf{U}_\mathrm{B} \cdot \hat{\mathbf{r}}) \mathbf{n} \sin\theta \, \mathrm{d}\phi \, \mathrm{d}\theta \,,\end{aligned}$$

and with $\mathbf{n} = -\hat{\mathbf{r}} = -\sin\theta\cos\varphi\hat{\mathbf{i}} - \sin\theta\sin\varphi\hat{\mathbf{j}} - \cos\theta\hat{\mathbf{k}}$ along with some tedious calculations,

$$\begin{aligned}\mathbf{I}_\mathrm{B} &= \frac{1}{2}\rho_\mathrm{l}\frac{4}{3}\pi R^3 \mathbf{U}_\mathrm{B} \\ &= \frac{1}{2}\rho_\mathrm{l} V_\mathrm{B} \mathbf{U}_\mathrm{B}.\end{aligned}$$

As a result,

$$\mathbf{F}_\mathrm{K} = -\frac{\mathrm{d}}{\mathrm{d}t}\left(\frac{1}{2}\rho_\mathrm{l} V_\mathrm{B}(t) \mathbf{U}_\mathrm{B}(t) \right), \tag{B.14}$$

which matches what is presented in the main body.

A more straightforward way to comprehend this phenomenon is to imagine a scenario where an expanding bubble is moving from left to right, equivalent to the fluid flowing from right to left; see Figure B.2. According to Bernoulli's equation, the windward side experiences a lower velocity than the leeward feels from the velocity superposition principle, so the pressure at the windward side is higher. As a result, an expanding bubble will experience a Kelvin impulse force opposite to the moving direction.

This page intentionally left blank

C

PLANAR MECHANICS IN POLAR COORDINATES

A minimum description of the polar coordinate as a preliminary is addressed. For further information, readers are referred to the textbooks in dynamics; see Hibbeler (2016) for example.

Two position-related unit vectors characterize the particle motion in the form of polar coordinates: outward-pointing radial direction and counter-clockwise azimuthal direction. The position $\mathbf{r}$ is defined in

$$\mathbf{r} = r\hat{\mathbf{e}}_r, \tag{C.1}$$

where $\hat{\mathbf{e}}_r = \cos\theta\hat{\mathbf{i}} + \sin\theta\hat{\mathbf{j}}$ in the Cartesian coordinate. The velocity is defined as

$$\mathbf{v} = \frac{\mathrm{d}}{\mathrm{d}t}\mathbf{r} = \dot{r}\hat{\mathbf{e}}_r + r\dot{\hat{\mathbf{e}}}_r = \dot{r}\hat{\mathbf{e}}_r + r\dot{\theta}\hat{\mathbf{e}}_\theta, \tag{C.2}$$

where

$$\frac{\mathrm{d}}{\mathrm{d}t}\hat{\mathbf{e}}_r = \quad \dot{\theta}\hat{\mathbf{e}}_\theta, \tag{C.3}$$

$$\frac{\mathrm{d}}{\mathrm{d}t}\hat{\mathbf{e}}_\theta = -\dot{\theta}\hat{\mathbf{e}}_r. \tag{C.4}$$

Differentiating the velocity formulation yields the acceleration

$$\mathbf{a} = \frac{\mathrm{d}^2}{\mathrm{d}t^2}\mathbf{r} = \left(\ddot{r} - r\dot{\theta}^2\right)\hat{\mathbf{e}}_r + \left(r\ddot{\theta} + 2\dot{r}\dot{\theta}\right)\hat{\mathbf{e}}_\theta. \tag{C.5}$$

Wherein it contains not only the normal second derivatives of the coordinate axes but also the fictitious term, or the so-called inertia

accelerations: $r\dot{\theta}^2$ and $-2\dot{r}\dot{\theta}$ represent the centrifugal and Coriolis[15] accelerations, respectively. The acceleration without the inertial terms is called the "apparent acceleration," while the total is named "absolute acceleration." The terms should be distinguished carefully in the acceleration analysis.

15 One could regard the Coriolis force here as the effect from the conservation of the angular momentum: if the bubble moves toward the center, the term will accelerate $\dot{\theta}$.

BIBLIOGRAPHY

Abdel-Maksoud, M., Hänel, D., & Lantermann, U. (2010). Modeling and computation of cavitation in vortical flow. *International Journal of Heat and Fluid Flow*, *31*(6), 1065–1074. https://doi.org/10.1016/j.ijheatfluidflow.2010.05.010

Afolabi, E., & Lee, J. (2014). An Eulerian-Eulerian CFD simulation of air-water flow in a pipe separator. *The Journal of Computational Multiphase Flows*, *6*(2), 133–149. https://doi.org/10.1260/1757-482X.6.2.133

Anderson, E. A., & Lawton, T. A. (2003). Correlation between vortex strength and axial velocity in a trailing vortex. *Journal of Aircraft*, *40*(4), 699–704. https://doi.org/10.2514/2.3148

Arakeri, V. H. (1979). Cavitation inception. *Proceedings of the Indian Academy of Sciences Section C: Engineering Sciences*, *2*(2), 149–177. https://doi.org/10.1007/BF02845030

Arndt, R. E. A., Arakeri, V. H., & Higuchi, H. (1991). Some observations of tip-vortex cavitation. *Journal of Fluid Mechanics*, *229*, 269–289. https://doi.org/10.1017/S0022112091003026

Asnaghi, A. (2015). *Developing computational methods for detailed assessment of cavitation on marine propellers* (Licentiate Thesis). Chalmers University of Technology. Göteborg, Sweden. https://research.chalmers.se/publication/217104/file/217104_Fulltext.pdf

Asnaghi, A., Bensow, R. E., & Svennberg, U. (2017a). Comparative analysis of tip vortex flow using RANS and LES. *MARINE VII: Proceedings of the VII International Conference on Computational Methods in Marine Engineering*. https://upcommons.upc.edu/handle/2117/332079

Asnaghi, A., Bensow, R. E., & Svennberg, U. (2017b). Implicit large eddy simulation of tip vortex on an elliptical foil. *Proceedings of Fifth International Symposium on Marine Propulsion (SMP'17)*. https://www.researchgate.net/publication/316460169_Implicit_Large_Eddy_Simulation_of_Tip_Vortex_on_an_Elliptical_Foil

Asnaghi, A., Svennberg, U., & Bensow, R. E. (2018). Analysis of tip vortex inception prediction methods. *Ocean Engineering*, *167*, 187–203. https://doi.org/10.1016/j.oceaneng.2018.08.053

Asnaghi, A., Svennberg, U., & Bensow, R. E. (2020). Large eddy simulations of cavitating tip vortex flows. *Ocean Engineering*, *195*, 106703. https://doi.org/10.1016/j.oceaneng.2019.106703

Auton, T. R. (1987). The lift force on a spherical body in a rotational flow. *Journal of Fluid Mechanics*, *183*, 199–218. https://doi.org/10.1017/S002211208700260X

Auton, T. R., Hunt, J. C. R., & Prud'Homme, M. (1988). The force exerted on a body in inviscid unsteady non-uniform rotational flow. *Journal of Fluid Mechanics*, *197*, 241–257. https://doi.org/10.1017/S0022112088003246

Batchelor, G. K. (2000). *An introduction to fluid dynamics*. Cambridge University Press. https://doi.org/10.1017/CBO9780511800955

Beelen, S. J. (2018). *Lagrangian trajectories method with bubble dynamics for cavitation inception predictions* (Master's thesis). University of Twente. Enschede, the Netherlands. http://essay.utwente.nl/74514/

Bertolotti, L., Jefferson Loveday, R., Ambrose, S., & Korsukova, E. (2021). A comparison of volume of fluid and Euler-Euler approaches in computational fluid dynamics modeling of two-phase flows with a sharp interface. *Journal of Turbomachinery*, *143*(12). https://doi.org/10.1115/1.4051554

Betz, A. (1933). *Behavior of vortex systems* (NACA Technical Memorandum NACA-TM-713). National Advisory Committee for Aeronautics (NACA).

Blake, J. R., Leppinen, D. M., & Wang, Q. (2015). Cavitation and bubble dynamics: The Kelvin impulse and its applications. *Interface Focus*, *5*(5), 20150017. https://doi.org/10.1098/rsfs.2015.0017

Bosschers, J. (2018). *Propeller tip-vortex cavitation and its broadband noise* (Doctoral dissertation). University of Twente. Enschede, the Netherlands. https://doi.org/10.3990/1.9789492679529

Boussinesq, J. (1877). *Essai sur la théorie des eaux courantes*. Imprimerie Nationale. https://books.google.nl/books?id=4NdQAAAAYAAJ

Brennen, C. E. (2005). *Fundamentals of multiphase flow*. Cambridge University Press. https://doi.org/10.1017/CBO9780511807169

Brennen, C. E. (2013). *Cavitation and bubble dynamics*. Cambridge University Press. https://doi.org/10.1017/CBO9781107338760

Bretherton, F. P. (1962). The motion of rigid particles in a shear flow at low Reynolds number. *Journal of Fluid Mechanics*, *14*(2), 284–304. https://doi.org/10.1017/S002211206200124X

Brouwer, J., Tukker, J., & van Rijsbergen, M. (2015). Uncertainty analysis and stationarity test of finite length time series signals. *AMT'15 The 4th International Conference on Advanced Model Measurement Technologies for the Maritime Industry*. https://www.researchgate.net/publication/295694401_Uncertainty_Analysis_and_Stationarity_Test_of_Finite_Length_Time_Series_Signals

Buevich, Y. A. (1966). Motion resistance of a particle suspended in a turbulent medium. *Fluid Dynamics*, *1*(6), 119–119. https://doi.org/10.1007/BF01022298

Bureau Veritas. (2019). *Bold strides towards URN reduction*. Retrieved January 4, 2022, from https://marine-offshore.bureauveritas.com/insight/bold-strides-towards-urn-reduction

Candelier, F., Angilella, J. R., & Souhar, M. (2004). On the effect of the Boussinesq-Basset force on the radial migration of a Stokes particle in a vortex. *Physics of Fluids*, *16*(5), 1765–1776. https://doi.org/10.1063/1.1689970

Cécora, R.-D., Eisfeld, B., Probst, A., Crippa, S., & Radespiel, R. (2012). Differential Reynolds stress modeling for aeronautics. In *50th AIAA Aerospace Sciences Meeting including the New Horizons Forum and Aerospace Exposition*. https://doi.org/10.2514/6.2012-465

Černe, G., Petelin, S., & Tiselj, I. (2001). Coupling of the interface tracking and the two-fluid models for the simulation of incompressible two-phase flow. *Journal of Computational Physics*, *171*(2), 776–804. https://doi.org/10.1006/jcph.2001.6810

Chang, E. J., & Maxey, M. R. (1994). Unsteady flow about a sphere at low to moderate Reynolds number. Part 1. Oscillatory motion. *Journal of Fluid Mechanics*, *277*, 347–379. https://doi.org/10.1017/S002211209400279X

Chen, L., Zhang, L., Peng, X., & Shao, X. (2019). Influence of water quality on the tip vortex cavitation inception. *Physics of Fluids*, *31*(2), 023303. https://doi.org/10.1063/1.5053930

Cifani, P. (2017). *DNS of turbulent bubble-laden channel flows* (Doctoral dissertation). University of Twente. Enschede, the Netherlands. https://doi.org/10.3990/1.9789036544160

Collicott, S. H., Valentine, D. T., Houghton, E. L., & Carpenter, P. W. (2016). *Aerodynamics for engineering students* (7th ed.). Butterworth-Heinemann, imprint of Elsevier. https://www.sciencedirect.com/book/9780081001943/aerodynamics-for-engineering-students

Corrsin, S., & Lumley, J. (1956). On the equation of motion for a particle in turbulent fluid. *Applied Scientific Research*, *A6*, 114–116. https://doi.org/10.1007/BF03185030

Daly, B. J., & Harlow, F. H. (1970). Transport equations in turbulence. *The Physics of Fluids*, *13*(11), 2634–2649. https://doi.org/10.1063/1.1692845

de Montgolfier, A. (2011). *Simulation of line vortex cavitation* (Master's thesis). École nationale supérieure de techniques avancées Bretagne. Brest, France.

Dijkhuizen, W., Roghair, I., van Sint Annaland, M., & Kuipers, J. (2010). DNS of gas bubbles behaviour using an improved 3d front tracking model – Drag force on isolated bubbles and comparison with experiments. *Chemical Engineering Science*, *65*(4), 1415–1426. https://doi.org/10.1016/j.ces.2009.10.021

Drela, M. (2014). *Flight vehicle aerodynamics*. The MIT Press.

Eça, L., & Hoekstra, M. (2014). A procedure for the estimation of the numerical uncertainty of CFD calculations based on grid refinement studies. *Journal of Computational Physics*, *262*, 104–130. https://doi.org/10.1016/j.jcp.2014.01.006

Egorov, Y., Menter, F. R., Lechner, R., & Cokljat, D. (2010). The scale-adaptive simulation method for unsteady turbulent flow predictions. Part 2: Application to complex flows. *Flow, Turbulence and Combustion*, *85*(1), 139–165. https://doi.org/10.1007/s10494-010-9265-4

Elghobashi, S. (1994). On predicting particle-laden turbulent flows. *Applied Scientific Research*, *52*(4), 309–329. https://doi.org/10.1007/BF00936835

Fedkiw, R. P., Aslam, T., Merriman, B., & Osher, S. (1999). A non-oscillatory eulerian approach to interfaces in multimaterial flows (the ghost fluid method). *Journal of Computational Physics*, *152*(2), 457–492. https://doi.org/10.1006/jcph.1999.6236

Finn, J., Shams, E., & Apte, S. V. (2011). Modeling and simulation of multiple bubble entrainment and interactions with two dimensional vortical flows. *Physics of Fluids*, *23*(2), 023301. https://doi.org/10.1063/1.3541813

Gatski, T., & Rumsey, C. (2002). Linear and nonlinear eddy viscosity models. In B. E. Launder & N. D. Sandham (Eds.), *Closure strategies for turbulent and transitional flows* (pp. 9–46). Cam-

bridge University Press. https://doi.org/10.1017/CBO9780511755385.003

Ghahramani, E., & Bensow, R. E. (2016). A multi-scale Eulerian-Lagrangian model for simulation of cavitating flows. *Proceedings of 19th Numerical Towing Tank Symposium (NuTTS' 16)*. https://research.chalmers.se/publication/509498/file/509498_Fulltext.pdf

Gindroz, B., & Billet, M. L. (1998). Influence of the nuclei on the cavitation inception for different types of cavitation on ship propellers. *Journal of Fluids Engineering*, *120*(1), 171–178. https://doi.org/10.1115/1.2819643

Goossens, W. R. (2019). Review of the empirical correlations for the drag coefficient of rigid spheres. *Powder Technology*, *352*, 350–359. https://doi.org/https://doi.org/10.1016/j.powtec.2019.04.075

Gosman, A. D., & loannides, E. (1983). Aspects of computer simulation of liquid-fueled combustors. *Journal of Energy*, *7*(6), 482–490. https://doi.org/10.2514/3.62687

Hibbeler, R. C. (2016). *Engineering mechanics: Dynamics* (14th). Pearson.

Hirt, C., & Nichols, B. (1981). Volume of fluid (VOF) method for the dynamics of free boundaries. *Journal of Computational Physics*, *39*(1), 201–225. https://doi.org/10.1016/0021-9991(81)90145-5

Hsiao, C.-T., Chahine, G. L., & Liu, H.-L. (2000). *Scaling effect on bubble dynamics in a tip vortex flow: Prediction of cavitation inception and noise* (Report No. 98007-1). Dynaflow, Inc.

Hsiao, C.-T., Ma, J., & Chahine, G. L. (2017). Multiscale two-phase flow modeling of sheet and cloud cavitation. *International Journal of Multiphase Flow*, *90*, 102–117. https://doi.org/10.1016/j.ijmultiphaseflow.2016.12.007

Hsiao, C.-T., & Pauley, L. L. (1999). Study of tip vortex cavitation inception using Navier-Stokes computation and bubble dy-

namics model. *Journal of Fluids Engineering*, *121*(1), 198–204. https://doi.org/10.1115/1.2822002

Hsiao, C.-T., Jain, A., & Chahine, G. L. (2006). Effect of gas diffusion on bubble entrainment and dynamics around a propeller. *Proceedings of 26th Symposium on Naval Hydrodynamics*. http://www.dynaflow-inc.com/Publications/pdf_documents/2006/26Naval_Hydrodynamic_BubbleEntrainment_Chahine_Hsiao.pdf

Johnson Jr., V. E., & Hsieh, T. (1966). The influence of the trajectories of gas nuclei on cavitation inception. *Proceedings of the 6th Symposium Naval Hydrodynamics*, 163–179. http://resolver.tudelft.nl/uuid:9e20d6b8-9b12-467c-8010-d5be6841564f

Katsuno, E. T., Lidtke, A. K., Düz, B., Rijpkema, D., Dantas, J. L., & Vaz, G. (2021). Estimating parameter and discretization uncertainties using a laminar-turbulent transition model. *Computers & Fluids*, *230*, 105129. https://doi.org/10.1016/j.compfluid.2021.105129

Keller, J. B., & Miksis, M. (1980). Bubble oscillations of large amplitude. *The Journal of the Acoustical Society of America*, *68*(2), 628–633. https://doi.org/10.1121/1.384720

Khoo, M. T., Venning, J. A., Pearce, B. W., & Brandner, P. A. (2021). Nucleation and cavitation number effects on tip vortex cavitation dynamics and noise. *Experiments in Fluids*, *62*(10), 216. https://doi.org/10.1007/s00348-021-03308-2

Kim, S., Cheong, C., & Park, W.-G. (2017). Numerical investigation on cavitation flow of hydrofoil and its flow noise with emphasis on turbulence models. *AIP Advances*, *7*(6), 065114. https://doi.org/10.1063/1.4989587

Klapwijk, M. D. (2021). *Towards predicting cavitation noise using scale-resolving simulations* (Doctoral dissertation). Delft University of Technology. Delft, the Netherlands. https://doi.org/10.4233/uuid:db85b819-cf0b-4909-8e02-9d75ca52b130

Klapwijk, M. D., Lloyd, T. P., & Vaz, G. N. V. B. (2021). The development of a partially averaged Navier-Stokes KSKL model.

Journal of Fluids Engineering. https://doi.org/10.1115/1.4052484

Klaseboer, E., Manica, R., Hendrix, M. H. W., Ohl, C.-D., & Chan, D. Y. C. (2014). A force balance model for the motion, impact, and bounce of bubbles. *Physics of Fluids*, *26*(9), 092101. https://doi.org/10.1063/1.4894067

Kreyszig, E. (2011). *Advanced engineering mathematics* (10th). Wiley.

Ku, G., Cheong, C., & Seol, H. (2020). Numerical investigation of tip-vortex cavitation noise of an elliptic wing using coupled Eulerian-Lagrangian approaches. *Applied Sciences*, *10*(17). https://doi.org/10.3390/app10175897

Kundu, P., Cohen, I., & Dowling, D. (2015). *Fluid mechanics*. Elsevier. https://books.google.nl/books?id=EehDBAAAQBAJ

Landau, L. D., & Lifshitz, E. M. (1987). *Fluid mechanics*. Pergamon Press.

Latorre, R. (1982). TVC noise envelope-an approach to tip vortex cavitation noise scaling. *Journal of Ship Research*, *26*(01), 65–75. https://doi.org/10.5957/jsr.1982.26.1.65

Launder, B. E., Reece, G. J., & Rodi, W. (1975). Progress in the development of a Reynolds-stress turbulence closure. *Journal of Fluid Mechanics*, *68*(3), 537–566. https://doi.org/10.1017/S0022211207500181 4

Lidtke, A. K. (2017). *Predicting radiated noise of marine propellers using acoustic analogies and hybrid Eulerian-Lagrangian cavitation models* (Doctoral dissertation). University of Southampton. Southampton, United Kingdom. https://eprints.soton.ac.uk/413579/

Liebrand, R. H. A. A. (2019). *Tip vortex modelling for cavitation noise applications: A verification and validation study in refresco* (Master's thesis). Delft University of Technology. Delft, the Netherlands. https://repository.tudelft.nl/islandora/object/uuid%5C%3A38888cc9-a116-42fa-bb2d-bdc7f407a78f

Liebrand, R. H. A. A., Klapwijk, M. D., Lloyd, T. P., & Vaz, G. N. V. B. (2020). Transition and turbulence modeling for the prediction of cavitating tip vortices. *Journal of Fluids Engineering*, *143*(1). https://doi.org/10.1115/1.4048133

Ligneul, P., & Latorre, R. (1993). Study of nuclei distribution and vortex diffusion influence on nuclei capture by a tip vortex and nuclei capture noise. *Journal of Fluids Engineering*, *115*(3), 504–507. https://doi.org/10.1115/1.2910167

Lopes, R. (2021). *Simulation of transition from laminar to turbulent regime in practical applications of incompressible flow* (Doctoral dissertation). Fundação para a Ciência e a Tecnologia. Lisbon, Portugal.

Lord Rayleigh, O.M., F.R.S. (1917). VIII. on the pressure developed in a liquid during the collapse of a spherical cavity. *The London, Edinburgh, and Dublin Philosophical Magazine and Journal of Science*, *34*(200), 94–98. https://doi.org/10.1080/14786440808635681

Ma, J., Hsiao, C.-T., & Chahine, G. L. (2015). Euler-Lagrange simulations of bubble cloud dynamics near a wall. *Journal of Fluids Engineering*, *137*(4). https://doi.org/10.1115/1.4028853

Magnaudet, J., & Eames, I. (2000). The motion of high-Reynolds-number bubbles in inhomogeneous flows. *Annual Review of Fluid Mechanics*, *32*(1), 659–708. https://doi.org/10.1146/annurev.fluid.32.1.659

Maines, B. H., & Arndt, R. E. A. (1993). Bubble dynamics of cavitation inception in a wing tip vortex. *ASME cavitation and multiphase flow forum, FED*.

Maxey, M. R., & Riley, J. J. (1983). Equation of motion for a small rigid sphere in a nonuniform flow. *The Physics of Fluids*, *26*(4), 883–889. https://doi.org/10.1063/1.864230

Mei, R., & Adrian, R. J. (1992). Flow past a sphere with an oscillation in the free-stream velocity and unsteady drag at finite Reynolds number. *Journal of Fluid Mechanics*, *237*(323), 323–341. https://doi.org/10.1017/S0022112092003434

Mei, R., Lawrence, C., & Adrian, R. J. (1991). Unsteady drag on a sphere at finite Reynolds number with small fluctuations in the free-stream velocity. *Journal of Fluid Mechanics*, *233*(613), 613–631. https://doi.org/10.1017/S0022112091000629

Menter, F. R. (1992). Influence of freestream values on k-ω turbulence model predictions. *AIAA Journal*, *30*(6), 1657–1659. https://doi.org/10.2514/3.11115

Menter, F. R., & Egorov, Y. (2010). The scale-adaptive simulation method for unsteady turbulent flow predictions. Part 1: Theory and model description. *Flow, Turbulence and Combustion*, *85*(1), 113–138. https://doi.org/10.1007/s10494-010-9264-5

Menter, F. R., Egorov, Y., & Rusch, D. (2006). Steady and unsteady flow modelling using the k-$\sqrt{k}L$ model. *Turbulence, Heat and Mass Transfer, 5th International symposium, Proceedings*, 403–406. https://doi.org/10.1615/ICHMT.2006.TurbulHeatMassTransf.800

Mohamed, K., Nadarajah, S., & Paraschtvoiu, M. (2009). Simulation of a wing tip vortex at static and dynamic stall conditions with a DES method. *47th AIAA Aerospace Sciences Meeting and the New Horizons Forum and Aerospace Exhibit 2009*, *47*, 588–609. https://www.tib.eu/de/suchen/id/BLCP%5C%3ACN073664595

Moore, D. W., Saffman, P. G., & Stewartson, K. (1973). Axial flow in laminar trailing vortices. *Proceedings of the Royal Society of London. A. Mathematical and Physical Sciences*, *333*(1595), 491–508. https://doi.org/10.1098/rspa.1973.0075

Nanda, S., Muller, K., van Terwisga, T. J. C., Westerweel, J., & Elsingaa, G. (2022). *Simultaneous three dimensional measurement of vortex kinematics and cavity dynamics for vortex-cavitation flows* [To-be-published journal article that is under peer-reviewing].

Nie, S., Krimmelbein, N., Krumbein, A., & Grabe, C. (2018). Coupling of a Reynolds stress model with the γ-$\mathrm{Re}_{\theta t}$ transition model. *AIAA Journal*, *56*(1), 146–157. https://doi.org/10.2514/1.J056167

Nieuwstadt, F. T., Westerweel, J., & Boersma, B. J. (2016). *Turbulence: Introduction to theory and applications of turbulent flows* (1st ed.). Springer International Publishing. https://doi.org/10.1007/978-3-319-31599-7

Ohl, C.-D., Kurz, T., Geisler, R., Lindau, O., & Lauterborn, W. (1999). Bubble dynamics, shock waves and sonoluminescence. *Philosophical Transactions of the Royal Society of London. Series A: Mathematical, Physical and Engineering Sciences*, *357*(1751), 269–294. https://doi.org/10.1098/rsta.1999.0327

Ohl, C.-D., Tijink, A., & Prosperetti, A. (2003). The added mass of an expanding bubble. *Journal of fluid mechanics*, *482*, 271–290.

Olsen, J. E., Skjetne, P., & Johansen, S. T. (2017). VLES turbulence model for an Eulerian-Lagrangian modeling concept for bubble plumes. *Applied Mathematical Modelling*, *44*, 61–71. https://doi.org/10.1016/j.apm.2017.01.031

Osher, S., & Fedkiw, R. P. (2001). Level set methods: An overview and some recent results. *Journal of Computational Physics*, *169*(2), 463–502. https://doi.org/10.1006/jcph.2000.6636

Oweis, G. F., van der Hout, I. E., Iyer, C., Tryggvason, G., & Ceccio, S. L. (2005). Capture and inception of bubbles near line vortices. *Physics of Fluids*, *17*(2), 022105. https://doi.org/10.1063/1.1834916

Park, I., Kim, J., Paik, B., & Seol, H. (2021). Numerical study on tip vortex cavitation inception on a foil. *Applied Sciences*, *11*(16). https://doi.org/10.3390/app11167332

Paskin, L., Visonneau, M., Guilmineau, E., & Wackers, J. (2019). Computational modeling of turbulent flows on the tip vortex of a marine propeller's blade. *6th International Symposium on Marine Propulsors (SMP'19)*. https://hal.archives-ouvertes.fr/hal-02873483

Peng, X., Lianghao, X., & Cao, Y. (2017). The study of tip vortex flow and cavitation inception on an elliptical hydrofoil. *Proceedings of Fifth International Symposium on Marine Propulsion (SMP'17)*.

https://www.marinepropulsors.com/proceedings/2017/WB2-3.pdf

Pennings, P. C. (2016). *Dynamics of vortex cavitation* (Doctoral dissertation). Delft University of Technology. Delft, the Netherlands. https://doi.org/10.4233/uuid:80840e36-abea-4682-b774-6e826b7f86e0

Peters, A. (2019). *Numerical modelling and prediction of cavitation erosion using Euler-Euler and multi-scale Euler-Lagrange methods* (Doctoral dissertation). University Duisburg-Essen. Duisburg, Essen, Germany. https://doi.org/10.17185/duepublico/71156

Peters, A., & el Moctar, O. (2020). Numerical assessment of cavitation-induced erosion using a multi-scale Euler-Lagrange method. *Journal of Fluid Mechanics*, *894*, A19. https://doi.org/10.1017/jfm.2020.273

Phillips, W. R. C. (1981). The turbulent trailing vortex during roll-up. *Journal of Fluid Mechanics*, *105*, 451–467. https://doi.org/10.1017/S0022112081003285

Plesset, M. S. (1949). The dynamics of cavitation bubbles. *Journal of Applied Mechanics*, *16*(3), 277–282. https://doi.org/10.1115/1.4009975

Pope, S. B. (1975). A more general effective-viscosity hypothesis. *Journal of Fluid Mechanics*, *72*(2), 331–340. https://doi.org/10.1017/S0022112075003382

Propulsion Committee of 23rd ITTC. (2002). *Testing and extrapolation methods propulsion; cavitation – Description of cavitation appearances* (Recommended Procedures and Guidelines No. 7.5 - 02 - 03 - 03.2). International Towing Tank Conference (ITTC).

Prosperetti, A., & Lezzi, A. (1986). Bubble dynamics in a compressible liquid. Part 1. First-order theory. *Journal of Fluid Mechanics*, *168*, 457–478. https://doi.org/10.1017/S0022112086000460

Reynolds, O. (1895). IV. on the dynamical theory of incompressible viscous fluids and the determination of the criterion. *Philo-*

sophical Transactions of the Royal Society of London. (A.), *186*, 123–164. https://doi.org/10.1098/rsta.1895.0004

Richardson, L. F., & Glazebrook, R. T. (1911). IX. the approximate arithmetical solution by finite differences of physical problems involving differential equations, with an application to the stresses in a masonry dam. *Philosophical Transactions of the Royal Society of London. Series A, Containing Papers of a Mathematical or Physical Character*, *210*(459-470), 307–357. https://doi.org/10.1098/rsta.1911.0009

Roghair, I., Lau, Y., Deen, N., Slagter, H., Baltussen, M., van Sint Annaland, M., & Kuipers, J. (2011). On the drag force of bubbles in bubble swarms at intermediate and high Reynolds numbers [10th International Conference on Gas-Liquid and Gas-Liquid-Solid Reactor Engineering]. *Chemical Engineering Science*, *66*(14), 3204–3211. https://doi.org/10.1016/j.ces.2011.02.030

Rule, J. A., & Bliss, D. B. (1998). Prediction of viscous trailing vortex structure from basic loading parameters. *AIAA Journal*, *36*(2), 208–218. https://doi.org/10.2514/2.7503

Rumsey, C. (2017). *Implementing turbulence models into the compressible RANS equations*. Retrieved February 10, 2022, from https://turbmodels.larc.nasa.gov/implementrans.html

Rumsey, C. (2022). *SSG/LRR full Reynolds stress model*. Retrieved February 10, 2022, from https://turbmodels.larc.nasa.gov/rsm-ssglrr.html

Ruth, D., Vernet, M., Perrard, S., & Deike, L. (2021). The effect of nonlinear drag on the rise velocity of bubbles in turbulence. *Journal of Fluid Mechanics*, *924*. https://doi.org/10.1017/jfm.2021.556

Salvatore, F., Streckwall, H., & van Terwisga, T. J. C. (2009). Propeller cavitation modelling by CFD - results from the VIRTUE 2008 rome workshop. *First International Symposium on Marine Propulsors (SMP'09)*. http://resolver.tudelft.nl/uuid:aad861db-1f8b-4f44-bef2-3d324c3eb1ee

Schiller, L., & Neumann, A. (1933). Uber die grundlegenden berechnungen bei der schwerkraftaufbereitung. *Zeitschrift des Vereines Deutscher Ingenieure*, *77*, 318–321. https://cir.nii.ac.jp/crid/1570854176037493120

Sokolichin, A., Eigenberger, G., Lapin, A., & Lübert, A. (1997). Dynamic numerical simulation of gas-liquid two-phase flows Euler/Euler versus Euler/Lagrange. *Chemical Engineering Science*, *52*(4), 611–626. https://doi.org/10.1016/S0009-2509(96)00425-3

Speziale, C. G., Sarkar, S., & Gatski, T. B. (1991). Modelling the pressure-strain correlation of turbulence: An invariant dynamical systems approach. *Journal of Fluid Mechanics*, *227*, 245–272. https://doi.org/10.1017/S0022112091000101

Sridhar, G., & Katz, J. (1995). Drag and lift forces on microscopic bubbles entrained by a vortex. *Physics of Fluids*, *7*(2), 389–399. https://doi.org/10.1063/1.868637

Takemura, F., & Magnaudet, J. (2004). The history force on a rapidly shrinking bubble rising at finite Reynolds number. *Physics of Fluids*, *16*(9), 3247–3255. https://doi.org/10.1063/1.1760691

Talaei, A., & Garrett, T. J. (2020). On the Maxey-Riley equation of motion and its extension to high Reynolds numbers. https://arxiv.org/abs/2006.16577

Tchen, C.-M. (1947). *Mean value and correlation problems connected with the motion of small particles suspended in a turbulent fluid*. Springer.

Terziev, M., Tezdogan, T., & Incecik, A. (2020). Application of eddy-viscosity turbulence models to problems in ship hydrodynamics. *Ships and Offshore Structures*, *15*(5), 511–534. https://doi.org/10.1080/17445302.2019.1661625

Thomas, N. H., Auton, T. R., Sene, K., & Hunt, J. C. R. (1983). Entrapment and transport of bubbles by transient large eddies in multiphase turbulent shear flows. *Papers presented at the International Conference on Physical Modelling of Multi-Phase Flow*, 169–184.

Thomas, N. H., Auton, T. R., Sene, K., & Hunt, J. C. R. (1984). Entrapment and transport of bubbles by plunging water. *Gas Transfer at Water Surfaces*, 255–268.

Vallier, A. (2010). *Eulerian and Lagrangian cavitation related simulations using openfoam* (Licentiate Thesis). Chalmers University of Technology. Göteborg, Sweden. http://www.tfd.chalmers.se/~hani/pdf_files/LIC_AV_2010_finalversion.pdf

Vallier, A. (2013). *Simulations of cavitation - from the large vapour structures to the small bubble dynamics* (Doctoral dissertation). Lund University. Lund, Sweden. https://www.energy.lth.se/fileadmin/energivetenskaper/Avhandlingar/Vallier_PhD.pdf

van den Boogaard, M. (2019). *Numerical simulation of a cavitating line vortex in a converging-diverging nozzle* (Master's thesis). Delft University of Technology. Delft, the Netherlands. http://resolver.tudelft.nl/uuid:d04e2cb2-7371-4ebf-bc96-6c2e5a48874a

van Eijkeren, D. F. (2016). *Dispersed droplet dynamics during produced water treatment in oil industry* (Doctoral dissertation). University of Twente. Enschede, the Netherlands. https://doi.org/10.3990/1.9789036540438

van Wijngaarden, E., Bosschers, J., & Kuiper, G. (2005). Aspects of the cavitating propeller tip vortex as a source of inboard noise and vibration. *Proceedings of the ASME 2005 Fluids Engineering Division Summer Meeting, 2: Fora*, 539–544. https://doi.org/10.1115/FEDSM2005-77271

Volokh, K. Y. (2008). On the material time derivative of volume, surface, and line integrals. https://doi.org/10.48550/arXiv.0807.3434

Wardle, K. E., & Weller, H. G. (2013). Hybrid multiphase CFD solver for coupled dispersed/segregated flows in liquid-liquid extraction. *International Journal of Chemical Engineering, 2013*, 128936. https://doi.org/10.1155/2013/128936

Weller, H. G. (2008). *A new approach to VOF-based interface capturing methods for incompressible and compressible flow* (Technical Report TR/HGW/04). OpenCFD Ltd.

Wilcox, D. C. (2006). *Turbulence modeling for CFD*. DCW Industries.

Xie, C., Liu, J., Jiang, J.-W., & Huang, W.-X. (2021). Numerical study on wetted and cavitating tip-vortical flows around an elliptical hydrofoil: Interplay of cavitation, vortices, and turbulence. *Physics of Fluids*, *33*(9), 093316. https://doi.org/10.1063/5.0064717

Xing, T., & Stern, F. (2015). Comment on "A procedure for the estimation of the numerical uncertainty of CFD calculations based on grid refinement studies" (L. Eça and M. Hoekstra, *Journal of Computational Physics* 262 (2014) 104130). *Journal of Computational Physics*, *301*, 484–486. https://doi.org/https://doi.org/10.1016/j.jcp.2015.08.046

Xu, J., Maxey, M. R., & Karniadakis, G. E. (2002). Numerical simulation of turbulent drag reduction using micro-bubbles. *Journal of Fluid Mechanics*, *468*, 271–281. https://doi.org/10.1017/S0022112002001659

Yakubov, S., Cankurt, B., Maquil, T., Schiller, P., Abdel-Maksoud, M., & Rung, T. (2011). Advanced Lagrangian approaches to cavitation modelling in marine applications. *IV. International Conference on Computational Methods in Marine Engineering, MARINE 2011*, 217–234. http://hdl.handle.net/11420/7029

Zhang, L., Chen, L., & Shao, X. (2016). The migration and growth of nuclei in an ideal vortex flow. *Physics of Fluids*, *28*(12), 123305. https://doi.org/10.1063/1.4972275

Zhang, Z., Legendre, D., & Zamansky, R. (2019). Model for the dynamics of micro-bubbles in high-Reynolds-number flows. *Journal of Fluid Mechanics*, *879*, 554–578. https://doi.org/10.1017/jfm.2019.662

COLOPHON

This document was typeset using the typographical look-and-feel `classicthesis` developed by André Miede and Ivo Pletikosić. The style was inspired by Robert Bringhurst's seminal book on typography *"The Elements of Typographic Style"*. `classicthesis` is available for both LaTeX and LyX:

https://bitbucket.org/amiede/classicthesis/

Final Version as of 2022-08-22 (classicthesis v4.6).